NBSIR 80-2178 (DoE)

Vaporization and Chemical Transport Under Coal Gasification Conditions

J. W. Hastie, D. W. Bonnell, E. R. Plante, W. S. Horton

High Temperature Processes Group
Chemical Stability and Corrosion Division
Center for Materials Science
National Bureau of Standards
U.S. Department of Commerce
Washington, DC 20234

December 1980

NBSIR 80-2178 (DoE)

VAPORIZATION AND CHEMICAL TRANSPORT UNDER COAL GASIFICATION CONDITIONS

J. W. Hastie, D. W. Bonnell, E. R. Plante, W. S. Horton

High Temperature Processes Group
Chemical Stability and Corrosion Division
Center for Materials Science
National Bureau of Standards
U.S. Department of Commerce
Washington, DC 20234

December 1980

U.S. DEPARTMENT OF COMMERCE, Philip M. Klutznick, *Secretary*

Jordan J. Baruch, *Assistant Secretary for Productivity, Technology, and Innovation*

NATIONAL BUREAU OF STANDARDS, Ernest Ambler, *Director*

Abstract

The present studies have resulted in the development of a new experimental technique, transpiration mass spectrometry, for the quantitative analysis of high temperature vapors and gases. This technique has been applied to vapor transport and thermodynamic activity determinations for real and synthetic coal slag samples in reactive coal gas components at pressures up to atmospheric. The results indicate a highly non-ideal and non-monotonic (with respect to temperature and composition) behavior for alkali metal vapor transport. Thus <u>a</u> <u>priori</u> predictions of alkali metal transport in coal gasifiers without actual activity data are virtually impossible at the present time. Surface segregation and diffusion limitations of alkali species in slags are also possible complicating effects in relating laboratory data to plant experience.

Since 1974, the National Bureau of Standards has been engaged in research designed to address materials problems and needs pertinent to coal conversion and utilization technologies. This work has been sponsored in part, at first by the Office of Coal Research, then by the Energy Research and Development Administration, and most recently by the Department of Energy. The main emphasis has been on test method development and particularly on accelerated procedures for evaluating materials behavior and durability. Complementary efforts have been made on the determination of the mechanisms of materials degradation and on the development and operation of materials data centers to provide evaluated information on properties and performance including failures occurring in operating plants.

During the FY77-79 period the NBS program, entitled "Materials Research for the Clean Utilization of Coal" consisted of a number of interrelated tasks including:

1. Metal Corrosion

    a. Constant Strain Rate Test
    b. Pre-cracked Fracture Test

2. Ceramic Deformation, Fracture, and Erosion

3. Chemical Degradation of Ceramics

    a. Reactions and Transformations
    b. Slag Characterization (viscosity)
    c. Vaporization and Chemical Transport

4. Failure Prevention

    a. Failure Information Center
    b. Materials Properties Data Center

The results of the research have been disseminated through quarterly reports of progress (available from NTIS; report designation EA-6010; Dist. Category UC-90C) as well as numerous scientific publications in technical journals. Further, as individual tasks are completed, an overall report is prepared detailing the results and accomplishments of the project. This present publication is the final report for the project on Vaporization and Chemical Transport.

SAMUEL J. SCHNEIDER
Program Manager
Center for Materials Science
National Bureau of Standards

TABLE OF CONTENTS

VAPORIZATION AND CHEMICAL TRANSPORT UNDER
COAL GASIFICATION CONDITIONS

1. Introduction

1.1 Background

In recent years the economic and strategic advantages of coal as an energy source have gained widespread attention. As a result, numerous processes for converting coal to low and high Btu gas are under development. The conversion reactions involve extremes of temperature (700 to 1500 K range) and pressure (1 to 70 atm range) as well as very reactive atmospheres, ranging from oxidizing to highly reducing. Reactor wall liner materials must therefore be constructed from refractory ceramic materials. However, the durability of even established refractory oxides under the unique conditions of coal gasification is open to question (Sadler, et al., 1979, Raymon and Sadler, 1976).

Chemical degradation of ceramics in reducing atmospheres (H_2) and H_2O-containing atmospheres is relatively well known. Vapor transport of reduced species such as SiO, Al_2O, and Mg, and of hydrated species such as $Si(OH)_4$ is a significant factor in process atmosphere corrosion. We have summarized the laboratory evidence for vapor transport processes of this type elsewhere (Hastie, 1975, p. 37, 91, 212). This evidence is based on systems with relatively few components, and quantitative extrapolation to coal gasification conditions is not possible. That is, there is a need to examine refractory-coal gas interactions under conditions more closely approximating those proposed for gasification as was stressed by Raymon and Sadler (1976).

In addition to the reactive nature of the coal gas itself, the coal mineral impurities, even in minor amounts, can be highly corrosive to ceramics. Volatile alkali metal (Na and K), iron, sulfur, and halogen-containing species are the prime candidates for ceramic degradation. Vapor transport (to ceramic surfaces) of these impurities will be primarily controlled by their thermodynamic activity in the coal slag or ash. This activity will, in turn, be highly dependent on the slag-coal gas reactivity. For instance, release of Na will be controlled by the vapor-phase processes:

$$Na_2O \text{ (in slag)} = 2Na + \tfrac{1}{2}O_2 \tag{1}$$

$$H_2 + \tfrac{1}{2}O_2 = H_2O \quad , \tag{2}$$
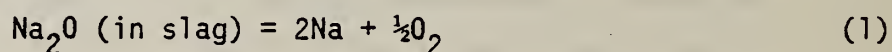
where a reducing atmosphere will drive reaction (1) in the forward direction. Other impurities and gas components will also affect this vapor transport process, e.g.,

$$2HCl + Na_2O \text{ (in slag)} = 2NaCl + H_2O \tag{3}$$

$$H_2O + Na_2O \text{ (in slag)} = 2NaOH \quad . \tag{4}$$
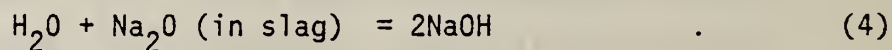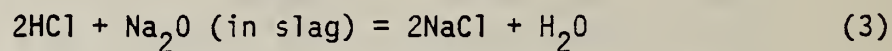
Clearly, thermodynamic prediction of the vapor concentration of, say, Na requires consideration of many competing equilibria. Another complication arises from the possible presence of new species and reactions. For instance, in high pressure steam an enhanced vapor transport of NaCl has been attributed to the hydrate, $NaCl \cdot 2H_2O$ (see Hastie, 1975 p.82). Existing thermochemical tables, which may be used to select likely vapor transport reactions are inadequate as the species selection is based largely on results for simple low pressure systems. Thus, under the higher pressure and complex mixture conditions of coal gasification, novel species and vapor transport reactions are likely.

The identification of species and reactions under the combined conditions of high pressure (> 1 atm), high temperature (T ~ 1700 K), and complex chemistry, is a challenging measurement problem. At the outset of this research project, no single measurement tool existed for the quantitative molecular characterization of high temperature processes representative of coal gasification. The best available methods of Knudsen effusion mass spectrometry (KMS) and transpiration have limited applicability. The KMS technique is molecular specific but is limited by molecular flow requirements to an upper limit total gas pressure of about 10^{-4} atm. Transpiration, on the other hand, is well suited to pressures of 1 atm and higher but does not provide molecular species identification in complex gas mixtures. A coupling of these two classical techniques would clearly resolve the individual limitations.

1.2 Objectives

A two-fold experimental objective was required for this project. First, a novel measurement technique was to be developed, based on a coupling of the Knudsen effusion mass spectrometric and transpiration methods. This technique was then to be applied to a molecular-level thermodynamic characterization of synthetic coal-gas-slag-ceramic vapor transport processes. As a secondary objective, multicomponent, heterogeneous, thermodynamic modeling methods were to be developed to complement the experimental analysis and extend the range of applicability of the data.

2. Technical Approach

An NBS-developed High Pressure Sampling Mass Spectrometer System (HPMS) (Hastie, 1973) was used as the basic vacuum and mass analysis component of the Transpiration Mass Spectrometer (TMS). The transpiration component of this apparatus consisted primarily of a platinum reactor with radiative heating provided by a tantalum tube furnace. Slag or ceramic samples were contained in a platinum boat within the

hot zone of the reactor. Reactive coal gas components (e.g., H_2, H_2O) were introduced, together with the carrier or transport gas (N_2 or Ar), and allowed to come to thermal equilibrium with the boat-sample. The gaseous reaction products were then sampled in real time through a small orifice and a molecular beam produced for mass analysis. Thus, species partial pressure data could be obtained as a function of inlet gas composition, pressure, temperature, and slag composition.

Figure 1 shows a photograph of key reactor components. Additional details of the apparatus and experimental procedure are given in Appendix A (see Sections 2 and 3).

Several approaches were devised for theoretical modeling of coal-gas-slag-ceramic interactions. First, a generally available computer code (Gordon and McBride, 1971) was adapted for this purpose. This code allows for the thermodynamic analysis of multicomponent gas mixtures reacting with condensed ideal solutions. Hence, in dealing with the highly non-ideal case of slag, it was necessary to postulate the formation and ideal mixing of various silicate compounds to simulate the slag thermochemistry. This approach was found to be less than satisfactory and a more comprehensive and less generally available code, SOLGASMIX (Eriksson, 1975) was obtained for explicit treatment of non-ideal solutions.

3. Results and Discussion

3.1 Reference Materials Analyses

The design, calibration, validation, and implementation of the TMS system required detailed studies on several well-characterized reference materials; namely, liquid NaCl and Na_2SO_4. Appendix A, Sections 4 and 5, contains a summary of the TMS system-performance and new thermodynamic data for these molten salts. In summary, the results indicate that the reactor can faithfully sample (i.e., without chemical perturbation) a complex gas-vapor mixture

4

in a heterogeneous system at thermodynamic equilibrium. Also, the temperature and pressure range attainable was found to be within that required for slag-coal gas analyses.

3.2 Vapor Transport Over Illinois Number 6 Coal Slag (K_1)[1]

In order to interpret the effects of coal gas components on coal-slag vapor transport, one needs, as base data, the vaporization behavior under vacuum and inert gas conditions. These data, obtained using the KMS and TMS (N_2 carrier gas) methods, respectively, are summarized in Appendix B, Section 2.2.2. In these studies, the thermodynamic activities of Na and K in the slag were extremely low and samples with additional alkali were needed to obtain accurate data on alkali transport under <u>inert</u> gaseous atmospheres. Vapor pressure data were then obtained as a function of alkali content and temperature, as shown, for example, in figures 6 and 7, Appendix B. Addition of water vapor to the transport atmosphere enhanced the release of K to the vapor phase, as shown in figure 9, Appendix B. This enhanced transport is attributed to the processes:

$$H_2O = H_2 + \tfrac{1}{2}O_2 \tag{5}$$

$$H_2 + K_2O \text{ (in slag)} = 2K + H_2O \quad . \tag{6}$$
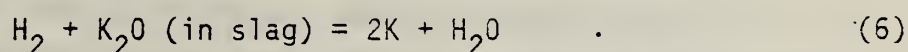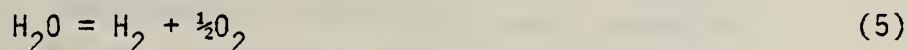
To determine the effect of added H_2, in amounts typical of coal gasification conditions, a synthetic slag with greater purity and homogeneity was selected.

3.3 Vapor Transport Over Synthetic Slag (K_2)

A lower melting, more basic, (as compared with the K_1 sample) synthetic slag was prepared for studies analogous to those performed for the K_1 system.

---

[1]The terminology K_1 (and K_2 in later discussion) is used to designate potassium-containing slags.

Under free vaporization (KMS) or N_2-atmosphere (TMS) conditions
the predominant vapor species in this system are K and O_2, as
shown in figure 2. The initial excess of O_2 present in this
slag is believed to result from the preparation procedure
where melting and pouring in room air led to oxygen absorption
by the sample. Pressure bursts of K and O_2 were noted in the
initial phase of the TMS experiments, e.g., at 1500 K in
figure 2, suggesting that trapped gas was released from the
slag.

The appreciable effect of H_2O vapor on the release of K from
the K_2 slag is demonstrated in figure 3. The data are consistent
with the reactions (5) and (6) as the primary process leading
to the enhanced release of alkali. Also, as the data agree
with the thermodynamic pressure dependence (slope 0.5 for the
curve of figure 3), the system appears to be at equilibrium.
In addition, a process involving KOH formation was also observed,
but to a much lesser degree than reaction (6), as shown in figure 4.

Previous attempts at modeling complex multicomponent systems,
including slags, have either assumed ideal solution behavior
or an ideal mixing of hypothetical complex species. However,
it is well known, and our experimental data confirm this, that
slags form highly non-ideal solutions. Accordingly, we have
applied, for the first time, a non-ideal solution multicomponent
equilibrium computer program to a slag system. The program,
known as SOLGASMIX is based on the development by Eriksson
[Eriksson (1975)]. As a test case we have taken the K_2 slag
system with 1 atm H_2 present. Typical data are given in table 1,
where the effect of non-ideal solution behavior is clearly demon-
strated. Also, at 1500 K, the atomic potassium species is much
more significant than KOH; 87 percent of the alkali is released
as K under these conditions.

Table 1

EXAMPLE OF THERMODYNAMIC MODEL OUTPUT[a]

Species	Ideal Solution Pressure (atm)		Non-ideal Solution[b] Pressure (atm)	
	(1000 K)	(1500 K)	(1000 K)	(1500 K)
K	6.7 -3[c]	1.8 -2	3.3 -8	4.6 -6
KOH	1.4 -2	3.3 -3	8.2 -8	6.7 -7
H_2	0.96	0.95	0.97	0.97
H_2O	2.3 -2	3.4 -2	2.7 -2	2.7 -2
O_2	4.2 -24	4.5 -15	5.7 -24	2.7 -15

---

[a]System K_2 slag wt %; SiO_2 (47.3), Al_2O_3 (11.1), Fe_2O_3 (12), CaO (13.9), MgO (7.0), K_2O (8.7).

[b]Activity K_2O experimental input (K_2O + SiO_2 data used).

[c]Computer notation; e.g., 6.7 -3 = 6.7×10^{-3}.

3.4 K_2 Slag + H_2 System

In order to verify the above reaction scheme [reactions (5) and (6)] and to extend the vapor transport conditions to a reducing environment closer to that present in coal gas, a series of measurements were made using H_2 as the initial reactant gas. Compositions of H_2-N_2-H_2O-O_2 gas up to 10 volume percent H_2 were attained prior to hydrogen-induced corrosive loss of the transpiration reactor.

As H_2 is introduced to the slag system, the O_2 concentration is decreased and H_2O increases in accord with reaction (2). Typical data are given in figure 5. Note that at relatively low H_2 concentration (partial pressure < 5×10^{-3} atm) the O_2 scavenging

process provides a high concentration of H_2O. As there are three interdependent reactive gases simultaneously present (H_2, H_2O, and O_2), the dependence of K pressure on reactive gas pressure can be complex, as shown in figure 6. For the decreasing partial pressure region of the run chronology, the one-half power dependence of K pressure on H_2O pressure [resulting from reaction (5)] is consistent with reaction (6) as the main process.

3.5 K_2 Slag System--Time Dependent Observations

During the initial heating-vaporization phase, using a non-reactive N_2 carrier gas, a periodic pressure burst phenomenon was noted for both the K and O_2 vapor species. As shown in figure 7, the rise time for such a burst is almost instantaneous once the critical temperature is reached. After about 20 minutes at constant temperature, the K and O_2 pressures return to the expected level. This type of phenomenon has also recently been observed in solar heating experiments of liquid oxides. The explanation for this effect in our system is unclear but may be indicative of a non-homogeneous sample, perhaps containing residual K_2CO_3 used in the slag-synthesis. Alternatively, phase separation of an initially homogeneous sample may be possible.

A second type of time dependent phenomenon was observed for this slag, as shown in figure 8. Once an isothermal condition has been achieved, the K pressure falls off with time. We believe that this results from surface depletion of K (and O_2) from the sample, due to the bulk diffusion rate being too small relative to the surface vaporization rate. This effect was found to be much less pronounced at higher temperatures where the diffusion rates are probably higher.

3.6 Modeling of the K_2 Slag + H_2 System

Typical output data obtained from the SOLGASMIX program for the K_2 slag in the presence of H_2 are given in table 2. Note that K is the predominant alkali vapor species, in agreement with experimental observation. However, the O_2 partial pressures are much less than those observed experimentally. It is also noteworthy that the K partial pressure is relatively temperature insensitive in the presence of H_2 and H_2O. This agrees qualitatively with the data presented for the K_1 slag system.

Table 2

SPECIES PARTIAL PRESSURES FROM NON-IDEAL SOLUTION[a]
MULTICOMPONENT EQUILIBRIUM CALCULATIONS FOR K_2 SLAG + H_2

Species	Pressure (atm) (1600 K)	Pressure (atm) (1700 K)
H_2	0.11 -3[b]	0.63 -4
H_2O	0.26 -3	0.27 -3
O_2	0.23 -9	0.77 -8
K	0.57 -3	0.60 -3
KOH	0.51 -4	0.55 -4
SiO	0.54 -8	0.31 -7

[a] K_2O activity coefficient specified as 10^{-8} and independent of temperature.

[b] Denotes e.g., 0.11×10^{-3}.

4. Summary and Future Directions

The present studies have resulted in the development of a new experimental technique, transpiration mass spectrometry, for the quantitative analysis of high temperature gases and vapors[2]. This technique has

---

[2] This development recently received external recognition in the form of an IR-100 award (1980).

been applied to vapor transport and thermodynamic activity determinations for real and synthetic coal slag samples in reactive coal gas components at atmospheric pressure. The results indicate a highly non-ideal and non-monotonic (with respect to temperature and composition) behavior for alkali metal vapor transport. Thus a priori predictions of alkali metal transport in coal gasifiers without actual activity data are virtually impossible at the present time. Surface segregation and diffusion limitations of alkali species in slags are also possible complicating effects.

Future studies should be made on a variety of typical coal slags in individual coal gas component atmospheres and then in the mixed gases. In view of possible non-equilibrium or transport-limited effects, studies should be made as a function of gas residence time and total pressure. Extension of transport measurements to pressures greater than one atmosphere is also desirable, particularly when non-equilibrium effects are rate controlling. It is unlikely that either experimental or modeling studies can stand alone for reliable prediction of coal gasifier materials durability problems; therefore, combined studies are needed.

5.   Publications and Talks

5.1 Publications

    a. Transpiration Mass Spectrometry of High Temperature Vapors,
        D. W. Bonnell and J. W. Hastie; Proceedings of the 10th
        Materials Research Symposium on Characterization of High
        Temperature Vapors and Gases; NBS, Gaithersburg, Maryland;
        September 18-22, 1978. NBS SP 561 (1979).

    b. Slag and Metal Oxide Vaporization in Reactive Atmospheres,
        J. W. Hastie, D. W. Bonnell, and E. R. Plante, High Temp. Sci.,
        in press (1980).

5.2 Talks

a. "Transpiration Mass Spectrometry Studies of the Thermal Decomposition and Sublimation of Sodium Sulfate," D. W. Bonnell and J. W. Hastie, 25th ASMS Conference, July 1977.

b. "Slag and Metal Oxide Vaporization in Reactive Atmospheres," J. W. Hastie, D. W. Bonnell, and E. R. Plante, Int. Colloq. on Use of Refractory Oxides for High Temperature Energy Sources, Toronto, Canada, July 1979.

c. "Vapor Transport of Coal Minerals and Slags," J. W. Hastie, D. W. Bonnell, and E. R. Plante, Symp. Coal Minerals Properties and Conversion, Materials Research Society, Annual Meeting, Cambridge, Mass., November 26-30, 1979.

d. "Transpiration Mass Spectrometry of High Temperature Vapors," D. W. Bonnell and J. W. Hastie, 10th Materials Research Symp. on Characterization of High Temperature Vapors and Gases, NBS, Gaithersburg, Maryland, September 18-22, 1978.

6. References

Eriksson, G. (1975). Chemica Scripta 8, 100.

Gordon, S., and McBride, B. J. (1971). Computer Program for Calculation of Complex Chemical Equilibrium Compositions, Rocket Performance, Incident and Reflected Shocks, and Chapman-Jonquet Detonations, NASA SP-273.

Hastie, J. W. (1973). Combust. Flame 21, 49.

Hastie, J. W. (1975). High Temperature Vapors: Science and Technology, Academic Press, NY.

Raymon, N. S., and Sadler, L. Y., III. (1976). Refractory Lining Materials for Coal Gasifiers, Information Circular 8721, U.S. Department of Interior.

Sadler, L. Y., III, Raymon, N. S., Ivey, K. H., and Heystek, H. (1979). Ceramic Bulletin 58, 705.
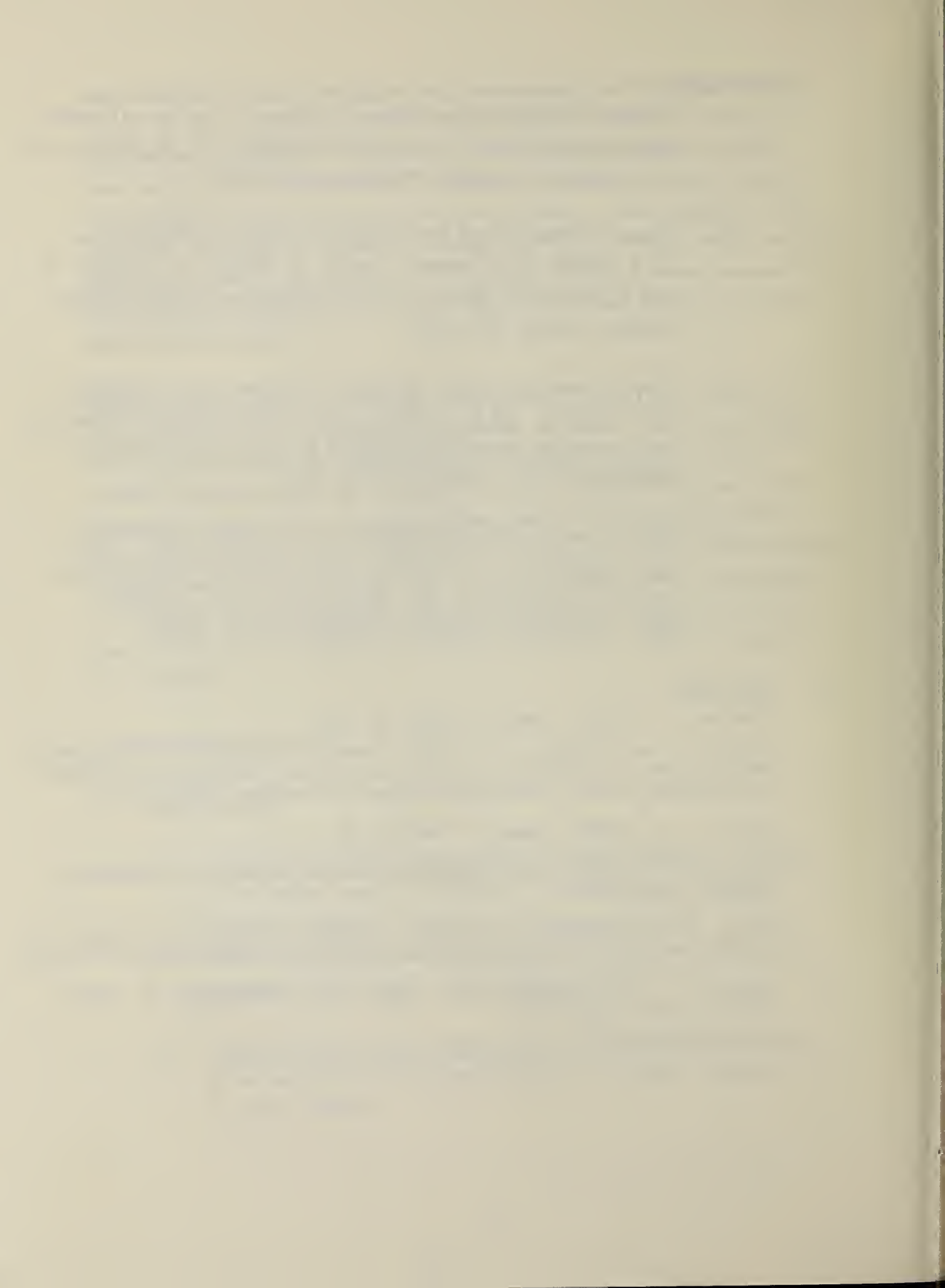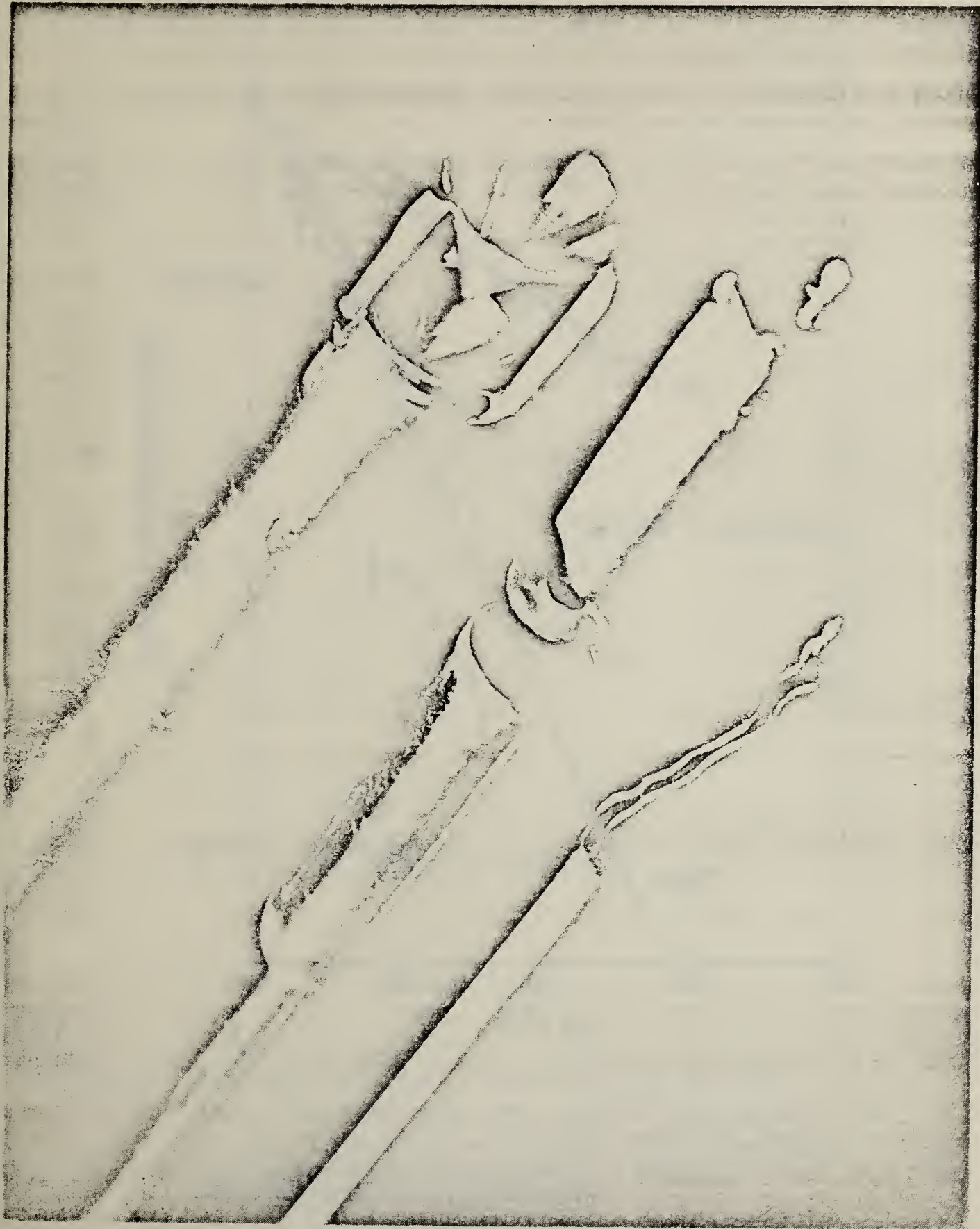
Figure 1. Photo of disassembled transpiration reactor showing the thermocouple,
sample boat, and transpiration tube with beam sampling nozzles attached.
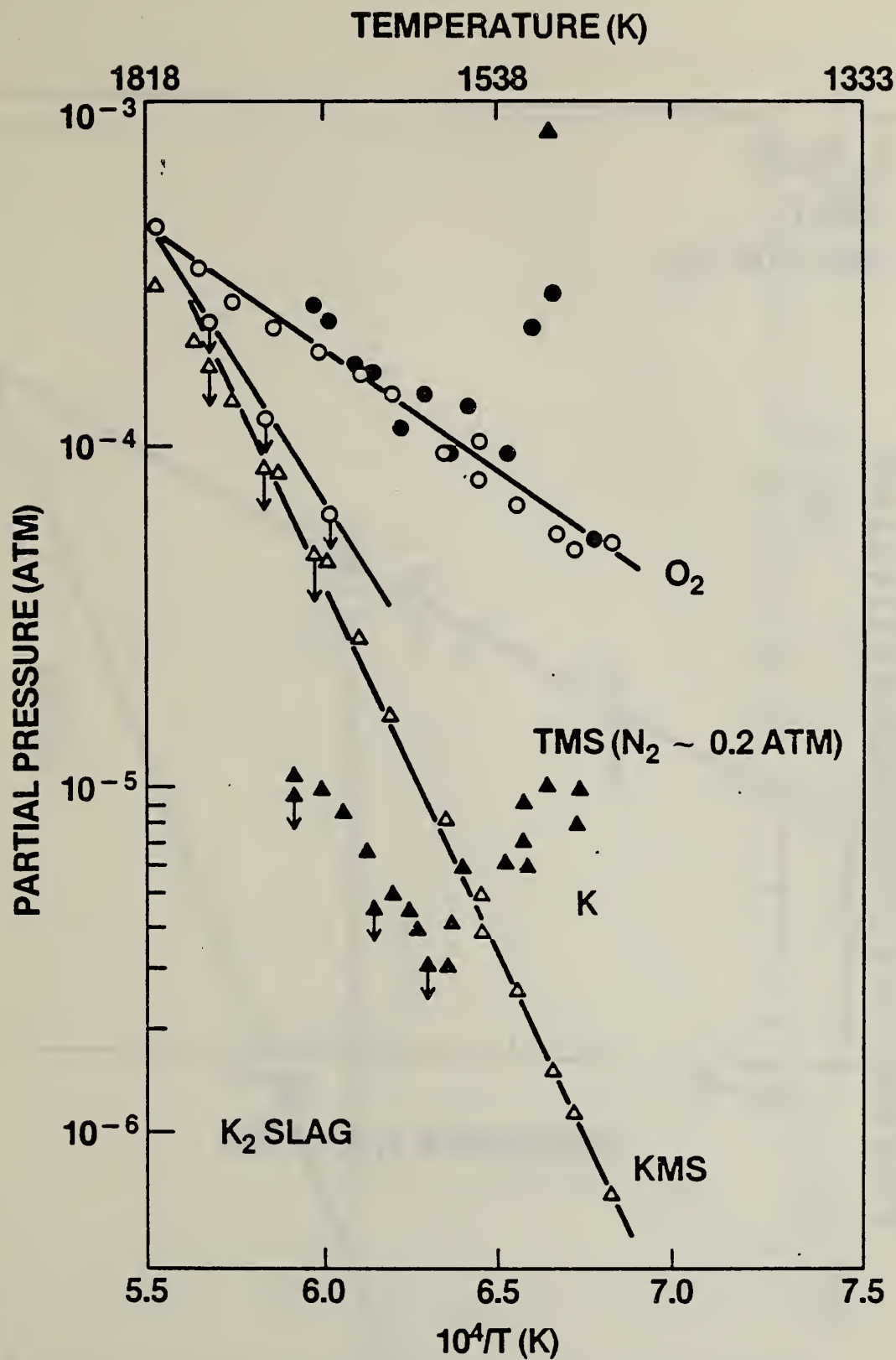
Figure 2. Vaporization of K and O_2 from the K_2 slag, expressed as log P vs 1/T plots: open circles--O_2 (KMS), closed circles--O_2 (TMS), open triangles K (KMS), closed triangles K (TMS). Chronological order of data taken with increasing temperature except for arrowed data points where the temperature was decreasing.
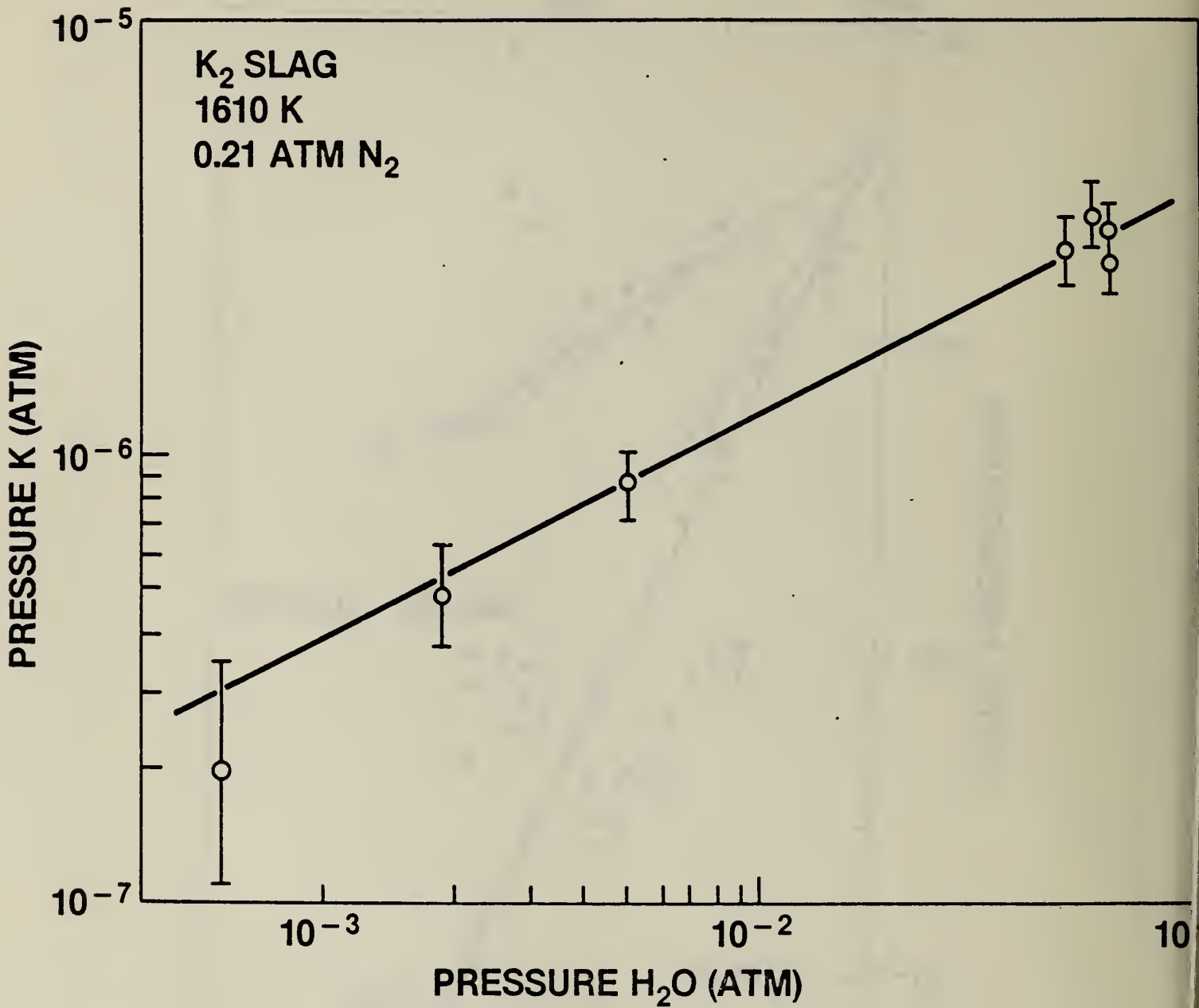
Figure 3. Dependence of K-pressure on H_2O-pressure at constant temperature for the K_2 slag (TMS data). The curve of slope 0.5 represents the theoretical pressure dependence for reaction (6) (see text).
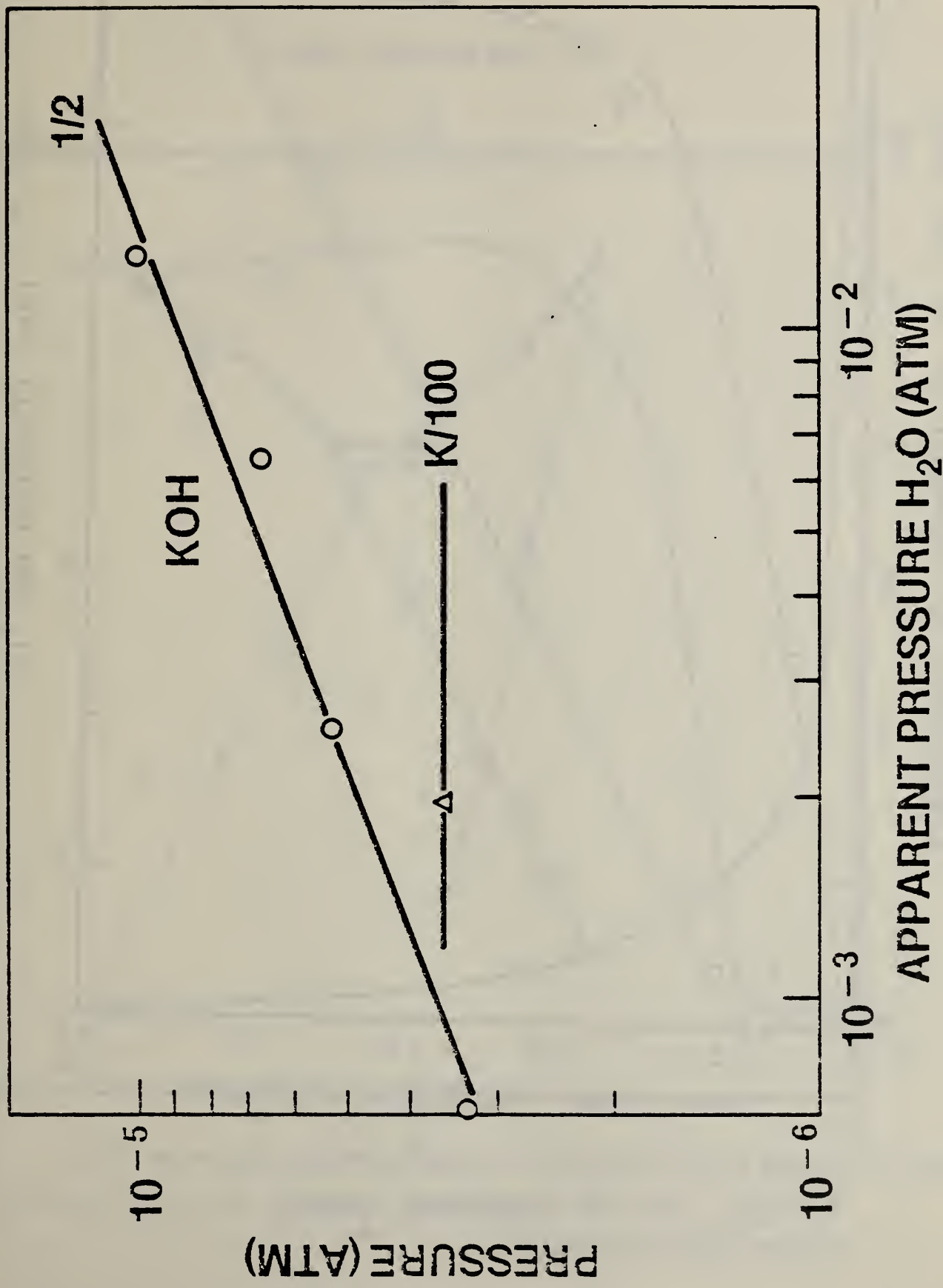
Figure 4. Dependence of KOH-pressure on H_2O apparent pressure at constant temperature for the K_2 slag at 1794 K (KMS data). The curve of slope 0.5 represents the theoretical pressure dependence for a process analogous to reaction (4).
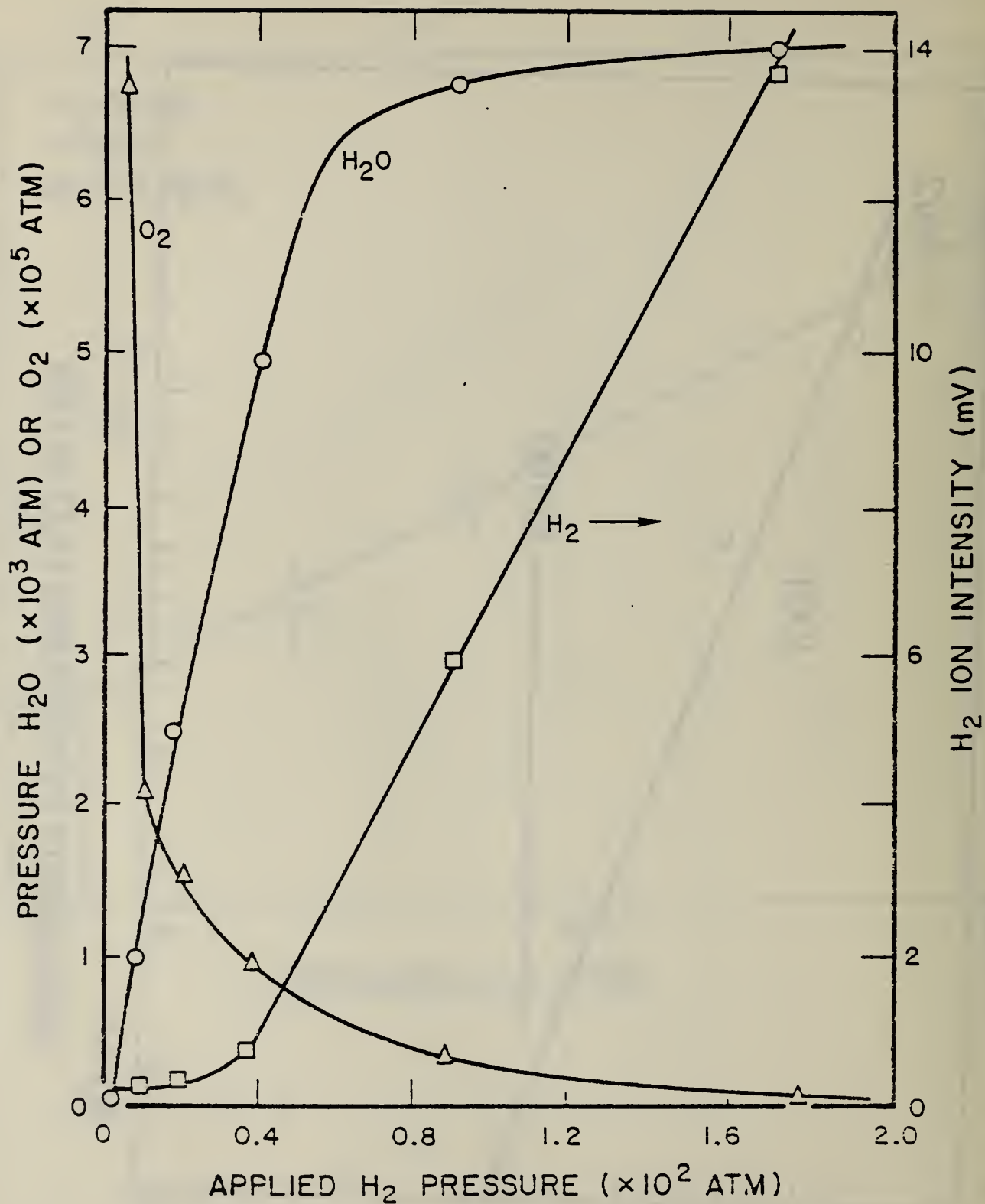
Figure 5. Reponse of K_2 slag system to added H_2, showing conversion of slag O_2 to H_2O. Conditions: temperature, 1655K; N_2 carrier gas pressure, 0.18 atm, capillary nozzle.
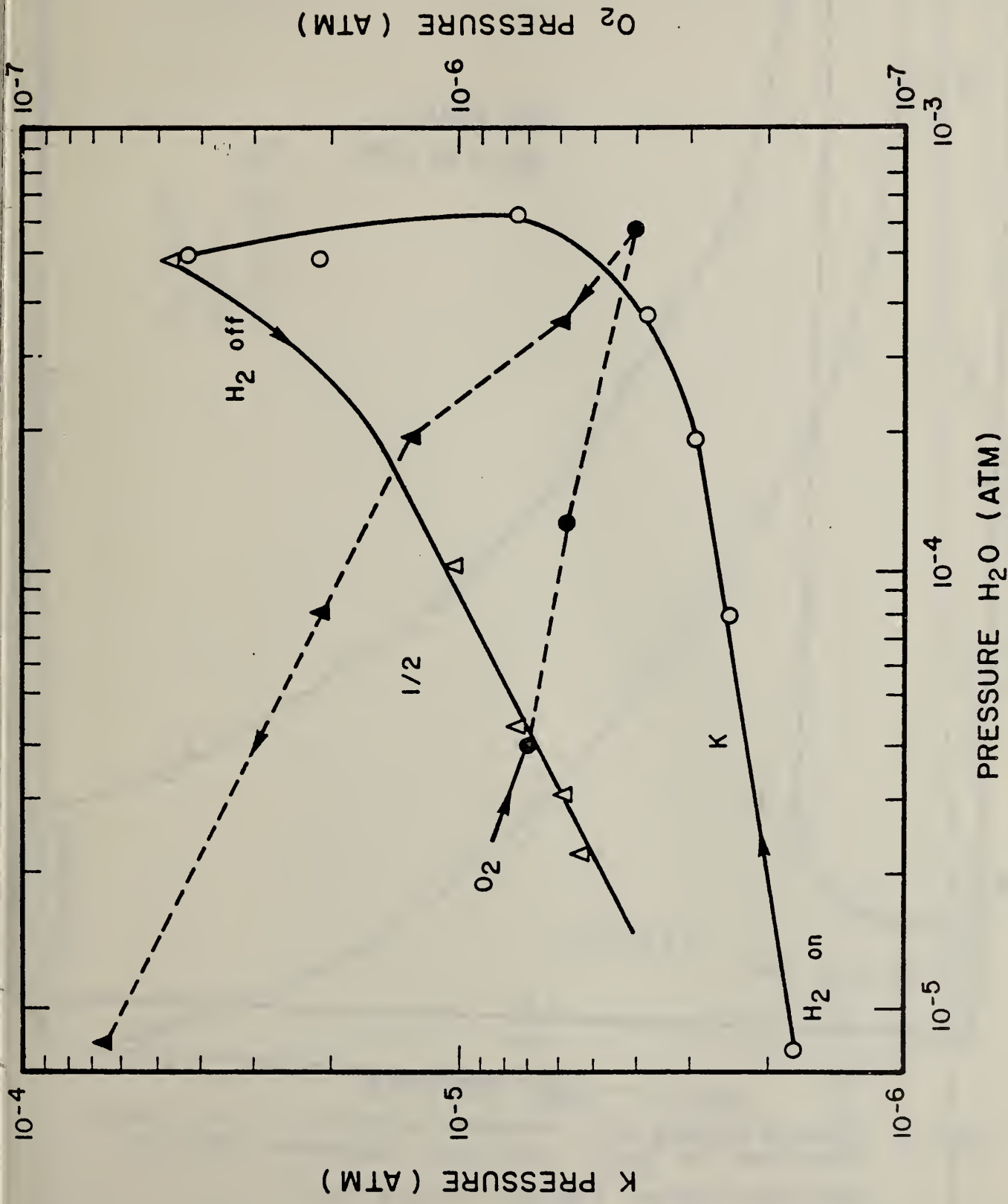
Figure 6. K-pressure (open symbols) and O_2-pressure (closed symbols) with H_2O-pressure for K_2 slag in the presence of added H_2. Conditions: temperature, 1655 K; N_2 carrier gas pressure, 0.18 atm., capillary nozzle.
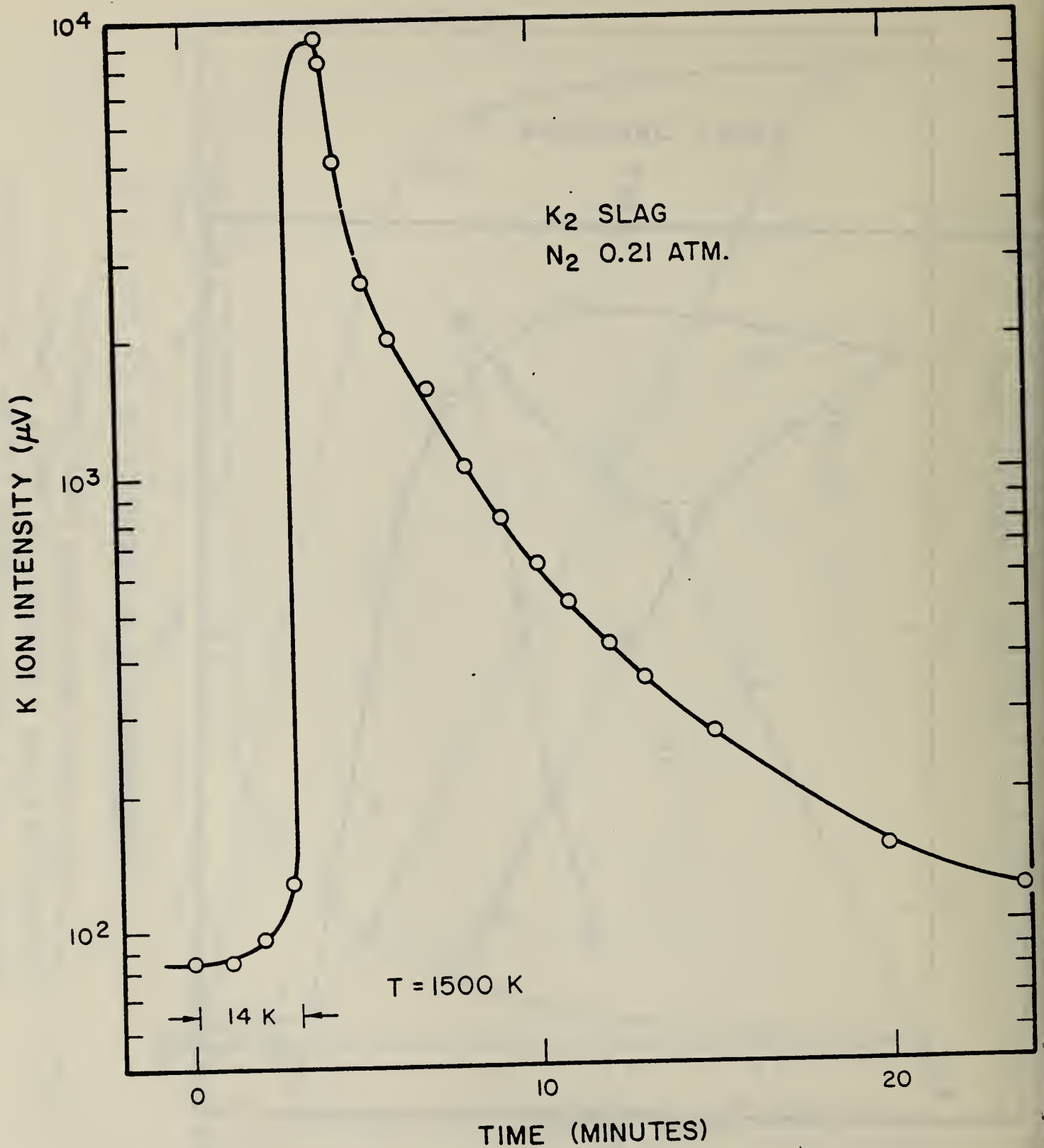
Figure 7. K-species pressure burst phenomenon, expressed as K$^+$ ion intensity versus time, for K$_2$ slag. Conditions: temperature, 1500 K; N$_2$ carrier gas pressure, 0.21 atm, capillary nozzle.
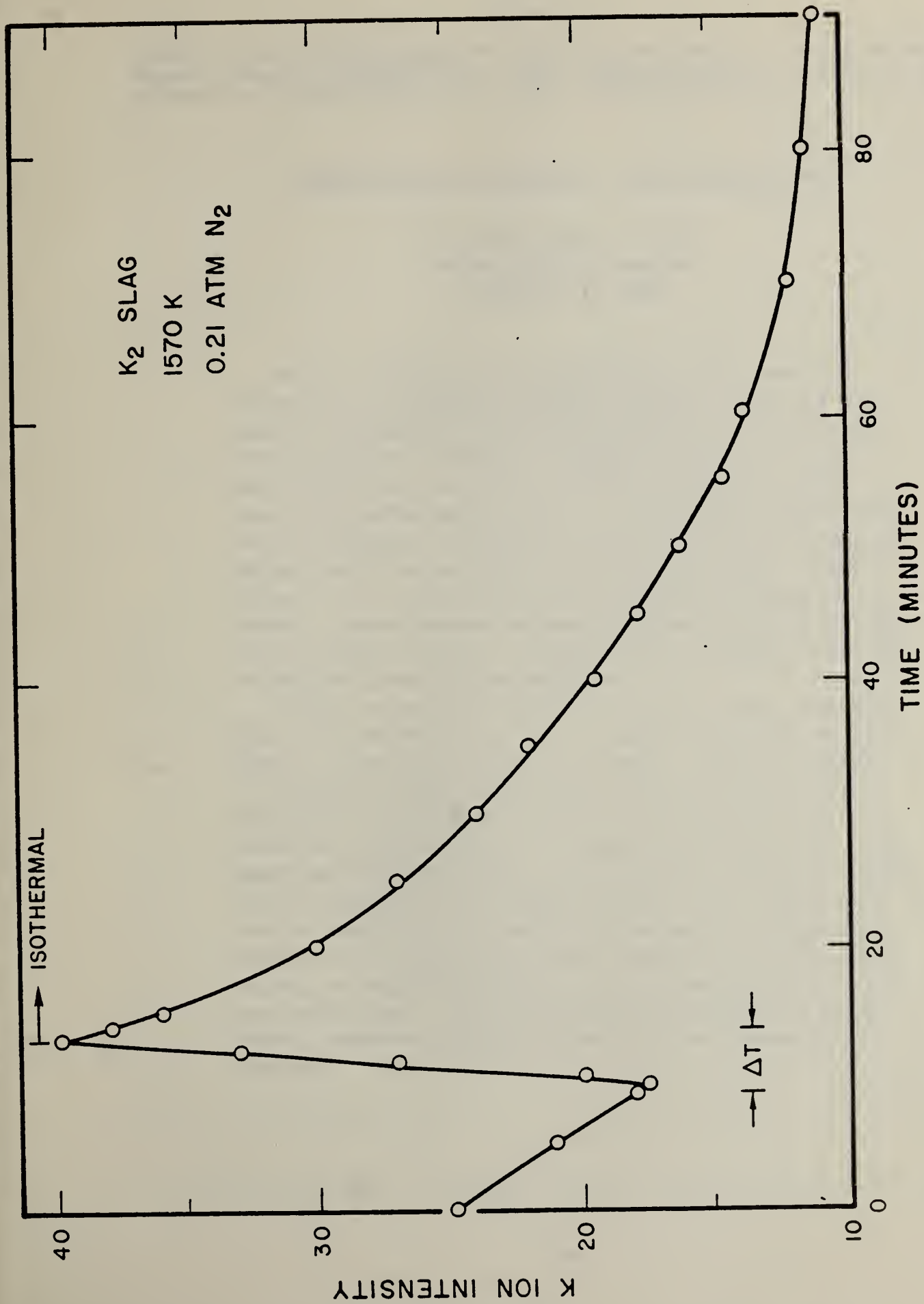
Figure 8. Typical K$^+$ ion intensity signal decay with time for K$_2$ slag. Conditions: temperature, 1570 K; N$_2$ carrier gas pressure, 0.21 atm, capillary nozzle.

Appendix A

TRANSPIRATION MASS SPECTROMETRY OF HIGH TEMPERATURE VAPORS

D. W. Bonnell and J. W. Hastie
National Bureau of Standards
Washington, DC 20234

Material transport via vapor phase species at high temperature and pressure is an important phenomenon in materials science and technology. The preparation of high purity semiconductor and ceramic materials utilizes vapor transport to advantage, whereas the corrosion of power plant boilers, gas turbines and other advanced energy devices results from reactive vapor transport. To understand and control these transport phenomena, it is essential to be able to identify and measure the key chemical species present in the vapor phase systems. However, in the past, classical characterization methods such as transpiration and Knudsen or Langmuir effusion have been limited because they do not establish the molecular identity of transport species or because low pressures are necessary to make effusion measurements.

We have developed a new technique - Transpiration Mass Spectrometry (TMS) - that overcomes both of these limitations by combining the basic features of transpiration and mass spectrometry. With this technique, it is possible to sample reactive gases directly from high-temperature, high-pressure atmospheres for qualitative and quantitative characterization with a mass spectrometer. To demonstrate the method, the thermodynamic equilibrium vaporization of the salts Na_2SO_4 and NaCl was studied at total pressures up to an atmosphere using N_2 or Ar as carrier gases. The molecular composition of the vapors was determined over a wide range of temperature and pressure and the results indicated no measurable perturbation of the vaporization equilibria due to the presence of a molecular beam sampling probe. In fact the accuracy of data obtained by the TMS method is competitive with that of established, lower dynamic range, techniques.

1. Introduction

1.1 Technological background

Many high temperature processes of technological importance rely upon, or are adversely affected by, chemically active heterogeneous subsystems. One such case involves chemical interaction of a multicomponent high temperature (e.g., ~500-2000 K) high pressure (e.g., ~0.1-100 atm) gas mixture with a solid or liquid substrate. This interaction frequently leads to the formation of intermediate species containing elements of both the gaseous and substrate materials. These reaction intermediates can be transported in the presence of temperature, concentration, or momentum (e.g., forced convection) gradients. Transport to another regime of temperature, pressure, or concentration can lead to a reaction-reversal or the introduction of secondary processes. In many instances, this changing chemistry along gradients results in a deposition of intermediate species with the overall result that the initial substrate has been physically transported to another part of the system.

Such material transport can have either an undesirable or beneficial effect on the system of interest. Examples in modern technology include, respectively:

(1) Hot corrosion of gas turbines, jet engines, rockets, coal gasifiers, magneto-hydrodynamic channels, coal fired boilers, and numerous pyrometallurgical systems.

(2) Controlled material transport for production of crystals and films, extractive metallurgy, flame inhibition and fire extinguishment, combustion modification such as smoke and antiknock control with additives, and regenerative lamp cycles.

A detailed recent discussion of these and other examples of high temperature materials transport has been given elsewhere [1][1].

In order to understand these heterogeneous processes for development of new or improved control strategies, it is necessary to define at a molecular level the transport mechanisms and particularly the reaction intermediates. To date, extensive reliance has been placed on speculation and empirical observations based solely on macroscopic variables defining the initial and final state of the system. For instance, current understanding of hot corrosion derives from metallurgical examination of the clean and corroded material under ambient conditions. Extrapolation of these observations to the actual conditions of usage requires many assumptions about the corrosion mechanisms. However, detailed mechanistic information is practically nonexistent. A further inaccuracy occurs because standard test procedures (e.g., use of laboratory burner rigs) simulate only part of the actual system. To properly relate test results to practical usage would require a knowledge of scale-up factors derived from a detailed mechanistic description of both the test and the end-use systems.

Information on reaction mechanisms, including the intermediate transport species, has been practically nonexistent heretofore because of the measurement problems associated with these extreme conditions. Very limited molecular-specific information can be obtained using optical spectroscopic methods at high temperature and pressure. In principle the broad spectrum of gaseous and vaporized species present could be identified and their spatial and temporal concentrations determined by the high pressure sampling mass spectrometric (HPMS)

---

[1]Figures in brackets indicate the literature references at the end of this paper.

technique. This molecular beam technique, which uses a sonic nozzle for sample extraction, has been amply demonstrated by us [2] and others for homogeneous systems, including flames. A summary of recent work in this area has been given by Stearns, et al. elsewhere in this volume [3]. For heterogeneous systems, the gas is saturated by condensible species. In this case, the nozzle probes used to interface the hot gas and the mass spectrometer become part of the reaction system and severe limitations arise. Conventional use of the HPMS technique (homogeneous systems) has required probe temperatures to be considerably less than for the sample system. With saturated gases, this leads to condensation of inorganic species at the probe tip and results in physical blockage of the small entrance orifice or in corrosive loss of the probe.

We have developed a procedure for avoiding this difficulty, in addition to providing other advantages, as described in Section 2. Basically, the sample, probe and skimmer (to a lesser degree) are maintained isothermal by an external heat source. Maintenance of a steady state (and constant pressure) between gas and substrate requires a continuous replenishment of the gas extracted by the sampling process. This leads naturally to a transpiration procedure, where the input flow rate matches the gas extraction rate through the small-orifice probe. The technique therefore combines the basic features of both the transpiration [4] and the HPMS methods.

1.2 Scope of application

In the following sections we describe this technique of transpiration mass spectrometry (TMS) and its application to the characterization of high temperature vapors. We have demonstrated that it is a nonperturbing method[2], which is always an important concern with probe methods. The method extends the dynamic range of classical vaporization and vapor transport techniques by many orders of magnitude; at least four orders with respect to Knudsen effusion mass spectrometry. We believe that TMS should be applicable as a quantitative measurement tool for laboratory simulations of most of the technological transport systems mentioned above and eventually may be applicable to plant-scale systems.

With regard to systems of initial academic interest, one can most likely expect this technique to be a useful means of producing novel high temperature species in a spectroscopically cool form, resulting from free jet expansion cooling. This would greatly extend the utility of thermally sensitive molecular beam spectroscopic methods. In particular, electron diffraction, microwave, laser fluorescence, Raman, photoelectron, and photoionization spectroscopy, as well as matrix isolation methods, would benefit from a coupling with the TMS technique. The extended high pressure range should also allow for the study of basic thermodynamic properties of novel complexes and adducts of the type suggested indirectly from gas-solid solubility studies (e.g., see Hastie, pp. 126-148; pp. 73-87 [1]). Future extension to even greater pressures should permit definitive molecular characterization of systems in their critical state and greatly supplement equation of state studies and the fundamental understanding of fluids.

---

[2]At least for the equilibrium systems studied, and this is most likely the case for many nonequilibrium systems.

2. Apparatus

2.1 The mass spectrometer system

Figure 1 shows a schematic of the mass spectrometer (stage II) and vacuum system layout with the transpiration apparatus attached (stage I). The aluminum walled vacuum system is partitioned into two differentially pumped stages. The stage labeled I utilizes a 6 in diffusion pump (Varian/NRC VHS-6)[3] with a cold trap (Granville-Phillips Model 270-6) and gate valve (NRC 1279-6) close-coupled to the base of the vacuum chamber. Net pumping speed at the bottom of the chamber is calculated to be $\sim$800 l/s. The backing system for this pump-stack uses a Roots blower (Leybold-Hereaus WA250) and a rotary two stage vane pump (Sargent-Welch 1375). Use of a blower in series maintains, even for high gas loads, a pressure at the diffusion pump outlet well below the $\sim 10^{-4}$ atm[4] critical backing pressure. This assures that the diffusion pump will continue to pump near its rated speed into the 10^{-5} atm pressure range. A high sensitivity thermocouple gage controller (Hastings-Raydist model SL-1R) and tube (type DV-8M) was used to monitor this pressure range.
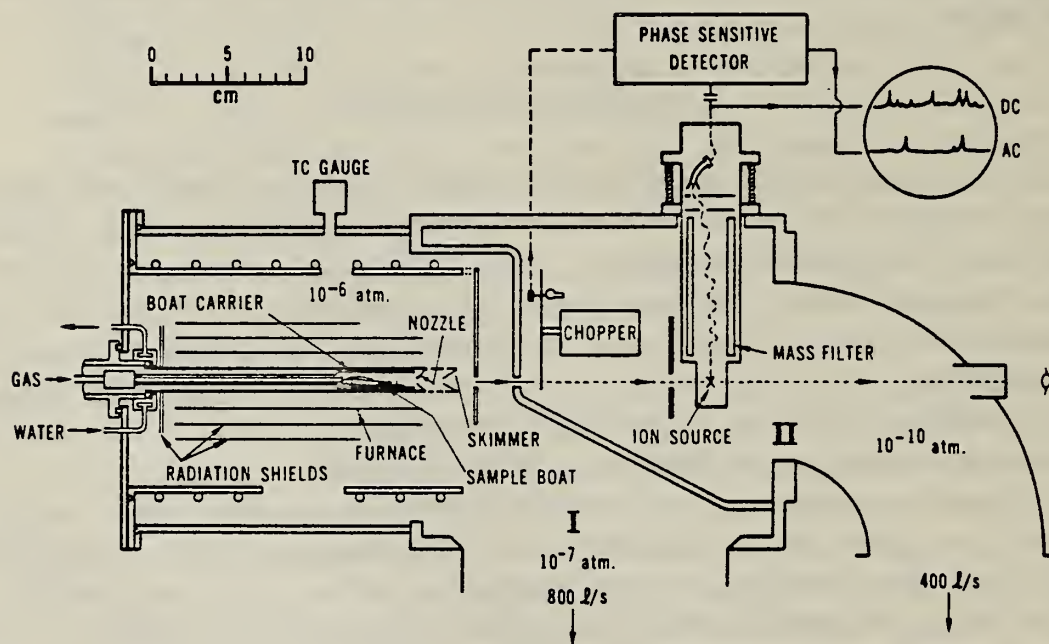
Figure 1. Detailed schematic of assembled transpiration reactor-mass spectrometer system.

---

[3]Commercial sources are identified only for purposes of accuracy and do not imply endorsement by the U. S. Government nor that they are the most suitable product for the work performed.

[4]1 atm = 1.01325 x 10^2 kpascal; see introduction to this volume for SI unit conversions.

A mechanical shutter separates stages I and II, acting as a valve to isolate the stages during removal of the transpiration reactor assembly. In addition, there are a variety of differential pump apertures (three hole sizes) in the shutter plate for control of the molecular beam diameter and stage I to II pressure difference. The aperture used for transpiration experiments is 0.05 cm in diameter and is located 4 cm from the skimmer orifice.

Stage II, the high vacuum mass spectrometer section, is pumped by a stack consisting of a 4 in diffusion pump (Varian/NRC VHS-4), a 4 in cold trap (Granville-Phillips Model 270-4) and a butterfly valve (Vacoa BFV-4). This stage has an approximate pumping speed of 400 l/s at the vacuum chamber base. No-load vacuum in both stages is $<5 \times 10^{-11}$ atm. The background mass spectrum at this pressure shows the 18 amu (H_2O^+) ion as the major peak ($\sim$50 percent of total ions) which arises from H_2O desorption from the aluminum-walled vacuum system. At maximum load ($\sim$50 sccm [standard cubic centimeters per minute]) the stage I and II pressures are $\sim 5 \times 10^{-6}$ atm and $\sim 5 \times 10^{-9}$ atm, respectively. A titanium sublimation pump (Granville-Phillips TSP series 287 in a 214-669 chamber) and an ion pump (Ultek Model 10-250), not shown in figure 1, are used as holding pumps on the stage II section when the diffusion pump is valved off to cycle the cold trap. This periodic trap cleaning procedure minimizes release of trapped reactive gas back into the mass spectrometer chamber.

The beam modulation chopper system, located in the stage II region, is a toothed wheel (3 or 24 teeth) driven by an AC synchronous motor (Globe 75-121-2) which has been cleaned for vacuum service. A reference signal, needed for phase sensitive detection, is generated by the wheel interrupting light from a small incandescent bulb (GE number 40) impinging on a photo transistor (GE-L14B). A sine wave oscillator (Donner model 1202) supplies the drive frequency to a chopper drive system [Extranuclear Laboratories (EL)] which produces the capacitively shifted two phase 115 V power to drive the chopper motor. The three tooth chopping wheel yields beam modulation frequencies from $\sim$40 to 270 Hz. Higher frequencies can be obtained with the twenty-four tooth wheel. The actual chopping frequency is normally selected by observing a very weak modulated beam mass spectral peak and adjusting for minimum noise interference from the 60 Hz line frequency. For these studies a chopping frequency of 214 ± 1 Hz was used.

The mass spectrometer itself is a quadrupole mass filter (EL-Model 270-9) with a crossed-beam configuration ion source (EL Model 041-2). We have modified the commercial ion source by mounting a stainless steel plate at the ion source entrance for additional neutral beam collimation. Standard quadrupole power supply (EL model 011-1) and ionizer control electronics (EL type II) are used. The mass analyzed ion beam is deflected to a channeltron electron multiplier (Galileo Electro-Optics, model 4700) mounted off axis and operated at a nominal 1700 volts dc. Since the final amplifier is a frequency and phase sensitive lock-in detector (Ithaco Model 393), the multiplier gain is set for optimum signal to noise ratio at the lock-in, rather than for maximum gain. Total system gain using a fast electrometer amplifier (EL Model 031-2) is $\sim 4 \times 10^{11}$; signal to noise, rather than total signal being the sensitivity limiting factor.

This mass filter system is supported by a 6 in flange (conflat) mounted on a large welded bellows assembly which allows three-axis positioning of the ion source entrance

aperture. In practice, a pinhole and collimator alinement assembly is mounted on the beam axis with a He-Ne laser directed along the same axis. The mass filter assembly is then positioned so that the ion source entrance and exit apertures are centered on the laser beam. Final molecular beam alinement is achieved by adjusting both the mass spectrometer and the molecular beam source angle position to obtain maximum ion intensity of a non-scatterable beam component. This alinement procedure proved to be a critical phase of the experiment.

2.2 The transpiration reactor

The transpiration reactor is located in stage I of the overall assembly (see fig. 1). Essential features of this reactor include: a sample container or boat, a boat carrier, a thermocouple for temperature measurements, a carrier gas inlet system, and a gas extraction system or probe. The boat carrier allows for boat removal from the reactor without need for a complete disassembling of the transpiration system. Molecular beam sonic probes are typically conical nozzles with design details determined by reasonably well established gas dynamic criteria, as outlined in Section 3. However, for highly reactive systems, we also found it desirable to develop a relatively more robust capillary probe, at the possible expense of sampling fidelity. Pertinent gas dynamic considerations for this type of probe are given in Section 2.3. Below we describe the construction details of these probes and the transpiration assembly in general.

2.2.1 Reactor internal details

Figure 2 shows a schematic view of a typical transpiration reactor assembly, including details of the assembled boat carrier and boat. A platinum tube, with outside diameter 1.23 cm, wall thickness 0.075 cm, and length 5 cm is used as a boat carrier. This tube has machined ridges at each end to allow a snug fit with the main chamber walls for prevention of diffusion losses. Welded to the rear of the carrier is a section of 0.64 cm diameter platinum tube through which the carrier gas passes. This carrier gas tube is sealed to an SS304 1/4 in stainless steel tube via a SWAGELOK joint machined to fit inside the 1.27 cm i.d. of the main chamber. The seal is 21 cm from the front of the boat carrier. This long path length allows the gas to reach thermal equilibrium with the walls before interacting with the sample. The platinum section of the carrier gas tube also serves as a guide for introduction of an alumina sheathed Pt-Pt/10 percent Rh thermocouple to the sample area.

The boat, which is fabricated from welded platinum sheet, has a slanted base ($\sim 5°$ to the front) to allow liquid samples to be preferentially retained in the front of the boat (fig. 3). The gas baffle shown in figure 2 is located ~ 0.75 cm behind the boat, and serves to interrupt the fast gas flow into the boat region, thereby allowing the gas maximum time to equilibrate thermally before passage at a relatively slow rate over the sample. The baffle also supports the tip of the alumina thermocouple sheath so that only bare wires are brought into the boat region, thereby minimizing exposure of potentially reactive ceramic to the system.
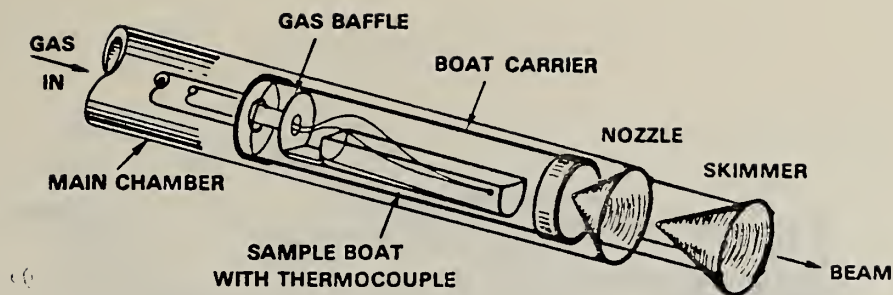
Figure 2. Transpiration reactor showing internal details.

2.2.2 Conical sampler

Details of the nozzle-skimmer arrangement are shown in figure 3. Nozzle cones are constructed by alternate pressing and heat annealing of thick platinum disks (2 cm x 0.1 cm) in steel dies until a 45° half angle cone with a relatively sharp tip (~0.1 cm radius) is obtained. Minor surface machining is followed by ELOX drilling of a hole in the tip to achieve an orifice 0.006-0.009 cm in diameter with a maximum hole channel length of 0.004 cm. The tip exposed to the source gas normally has a flat face ~0.1 cm wide. We discontinued use of knife edge machined nozzles since they occasionally failed in service due to cracking in the wall close to the orifice. Experience showed that gas leaking through such cracks created serious disturbances in the expanding gas flow and sufficiently disrupted the trajectory of the initial high intensity jet to lower its density, after passage through the skimmer, by three to four orders of magnitude. We believe that micro cracks originate during the cone-forming and machining process and that these cracks propagate as a result of the combined effects of thermal cycling under pressure and reactive gas mixtures (nonoxidizing). The design of a sturdier probe (snubnosed), such as that depicted in figure 3, avoided this problem which was particularly severe for slag and strongly basic samples.

The skimmer (shown in fig. 3) was fabricated in a manner similar to the nozzle, using 30° half angle dies. Finish machining specified a sharp-edged hole since cracking would not be a problem and minimal flow disturbance is mandatory for skimmers. The skimmer hole was drilled with a high speed twist drill (number 69-0.074 cm). Clogging of the skimmer was a primary concern in the use of supersonic beam sampling, since at high temperatures and source pressures a single experiment could be expected to deposit condensable material on a cool skimmer at a rate of several hundred mg/hr. Such deposits were avoided by physically attaching the skimmer to the nozzle assembly with thin platinum support struts (not shown in fig. 3). Skimmer temperatures were then within 50 K of the nozzle temperature. This arrangement also provided an essentially permanent alinement of skimmer and nozzle.

363
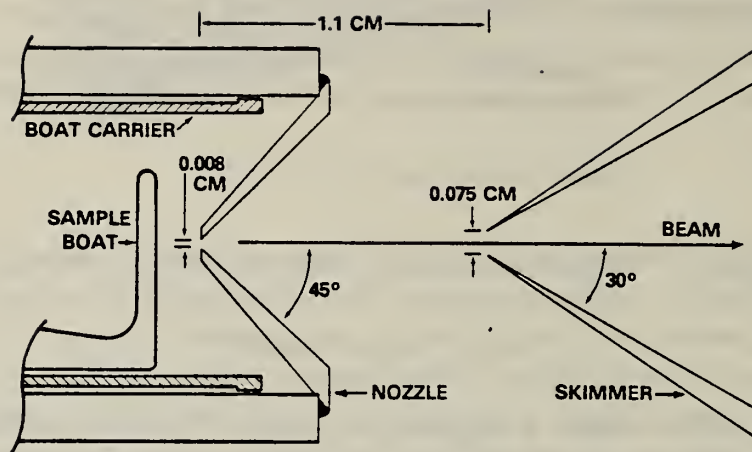
Figure 3. Schematic of conical sampler construction details and relative
location of internal components. Forward edge of skimmer is attached to
outer edge of chamber exterior with 3 thin (0.2 cm thick) platinum struts
(not shown in fig.). For clarity, not all dimensions are drawn to scale.

2.2.3 Capillary sampler

A capillary sampler, shown in figure 4, was fabricated to be interchangeable with the
conical nozzle-skimmer assembly. Note the absence of a skimmer with the capillary method.
This omission was possible since beam velocity distribution measurements [5] with short
channels (length to orifice diameter ratio of 2) and no skimmer have indicated formation of
a well developed isentropic expansion leading to a high Mach number supersonic beam. Our
longer channel (corresponding ratio of 30) capillary also produces a good quality supersonic
beam (see Section 3.4.2).

Capillary fabrication involved first welding a 0.32 cm diameter platinum rod to the
center of a 2 cm x 0.1 cm thick platinum disk. Then, using a 0.013 cm wire, a hole was
drilled from the disk side by the ELOX process to a depth of ∿0.5 cm. Overcut from the ELOX
process produced a converging capillary, as shown in figure 4. The rod was then cut at the
bottom of the hole and crushed in steel dies to reduce the hole to the approximate dimensions
shown (see fig. 4). ELOX machining smoothed any irregularities from the postforming process.
The entire assembly was then welded to the main chamber tube, using a jig to maintain proper
alinement. System alinement procedure was essentially identical to that used for the conical
sampler system.
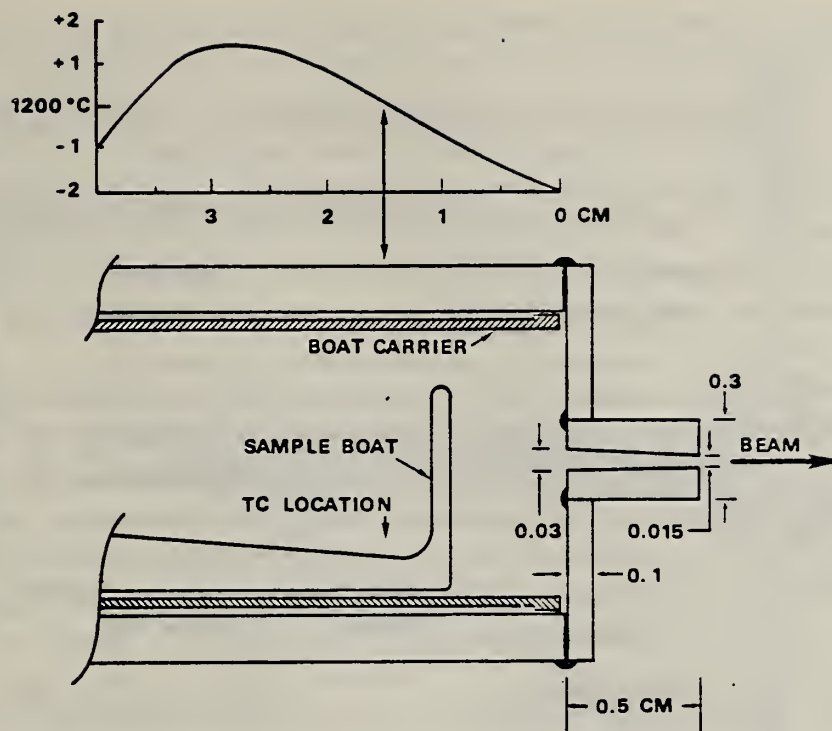
Figure 4. Schematic of capillary sampler showing construction details and relative location of internal components. Channel not drawn to scale for clarity. A typical temperature profile, obtained along the central axis of the chamber, is also shown.

2.2.4 Reactor external details

The complete transpiration assembly is shown in figure 5. Attachment to the support flange is made with a 1.59 cm (commercial 5/8 in) CAJON O-ring fitting. Initially a large stainless steel SWAGELOK fitting was used to make this connection, but differential expansion on heating caused unacceptable leaks. To protect the VITON O-ring from thermal degradation, the CAJON nut was water jacketed. A rigid connection was provided by compressing a machined ridge (an integral part of the main chamber) between the nut and O-ring. With this protection, the system could operate even at the ∿1700 K maximum temperature for many hours. However, the large temperature gradient resulting from the location of this water cooled connection only 15 cm from the sample area, required careful optimization of the position of the Ta foil furnace and its radiation shields. By careful positioning of a partial shield (see fig. 5) at the rear of the furnace, it was possible to control the temperature gradient to <10 K over the length of the boat (3 cm) at the highest operating temperature. Gradients between the thermocouple location and the nozzle were much less, as shown in figure 4, and constituted a negligible source of experimental error.

365
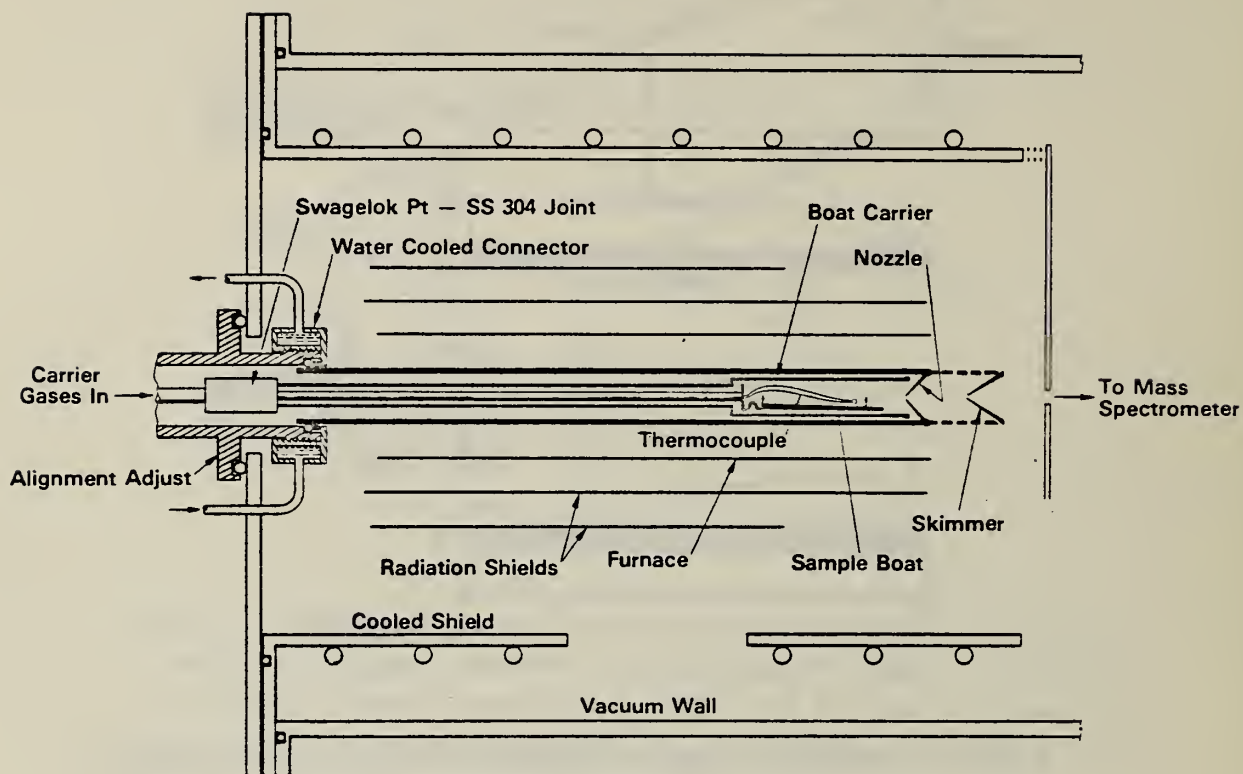
Figure 5. Transpiration inlet assembly showing details of furnace,
radiation shield and assembly proportions.

The main body of the furnace is supported by water cooled bus bars (not shown in fig. 5) which are sealed to the support flange via SWAGELOK compression of TEFLON sleeves against the bus bars. Power to the furnace is supplied by a 208 V, 20 amp variable autotransformer driving a 20:1 stepdown transformer. Typically, 250-300 amperes is required to attain 1700 K. Precise temperature adjustment with this arrangement is only marginally acceptable. However, alternative use of phase angle fired controllers creates unacceptable noise in the mass spectrometer signal amplifier circuit, and zero crossing controllers cannot fire into the inductance presented by the stepdown transformer. Several remedies to improve temperature control are under investigation.

A water cooled copper jacket surrounding the furnace assembly condenses high temperature species scattered by the skimmer. The front plate of this jacket is mounted on copper stand-off legs to improve pumping access to the furnace region (see fig. 5). The entire transpiration assembly is flange mounted and attached to the vacuum system as a unit, as shown in figure 1.

2.3 Reactor alinement

Alinement of the skimmer to the nozzle is performed by mounting the sampler (i.e., transpiration reactor) assembly in a jig with the same type CAJON fitting used for the vacuum seal at the support flange. This jig is carefully machined to have a rear face perpendicular to the sampler axis. A small He-Ne laser is then alined by reflection to project its beam parallel to the sampler axis. The laser is then translated, maintaining parallelism, until the beam is centered on the orifice. It is then a simple matter to deform the skimmer struts slightly to obtain a visually perfect circular diffraction pattern through the skimmer. This adjustment is very sensitive and can detect alinement errors of a few hundredths of a milli-meter.

Approximate centering of the sampler on its support flange is achieved by translating the entire sampler on its mount until the nozzle-skimmer-line is centered in the aperture of the front plate of the water cooled shield. This initial alinement is facilitated by shining a light down the sampler and positioning the light viewed through the nozzle and skimmer. With the entire assembly mounted and evacuated, a final tuning of the initial alinement is made by telescopic observation of the light passing through the nozzle, skimmer and mass spectrometer ion source. The sampler is then centered on the differential pump aperture (separating stage I and II). Final alinement is achieved by moving the quadrupole mass filter assembly and adjusting for maximum observed beam intensity. This is a very minor adjustment, requiring movement of the mass filter by less than 1 mm.

2.4 Carrier gas system

Mass flow meters (Tylan Corporation model FM 360) and mass flow controllers (Tylan model FC 260) are used to provide carrier gas and mixed gas flow to the sampler. The flow con-trollers are slaved electronically to the carrier gas output to ensure constant and repro-ducible (±0.5 percent) gas mixture compositions. These mixtures can contain from 40 to 2 x 10^5 ppm of each of as many as three solute gases in the carrier gas stream. Flow controller ranges can be readily changed from 0.2-10 sccm to 20-1000 sccm to achieve these dilutions. During a transpiration run, gas flows of typically 3-30 sccm are used. The flow meter con-trollers are calibrated against a mercury piston volume gage to better than 2 percent absolute sccm. The mixed gases are metered to the sampler through a rotameter-type flowmeter (Matheson series 600; 602 flow tube) and valve (NRS number 1). Before passage through this flow meter, excess carrier gas is exhausted through a metering valve and a fixed differential pressure check valve to a hood system. The total gas pressure at the sampler inlet is measured by a capacitance pressure transducer (Rosemount model 1332A4, 0-30 psia) calibrated to read directly in atmospheres. Gage sensitivity is 0.002 atm and long term accuracy is ±0.003 atm (0.15 percent).

3. Gas Dynamic Aspects of High Pressure Sampling

The design of an effectively non-perturbing high pressure molecular beam sampling device, and subsequent data analysis, relies heavily on fundamental gas dynamic principles. In deciding on an optimum nozzle (probe)--skimmer geometry, consideration must be given to system pumping capacity, source pressure and temperature, desired beam intensity, and the characteristic thermodynamic and dynamic properties of the sample gas. Stearns, et al., elsewhere in this volume [3], have discussed this subject in some detail and cited the pertinent literature. The following treatment deals primarily with those aspects necessary to system design and data analysis considerations.

Following the landmark paper of Kantrowitz and Grey [6] which suggested that intense molecular beams could be obtained from small supersonic nozzles, a number of theoretical and experimental verifications [7-11], have laid the groundwork for extending this technique to studies of high pressure-high temperature systems. The primary advantages over conventional effusive techniques provided by the use of a supersonic beam source are, enhanced beam intensity resulting from the use of higher source pressures, and the narrower angular distribution (better beam collimation) obtained as a consequence of the conversion of random thermal motion to ordered motion in the expansion process. A possible disadvantage results from changes in the distribution of translational velocity, rotational and vibrational populations during the initial free jet expansion stage.

3.1 Free-jet relaxation effects

Factors affecting the final beam characteristics include: the nature of the free-jet expansion process (e.g., time to reach a collision free condition), down-stream effects (shock boundaries, background pressure, geometry, etc.), and the gas heat capacity(s). Inferences made concerning pre-expansion source conditions (i.e., composition of the sample gas of interest) from observations on the final molecular beam are highly dependent on an awareness of these factors and their relationship to source conditions and system design.

3.1.1 Relaxation of internal modes

In the supersonic sampling process, isentropic conditions generally govern the gross mass flow characteristics of the beam (pressure, temperature and density). In an excellent review article, Morris [12] discusses relaxation phenomena under isentropically expanding hypersonic conditions. Using the Navier-Stokes equations, which have been shown [13] to satisfactorily describe the flow properties, Morris [12] estimated the translational relaxation time τ_t for rigid non-attracting spheres to be

$$\tau_t = 5/4 \ \tau_c \qquad ,$$

where τ_c is the mean collision time based on the number of gas collisions. By assuming that molecular collisions are non-adiabatic with respect to rotation, it can be shown that rotational relaxation should readily occur. Experimental data for simple molecules such as N_2, NH_3, and CH_4 indicate the ratio

$$\tau_r/\tau_c \; <50, \text{ where } \tau_r = \text{rotational relaxation time.}$$

Even H_2 relaxes rotationally in 400 collisions. As the collision controlled expansion time is of the order of 10^{-7}s, for the rapid expansions typical of the supersonic sampling process, both the translational and rotational degrees of freedom are essentially equilibrated [3].

On the other hand, vibrational relaxation is a relatively much slower process with times ranging from 10^2 to 10^7 τ_c [12]. Higher temperatures should increase the vibrational relaxation rates. Only binary collisions appear to be important and polyatomic species typically have a single characteristic vibrational relaxation time. For the very fast expansions characteristic of supersonic sampling, the degree of vibrational relaxation depends mainly on the gas mixture used and may vary for different constituents. Bray [14] points out that the falling temperature and pressure as the gas passes through the nozzle both tend to increase the vibrational relaxation time, and the vibrational temperature can be represented by a sudden freezing approximation.

3.1.2 Chemical relaxation

Chemical relaxation is of paramount concern in the application of free-jet expansion methods to the analysis of species identity and concentration in high pressure sources. Bray's [14] one-dimensional sudden freezing model of chemically reacting expanding gases, where the reaction is at equilibrium upstream and frozen downstream provides a reasonable approximation to finite rate non-equilibrium systems. This model is also supported by the experimental results of Wegener [15] who used a low expansion ratio[5] one-dimensional nozzle system. The reaction studied

$$N_2 + N_2O_4 \rightleftarrows N_2 + 2NO_2$$
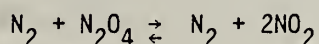
is quite fast, with a half life of $\sim 10^{-7}$s [15]. In spite of the fact that the expansion time for Wegener's nozzle was about 3×10^3s, i.e., relatively long, he observed major departures from the expansion flow equilibrium--expected for an infinitely fast relaxation rate. Hence, even for reactions of the order of 10^4 times faster than the expansion process, much of the chemical information may be frozen with respect to the source composition--which is the desired condition for high pressure sampling.

---

[5]Number density ratio for pre and post expansion regimes (see Section 3.2.2).

A more critical test for chemical relaxation effects is given by the very fast ion-molecule reactions studied by Hayhurst and Telford [16]. Their nozzle system geometry is similar to ours. Using a 1 atm flame source they monitored the reaction

$$H_3O^+ + H_2O + M \rightleftarrows H_5O_2^+ + M$$
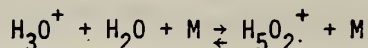
which has an estimated forward rate relaxation time of 2×10^{-9}s. The concentration ratio $[H_5O_2^+]/[H_3O^+]$ observed was much higher than the equilibrium concentration expected in the sampled flame. Using a three-dimensional method-of-characteristics solution to the expansion flow field, they obtained results which were in good agreement with one dimensional solutions. Although they found significant evidence for boundary layer perturbations, caused by the water cooled nozzle, they concluded that flow equilibrium had prevailed during the early phase of expansion. They also suggested as a general criterion for ideal unperturbed sampling that the reactions of interest have a relaxation time significantly longer than continuum flow time.

For normal gas-gas and condensed-gas reactions involving uncharged species, reaction times are typically greater than 10^{-5}s. As continuum flow times of 10^{-7}s are typical for modern sampling systems, including ours, the criterion for minimal sampling perturbation should apply for most molecular systems of interest. In the absence of chemical reaction kinetic data, however, it is desirable to provide experimental verification of sampling fidelity. This has been done for the TMS system, as described in Section 4.

3.2 Beam flux and sensitivity--conical probes
3.2.1 Beam flux-source pressure dependence

Greene, et al. [17] showed that the flux through the skimmer of an isentropically expanding gas from a supersonic nozzle (i.e., conical probe) has the functional form of effusive flow multiplied by a function dependent only on the gas specific heat and the Mach number at the skimmer. Experimentally it has also been shown [18] that, to a good approximation, the dilute components of a gas mixture undergoing supersonic expansion are accelerated with the characteristics of the solvent carrier gas. In the absence of mass separation effects (see Section 3.3) these results suggest that the usual mass spectrometer relationship, based on effusive flow, can be applied to the supersonic jet sampling process. That is,

$$P_o = kIT_o$$

where I is the observed ion intensity,
T_o the source temperature,
k the effective mass spectrometer sensitivity constant, and
P_o the source pressure.

As will be shown by our data, the functional dependence of beam flux on specific heat and Mach number can be empirically absorbed into the k factor when this "constant" is obtained from the observed ion intensity for the carrier gas at known conditions of P_0 and T_0. In practice, k is measured at every temperature and pressure of an experimental run. The k's obtained show a minor variation with temperature and pressure, reflecting small changes in the expansion process including mass separation effects.

3.2.2 Nozzle characteristics

The size of main chamber tube (see fig. 2) and sample which could be accommodated in the current vacuum system design, and the need to assure saturation of the carrier gas, determined the transpiration gas flow range (less than 40 sccm). In the physical design of the sampling system, available pumping speed and desired expansion ratio governed the choice of nozzle orifice size. Experimentally, it was determined for the chosen nozzle geometry and available pumping speed, that an orifice diameter of 0.008 cm, required a nitrogen carrier gas flow rate of <10 sccm to maintain a stage I pressure of ~5x10^{-7} atm.

The Knudsen number (Kn_0) can be determined from its definition,

$$Kn_0 = \frac{\lambda_0}{d_0}$$

where $\lambda_0 = [(2)^{1/2} \pi \sigma^2 n_0]^{-1}$ = mean free path,

d_0 is the nozzle orifice diameter,

σ is the collision diameter, and

n_0 is the carrier gas number density.

Using $\sigma \sim 3.7 \times 10^8$ cm [19], Kn_0 for this system is 0.003 at 1 atm and 1000 K. This value is well within the limit for continuum flow which is generally taken as $Kn_0 \leq 0.1$. To insure that the sample beam represents the bulk source gas and not a stagnant boundary layer near the orifice, the Knudsen number should be small enough that boundary layer effects can be ignored. For $Kn_0 \leq 0.01$ these effects are minimal [20]. In the present system, where the nozzle is maintained at T_0, this Knudsen number constraint is probably of lesser importance than the continuum flow requirement.

Pumping speed in the nozzle-skimmer region can be calculated from

$$F_0 = n_I S_I$$

where F_0 is the net flow rate in molecules/s from the source,

n_I is the stage I number density in molecules/cm^3, and

S_I is the pumping speed in cm^3/s.

For the above conditions, the pumping speed in the nozzle region is calculated as ~330 L/s. Conductance estimates, based on the stage I geometry, indicated the net pumping speed in the nozzle region should be ~300-400 L/s in good agreement with the above flow rate determination.

The nozzle expansion ratio for the sonic conical nozzle can be given by the ratio of source number density to stage I number density, i.e.,

$$\frac{n_0}{n_I} = \left(\frac{P_0 \cdot 298}{P_I \cdot T_0}\right) \sim 5 \times 10^5 \quad ,$$

at typical conditions of P_0 = 0.8 atm and T_0 = 1000 K. This ratio is essentially constant as long as S_I and the nozzle-skimmer geometry are fixed. It was not feasible to construct a real-time variable distance nozzle-skimmer system for the following reason. The high flux of condensibles from the transpiration zone at high temperatures precluded the more conventional use of a room temperature or cooled skimmer [21] since plugging of the skimmer orifice would be quite rapid (see Section 2.1). This problem was avoided by mounting the skimmer directly onto the heated nozzle, just outside the furnace zone. The high available pumping speed of 800 L/s in stage I, outside the nozzle-skimmer region, produces an operating mean free path of ~15 cm. A simple plate, with an orifice for line of sight transmission (see fig. 1, region I) allows the skimmer itself to behave as a differential pumping barrier with the stage I pump performing double duty. The disadvantage of a higher post-skimmer pressure is more than offset by the system simplification provided, and since the skimmer orifice would be located about 4 cm from the differential pump aperture, this nozzle-skimmer arrangement seemed to be a reasonable compromise.

3.2.3 Skimmer characteristics

Location of the skimmer should be well upstream of the Mach disc to avoid beam scattering through a detached shock. Ashkenas and Sherman [9] have experimentally confirmed the relation determining the Mach disc location, in nozzle diameters, as

$$\frac{Z}{d_0} = 0.67 \left(\frac{P_0}{P_I}\right)^{1/2}$$

for distance Z from the nozzle orifice, at room temperature expansion ratios to ~17,000 and $T_0 = T_I$. This expression places the Mach disc in our system at ~475 nozzle diameters or ~4 cm from the nozzle. Greene, et al. [17] have successfully utilized a system with similar nozzle size, geometry, and expansion ratio parameters. Their determination of beam intensity dependence on nozzle to skimmer distance indicated a maximum intensity at 120 nozzle diameters for 1 atm pressure. At smaller Z/d_0 the intensity dropped sharply but at greater distances the decline was gradual. In order to avoid rapid changes in instrument sensitivity with pressure, the skimmer-nozzle spacing was somewhat larger than for the maximum intensity condition, i.e., 1.1 cm (Z/d_0 ~140). An estimated 30 percent of the maximum beam intensity was sacrificed with this arrangement. This spacing also placed us well within the expected Mach disc location, thus providing a safety margin against a possible over-estimate of the expansion ratio. It is also desirable to locate the skimmer downstream of the "freeze-in" point,

where essentially collisionless flow begins, to minimize shock induced scattering in the downstream regions of the skimmer.

Anderson and Fenn [8] have developed an expression for estimating the location at which the terminal Mach number occurs. At this location the Mach number has a maximum rate of change and the collision dominated region of the expansion ends. Stearns, et al. [20] have calculated, using the derivations of Anderson and Fenn [8], expressions for the terminal Mach number for typical ratios of the gas heat capacity γ,

$$M_t \ (\gamma=5/3) = 2.03 \left(\frac{Kn_0}{\varepsilon}\right)^{-0.400}$$

$$M_t \ (\gamma=7/5) = 2.48 \left(\frac{Kn_0}{\varepsilon}\right)^{-0.286}$$

$$M_t \ (\gamma=9/7) = 2.85 \left(\frac{Kn_0}{\varepsilon}\right)^{-0.222}$$

where ε is a collision effectiveness parameter, measured by Anderson and Fenn [8] for monatomic gases to be ~0.25. This terminal Mach number can be applied in the general semi-empirical expression for center-line Mach number

$$M = A(\gamma) \ \left(\frac{Z}{d_0}\right)^{\gamma-1}, \ (M>4)$$

where $A(\gamma)$ is 3.26 for $\gamma=5/3$, 3.65 for $\gamma=7/5$, and 3.96 for $\gamma=9/7$. Using the $\gamma=7/5$ expression for our nozzle, a value of M_t ~10.7 is calculated. Z_t/d_0 is then about 15. Thus our choice of Z/d_0 ~140 is well downstream of the point of translational freezing.

Using the sudden-freeze approximation of Stearns, et al. [20], the number density at the end of the isentropic expansion process can be calculated from

$$n_t = n_0 \ [1 + \frac{(\gamma-1)}{2} \ M_t^2](1-\gamma)^{-1}$$

which for typical conditions (n_0 = 2.2 x 10^{19} molecules/cm^3) in our system gives n_t ~3.6x10^{15} molecules/cm^3. The number density (n_s) at the skimmer is derived from molecular flow considerations as,

$$n_s = n_t \left(\frac{Z_t}{Z_s}\right)^2$$

giving n_s ~4x10^{13} molecules/cm^3. With a skimmer orifice size of 0.08 cm, the skimmer Knudsen number is ~56, indicating that flow into the skimmer is well into the effusive range.

The choice of skimmer aperture size was based on an expected core beam with a half angle spread of ~4°. Since the skimmer could not be readily adjusted during an experiment, additional beam attenuation due to downstream scattering for this relatively large skimmer

orifice would be a lesser problem than loss of the beam due to shifting of the skimmer during thermal cycling. This has proved to be the case since we routinely monitor the low abundance isotopes ^{36}Ar and $^{14}N^{15}N$ which are 0.3 and 0.7 percent of the carrier gases, respectively, and find these signals to be 3 or 4 orders of magnitude above the minimum detectable signal for high background regions of the spectrum. That is, minimum sensitivity is about 1 ppm.

3.3 Capillary probe sampling

For the converging nozzle geometry of our capillary, two descriptions of the flow conditions can be used. The standard isentropic relations, assuming adiabatic conditions, yield expressions identical to those for the sonic nozzle, since the isentropic solution is independent of channel length when the exit pressure is lower than the critical pressure, P_c[6]. For this case, the pressure drop across the capillary channel is given by,

$$\frac{P_c}{P_o} = (\frac{2}{\gamma+1})^{\gamma/(\gamma-1)}$$

and the exit velocity is sonic, i.e., the Mach number is 1. A simple graphical treatment of the velocity function along the capillary suggested that in the early phases of expansion, the isentropic temperature drop might occur in a time scale where vibrational relaxation could play a role. This could manifest itself, for example, as an apparent temperature error - in Clausius-Clapeyron plots of pressure versus temperature data.

Another possible treatment is to consider that for a narrow channel wall collisions should be important. Thus, energy transfer should occur and since the capillary is essentially at T_o, the flow description should be isothermal. The solution for the isothermal case is a straightforward problem, very similar to the isentropic case, and yields a pressure drop along the nozzle channel of,

$$\frac{P_c}{P_o} = e^{-1.2} = 0.606.$$

The flow velocity yields an exit Mach number of $M\gamma^{-1/2}$. These conditions are very similar to the isentropic case and thus one would expect expansion in the stage I vacuum chamber to be indistinguishable from isentropic expansion within the channel. In practice both the conical and capillary samplers showed similar, though not identical, gas dynamic character.

---

[6]This critical pressure in the minimum pressure which can exist within the channel for a given initial pressure at the channel entrance.

3.4 System mass discrimination
3.4.1 Contributing factors

In order to make quantitative measurements of species partial pressures, it was necessary to determine the magnitude of possible mass discrimination effects in our system. One such effect is inherent in the free-jet expansion process and results from differences in the perpendicular velocity component for various beam species, leading to radial diffusion and depletion of low mass species in the beam. In practice, this effect is superimposed on the normal mass discrimination effects of the quadrupole mass analyzer and electron multiplier.

The radial diffusion effect, often referred to as "Mach number focusing," has been explained by Stern, et al. [22] as follows. As the expansion progresses, the translational temperature falls and random velocities in the beam decrease. However, lighter gases near the axis (and elsewhere) will have a higher net velocity and thus a larger perpendicular velocity component with respect to the beam axis. Qualitatively, then, one would expect to observe in the regions where the flow is collision dominated, a depletion in the beam of the lighter mass species. Past the collision dominated region, reverse diffusion would be expected to gradually reduce this process.

Reis and Fenn [23] observed mass separation effects in nitrogen-hydrogen mixtures which could be attributed to formation of a detached shock. A theoretical analysis by Sherman [24] indicated agreement with the results of Reis and Fenn [23] where the bow shock was swallowed (by the skimmer); but where a detached shock was formed, a much higher separation of light and heavy species was predicted. He concluded that large separation effects result from a probe perturbation and vary proportionally to the inverse of the Reynolds number.

A first power dependence of mass separation with molecular weight was observed by Green, et al. [17] which suggested that the lesser dependence observed by Stern, et al. [22] may be due to skimming downstream of the Mach disc location. However, this is not the case in the work of Reis and Fenn [23], and the large separations observed by Greene, et al. [17] might have a similar explanation, even though the conditions are quite different. Greene, et al. [17] used rather small pumps and the skimmer region pressures were such that the mean free path was of the order of 0.5 cm. A calculated Reynolds number at their skimmer, based on their reported background gas pressure, is ~0.08. Even though collisional interaction in their beam presumably ceased well upstream of the skimmer, shock production and detachment at the skimmer were still possible, and the above arguments could then apply at least qualitatively.

3.4.2 Experimental observations

In combination, the various mass discrimination effects are taken into account by calibration with a commercially prepared (Matheson) standard gas mixture analyzed (Matheson) against gravimetric standards. This gas mixture contains ~1 percent of each of the rare gases, helium, neon, argon, krypton, and xenon in nitrogen and has been analyzed to 0.01 percent of the gas composition. The overall mass discrimination function, as obtained in the temperature and pressure region of operation and normalized to the carrier gas (N_2), is used

to correct the ion intensity and, hence, pressure data (see Section 4.2). Table 1 gives the gas mixture analysis (as supplied by Matheson). This analysis was independently confirmed by us using GC analysis.

Table 1. Calibration gas mixture characteristics.

Gas	Fraction of mix[a]	Ionization cross section[b]	Isotope mass (amu)	Isotope abundance
N_2	0.9489	1.18 ± 0.1	28	0.9892
			29	0.0072
He	0.0102	0.08 ± 0.03	4	1.00
Ne	0.0100	0.11 ± 0.03	20	0.905
			22	0.092
Ar	0.0104	2.6 ± 0.3	36	0.0034
			40	0.9959
Kr	0.0104	3.8 ± 0.6	84	0.570
			86	0.173
Xe	0.0105	6.2 ± 2	129	0.264
			132	0.270
			134	0.105

[a]Gas chromatographic analysis (Matheson) calibrated against gravimetric standards.

[b]Kieffer and Dunn [39]; σ taken from their graphs at 30 eV, errors estimated from their data spread.

A typical plot of normalized ion intensities versus mass number, at several temperatures and pressures, is given in figure 6. The normalization of ion intensities, I_m, for species m, to the nitrogen carrier gas (using the $^{29}N_2$ isotopic species) is made using the expression

$$I_m(\text{norm}) = \frac{I_m}{f_m \cdot A_m \cdot \sigma_m} \frac{f_{29} \cdot A_{29} \cdot \sigma_{29}}{I_{29}} \quad ,$$

where f_m is the mole fraction,
    A_m the isotopic abundance, and
    σ_m the ionization cross section at 30 eV (see table 1).
The mass spectrometer resolution used was sufficient to separate (>10% valley) each xenon isotope. It should be noted that the ^{36}Ar isotope concentration in the mixture is only

34 ppm. This mass peak is relatively noisy due to background argon and other unidentified residual gas components. However, with reasonable integration times (4 s), a signal-to-noise ratio significantly better than 10 could be obtained, indicating a conservative detection limit of <10 ppm. The reference discrimination curve (see effusive curve of fig. 6) was obtained under effusive conditions at a pressure of less than 10^{-5} atm using a large orifice cell. This curve may be used as a measure of the mass discrimination effects present in the quadrupole filter and detector.
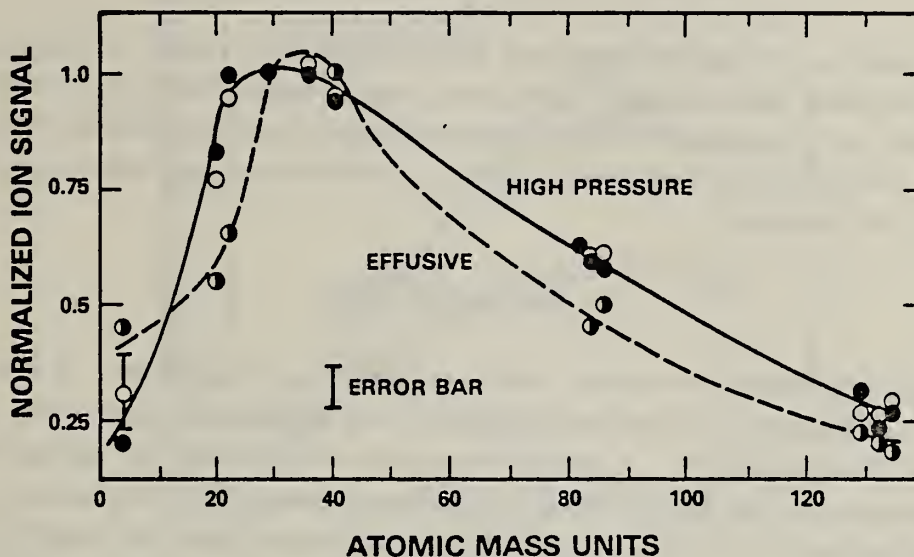
Figure 6. Mass discrimination behavior obtained using a standard gas mixture of: He(1.02%), Ne(1.00), Ar(1.04), Kr(1.04), Xe(1.05), and N_2(94.85): open circles – conical sonic orifice sampler at 1065 K and 0.6 atm, closed circles – capillary sampler at 800 K and 0.3 atm, and half closed circles – effusive source at 295 K and $<10^{-5}$ atm. Error bar represents worst case for variations in ion signal; most abundant isotope of each species normally exhibits variations less than half this amount. An exception is ^{20}Ne, where contributions from ^{40}Ar^{2+} and the narrow peak width limit the signal to noise ratio. Ion intensities measured at 30 eV ionizing electron energy and normalized with respect to $^{29}N_2{}^+$.

Figure 6 shows a small enhancement (∼10%) of higher mass species in supersonic beams which agrees qualitatively with the arguments outlined in Section 3.4.1, considering an early onset of collisional "freezing" and the relatively large skimmer-orifice separation used. The rapid signal fall-off at He is mainly a mass spectrometer resolution effect. Instrument tuning conditions produce very narrow peaks below 12 amu and consequent difficulties in

dwelling on the peak maximum. The effective coincidence of the mass separation curves for the conical and capillary probes (see fig. 6) suggests that both probe types are effectively isentropic in their expansion characteristics.

To account for the combined mass discrimination effects of mass separation in the expanding jet and quadrupole mass filter discrimination, a sensitivity factor, $S_{Na^+(NaCl)}$, for example, was obtained from

$$S_{Na^+(NaCl)} = \left(\frac{S_h - S_e}{S_e}\right)_{58\ amu} + (S_e)_{23\ amu}$$

where h and e refer to the high pressure and effusion curves of figure 6, respectively.

It should be noted that the experimental mass discrimination function is essentially fixed for a given set of quadrupole mass filter operating parameters. However, when the mass spectrometer is re-tuned by varying the ion source and resolution settings a new discrimination function is obtained.

3.5 Aggregation effects

Besides mass discrimination effects, other perturbations are possible in supersonic free jet expansion. Condensation or species aggregation is a particularly well known case, e.g., see [10,25] and cited references. A particularly useful test of species aggregation is to monitor the formation of Ar_2 in the expansion process. However, the single pump differential pumping scheme employed by us in the nozzle-skimmer region did not allow operation in a low scattering condition at pressures where the Ar_2^+ intensity would be above our detection limit. Bier and Hagena [10] give limiting criteria for minimizing condensation, based on the source pressure-nozzle diameter product $P_o \cdot d_o$. At a source temperature of 295 K, $P_o \cdot d_o$ should be less than 60 Torr-mm for CO_2, 85 Torr-mm for argon, and 500 Torr-mm for nitrogen. At atmospheric pressure and room temperature our system operates at $P_o \cdot d_o < 60$ Torr-mm and, consequently, condensation should be minimal or non-existant, particularly at higher temperatures.

3.6 Pressure operating characteristics

Figure 7 shows the behavior of the detected ion signal as a function of source pressure. For this instrument, the expansion ratio is essentially constant, set by the available pumping speed, and the turnover of the unit slope portion of the curves, marked by arrows on figure 7, occurs consistently at an observed pressure of $P_I \sim 2 \times 10^{-6}$ atm. The fact that this turnover occurs for both the capillary (no skimmer) and conical sampling system at the same stage I pressure, independent of temperature, suggests the effect is a post-expansion scattering phenomenon dependent primarily on the mean free path. This argument is also consistent with the sensitivity of the turnover point onset to the skimmer alinement relative to the nozzle.

It appears possible, as Green, et al. [17] showed, to operate at pressures where scattering is significant and still maintain sampling fidelity; our data also indicate this (see Sections 4 and 5). However, the majority of our experimental runs were made in a pressure

range where scattering was relatively low, i.e., within the linear region of the intensity-pressure curves such as those shown in figure 7.
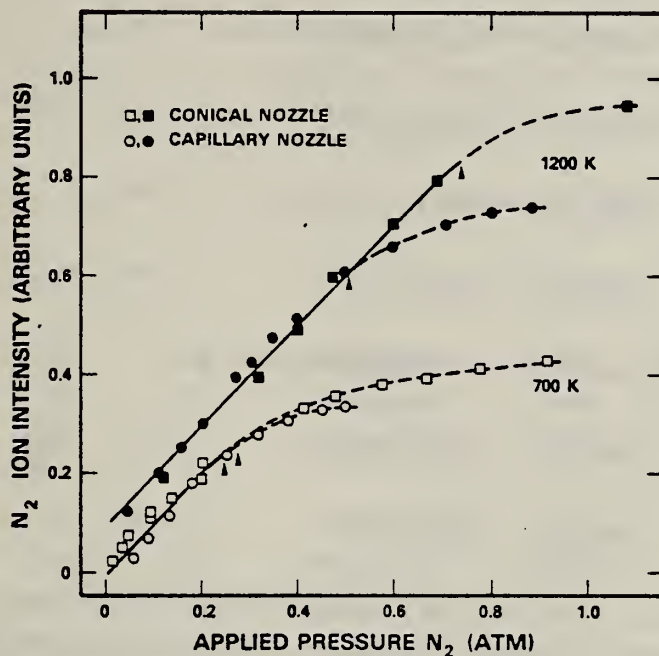
Figure 7. Dependence of carrier gas ion intensity on applied pressure and temperature. The 1200 K data have been offset vertically +0.1 div for clarity. Solid curves are lines of unit slope and zero intercept in accord with the theoretical relationship. Arrows indicate where stage I pressure exceeds 2×10^{-6} atm. The capillary curve deviates from linearity at lower pressure because the total flow rate is higher through the relatively large capillary orifice.

4. The NaCl System: Results and Discussion

This system was chosen to test the validity and accuracy of the transpiration mass spectrometric technique, since the literature data for NaCl is extensive, reasonably self-consistent, and has been critically evaluated and formatted as thermochemical tables by JANAF [26].

Between about 800-1600 K the significant reactions in the equilibrium NaCl vaporization process are

$$NaCl(s) = NaCl(g) \qquad\qquad R1$$

$$NaCl(l) = NaCl(g) \qquad\qquad R2$$

$$2NaCl(s) = (NaCl)_2 \, (g) \qquad R3$$

$$2NaCl(l) = (NaCl)_2 \, (g) \qquad R4$$

$$3NaCl(s) = (NaCl)_3 \, (g) \qquad R5$$

$$3NaCl(l) = (NaCl)_3 \, (g). \qquad R6$$
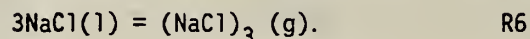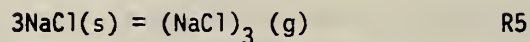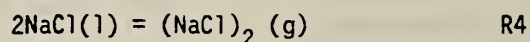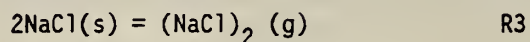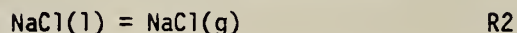
Reactions R1 - R4 can be expressed in homogeneous form as

$$2NaCl(g) = (NaCl)_2 \, (g), \qquad R7$$

and similarly

$$3NaCl(g) = (NaCl)_3 \, (g). \qquad R8$$
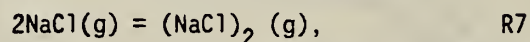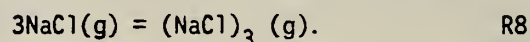
This variety of reactions, involving both homogeneous and heterogeneous equilibria should provide a stringent test of the TMS technique, and particularly where the second law method of data analysis is used.

Barton and Bloom [27] measured the total pressure of NaCl(l) by a boiling point method and reported excellent agreement with the results of earlier workers. Vaporization of NaCl(s) from a copper Knudsen cell was reported by Miller and Kusch [28] who used a velocity profile analysis on effusive vaporization and determined the presence of substantial amounts of dimer $(NaCl)_2(g)$. More recently, Milne and Klein [29] measured heats of sublimation and dimerization for the alkali chlorides, including NaCl, using the mass spectrometric Knudsen effusion method. By incorporating selected literature data with their results they were able to make an extrapolation to the liquidus region. Second law heats of vaporization for the monomer (reaction R2) differ between laboratories by no more than 3.5 k cal/mol. This uncertainty is sufficiently low that the reaction may be used to test the temperature dependent character- istics of the transpiration reactor sampling system.

Certified reagent grade (A.C.S.) sodium chloride (Fisher lot number 757984) was used without further treatment. Lot analysis indicated contaminants of less than 0.1 percent and no impurity ion signals were observed in the mass spectra.

4.1 NaCl mass spectral fragmentation data

The characteristic mass spectral fragmentation pattern for NaCl vapor has been reasonably well established by others using Knudsen effusion mass spectrometry [29,30] over solid

samples. A potential problem with this system arises from the presence of both NaCl and $(NaCl)_2$ in the vapor, where either of these species could be a precursor for the ions Na^+ and $NaCl^+$. Feather and Searcy [31] have considered the possible contribution to $NaCl^+$ from $(NaCl)_2$. They showed that if one assumes the dimer as the $NaCl^+$ progenitor, a 35 percent change in the ratio $R = Na^+/NaCl^+$ should result over the temperature range 870 to 1020 K. However, within a 15 percent uncertainty, they observed no temperature dependence in the observed R value of about two. Our Knudsen effusion data (see Section 4.5) support this observation; R values of about 1.5 were practically invariant over the same temperature range (see fig. 10, in Section 4.5). Hence, $NaCl^+$ can be used as a measure of the monomer partial pressure[7]. Typical mass spectral fragmentation data are summarized in table 2.

Table 2. Typical mass spectral ion intensities[a] for the NaCl system.

Na^+	$NaCl^+$	Na_2Cl^+	R^b	Cell	T(K)	eV	Source
1.00	0.49	0.88	2.0	Cu-Knudsen	968	70	[31]
1.00	0.73	0.91	1.4	Cu-Knudsen	~960	20	[29]
1.00^c	0.66	0.66	1.5	Pt-Knudsen	957	30	Section 4.4
1.00^d	0.04	0.08	25.0	Pt-transp.^{e}	1312	30	Section 4.3
1.00^g	0.03	0.14	33.3	Pt-transp.^{f}	1360	30	

[a] Normalized to $I_{Na}+$, and corrected for Cl-isotope fractions.

[b] $R = I_{Na}+/I_{NaCl}+$.

[c] Equivalent to a signal intensity of 920 $\mu V (10^7 \Omega)$.

[d] Equivalent to a signal intensity of 1.8×10^4 μV.

[e] Carrier gas N_2 at 0.54 atm; $I_{29_{N_2}} = 1.00$ $(=1.8 \times 10^4$ $\mu V)$ and $k_{N_2} = 1.66 \times 10^{-10}$ $\mu V/atm$ K.

[f] Transpiration weight loss run. Note S factors differ to e. $k_{N_2} = 3.7 \times 10^{-11}$ $\mu V/atm$ K (0.65 atm).

[g] Equivalent to a signal intensity of 1.9×10^4 μV.

The transpiration mass spectrometric data for the vapors over solid NaCl (i.e., at temperatures more compatible with Knudsen effusion data) showed no measurable $NaCl^+$ ion. However, while the 23 amu Na^+ ion is at a low noise position, $NaCl^+$ at 58 and 60 amu is relatively noisy (an order of magnitude greater than for 23 amu) and R values of about 2 cannot be ruled out on this basis. But, well into the liquid range, where the ion signals at both 23 and 58 amu are strong and relatively noise-free, we observe R ~26 ± 4[8]. This ratio

[7] Recent angular distribution mass spectrometric measurements (~10-70 eV) also indicate NaCl as the predominant (>99 %) precursor for Na^+ and $NaCl^+$, as well as $(NaCl)_2$ for Na_2Cl^+. (R. Grimley, Purdue Univ., personal communication (Nov. 1978)).

[8] Error is standard deviation for data above 1170 K.

varies slightly between experimental runs. The average ratio above 1200 K is quite constant within a variable temperature run and shows no significant variation from ~1200 - 1500 K, even with carrier gas pressures varying over the range 0.35-0.8 atm.

That the relatively high Na^+ signal intensities are not an artifact of the external geometry of the sampling system, such as NaCl-furnace interaction, is evidenced from the following observations. If the furnace power is suddenly turned off, the transpiration sampler cools much more slowly than the furnace and the Na^+, $NaCl^+$ and Na_2Cl^+ signals respond to the sampler temperature, not the furnace, thus precluding a decomposition mechanism involving the hotter furnace. Salt does not deposit on the exterior of the sampler elements since, with the sampler cool, a sudden heating of the furnace does not produce significant signals of sodium-containing species until the lagging sampler has reached an internal temperature where these species are normally observed. As a final test of the absence of external deposits, the sampler can be cycled down in temperature, the sample boat and boat-carrier removed, and the sampler immediately returned to a high temperature. The small amount of residual salt in the sampler produces ion signals of less than 4 percent of those obtained at the same temperature with a normal sample level present, and the ion signal decays rapidly to barely detectable levels.

Ion intensity ratios can also depend on mass discrimination differences between individual species, as was discussed in Section 3.4. However, for the ions in question the mass discrimination curves of figure 6 indicate only small differences between the 23 and 58 amu species.

It appears, then, that the high $Na^+/NaCl^+$ ion intensity ratio, with respect to those characteristic of Knudsen effusion measurements, are not an artifact of the sampling process. The remaining explanation must be associated with the electron impact ionization process and the non-thermal nature of the molecular beam. A possible pertinent observation in this regard was made by Berkowitz, et al. [32] for the related case of LiF, using Knudsen effusion mass spectrometry, where a factor of three decrease in Li^+/LiF^+ was observed for a 300 K temperature increase. It was suggested that the tendency for LiF to yield Li^+ in a state of excess energy increased with temperature and that the ion source discriminated against these excess energy ions thereby yielding lower Li^+/LiF^+ ratios at higher temperatures. In sharp contrast to effusive beams, the supersonic beam used for our TMS studies had an effective temperature of the order of 10 percent of the transpiration source temperature. We speculate that this large difference in temperature between effusive and supersonic beams might well produce a similar ion source discrimination effect for NaCl. That is, the effectively much cooler (translationally and probably vibrationally) NaCl species produced by high pressure sampling would ionize to form Na^+ with relatively less excess energy, and the ion source would produce higher relative amounts (with respect to $NaCl^+$ and Na_2Cl^+) of Na^+ for mass analysis and detection, leading to high R values. On the other hand, the effusive molecular beams obtained using Knudsen cells remain at high temperature during passage to the ionizer and low R values would result from the effect of excess energy discrimination. That R is essentially temperature independent for a TMS experiment may be explained from the known

properties of supersonic beams where the final beam temperature does not vary to nearly the same degree as the source temperature.

This explanation of apparently anomalous mass spectral fragmentation warrants further investigation with the TMS technique, possibly including other alkali halide species such as LiF. However, as will become evident from the discussion to follow, a definitive explanation of the apparent high R values obtained by TMS is not necessary to successful application of the technique to thermodynamic studies.

4.2 NaCl vaporization and pressure calibration

The effective temperature insensitivity of the $Na^+/NaCl^+$ ratio, R, together with auxiliary appearance potential data (not presented here as it basically agrees with earlier work), leads to the conclusion that both Na^+ and $NaCl^+$ may be used as a measure of the NaCl partial pressure without significant interference from electron impact fragmentation of the $(NaCl)_2$ dimer species[9]. Typical partial pressure data for NaCl derived on this basis are shown in figure 8. This plot represents a number of sets of data obtained using either Ar or N_2 as carrier gases, with total pressures varying from 0.35-0.75 atm and 0.4-0.8 atm, respectively. Two different conical orifice samplers of similar, but not identical, construction were used. Also, the data plotted in the liquid range include pressures calculated from both Na^+ and $NaCl^+$ ion intensities. The essential concordance between these various data sets support the ion-precursor assignments and all other aspects of the procedure adopted for converting ion intensities to partial pressures. Note also in figure 8 the good agreement between the experimental and literature melting points (T_m), indicative of accurate temperature measurement.

4.2.1 Partial pressure-ion intensity relationships

There are three methods by which the mass spectral ion intensity data were converted to absolute pressures in the present study:
  (a) classical transpiration,
  (b) integrated ion intensity-time method, and
  (c) reference gas ion intensity comparison.

With method (a) the salt mass loss is measured (gravimetrically) for a known volume of transpiration carrier gas at a fixed temperature and total pressure. Typical data are given in table 3. To convert these data to a partial pressure for the NaCl species, a small correction was made for the dimer species $(NaCl)_2$ using the JANAF [26] thermochemical data. Subsequent analysis of our own data for the dimer-monomer equilibrium reaction (Section 4.5) will indicate that this dimer correction may be too high but is still within the quoted uncertainty for P_{NaCl} given in table 3.

---

[9]The similar T dependence of Na^+ and $NaCl^+$, but not Na_2Cl^+, shown in figure 10 (Section 4.5) also supports this claim, as do similar data reported in the literature.
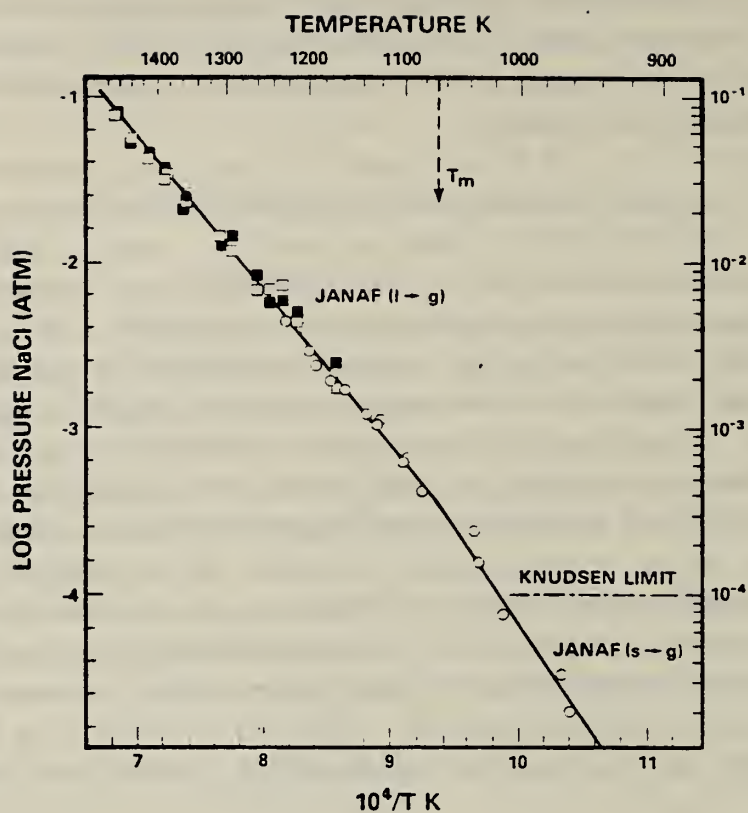
Figure 8. Vapor pressure curves for NaCl (s and l) obtained by TMS.
Open squares - $P_{NaCl}(Na^+)$ in N_2 carrier gas, total pressure 0.4-0.8 atm,
at 30 eV. Closed squares - $P_{NaCl}(NaCl^+)$ in N_2 carrier gas total
pressure 0.4-0.8 atm, at 30 eV. Open circles - $P_{NaCl}(Na^+)$ in Ar
carrier gas, total pressure 0.35-0.75 atm, at 70 eV. The data points
Δ and ● were obtained using the integrated ion intensity (b) and clas-
sical transpiration (a) methods, respectively (see Section 4.2.1). All
other points were obtained using the ion intensity comparison method (c).
Solid curve represents data from the JANAF compilation [26]. The broken
line labeled Knudsen limit was calculated assuming a typical orifice
diameter of 0.1 cm.

Method (b) is an adaptation of the integrated ion intensity method often used with Knudsen
effusion cells as described in Section 4.4. In the present case use is made of equation 4.1
and the relationship

$$k_{NaCl} = R(\frac{n}{V})\Delta t/\Sigma I\Delta t$$

384

where R is the Universal gas constant, n the number of moles of salt transported as NaCl species, and V the volume of carrier gas transported for time t and constant temperature T.

Table 3. NaCl Absolute Pressure Calibration

transpiration mass loss data:

time 172 min
N_2 flow rate 7.9 sccm
T = 1360 K
N_2 pressure 0.7 atm
NaCl mass loss 0.193 gm

auxiliary input data:

average mol wt 72^a

$$P_{Na_2Cl_2}/\left(P_{Na_2Cl_2} + P_{NaCl}\right) = 0.23^a$$

derived pressures:[b]

$$P_{NaCl_{total}} = [n_{NaCl}/(n_{NaCl} + n_{N_2})]P_{total} = 2.96 \ (\pm 0.6) \times 10^{-2} \ atm$$

$$P_{NaCl} = 2.28 \ (\pm 0.4) \times 10^{-2} \ atm$$

---

[a] Derived from JANAF [26] data and also self consistent with independent Knudsen and TMS data from the present study.
[b] n refers to moles of gas transported.

Method (c) utilizes the known pressure and ion intensity of the carrier gas (Ar or N_2), but relative mass discrimination factors and ionization cross sections are needed. For the relatively straightforward case of Na^+ as a measure of NaCl, ion intensities were converted to partial pressures as follows. The partial pressure of NaCl is given by,

$$P_{NaCl}(Na^+) = k_{NaCl} \cdot I_{Na^+} \cdot T \ , \qquad (4.1)$$

where k_{NaCl} is a constant which takes into account mass spectrometer sensitivity (k'), mass discrimination (S) and ionization cross section (σ) effects; I_{Na^+} is the measured Na^+ ion intensity at the sample temperature, T. The constant k_{NaCl} can be derived from a knowledge of the carrier gas pressure and ion intensity, i.e.,

$$P_{Ar} = k_{Ar} \cdot I_{Ar^+} \cdot T \ , \qquad (4.2)$$

and

$$k_{Ar} = P_{Ar} / \left(I_{Ar}{}^{+} \cdot T \right) \qquad (4.3)$$

then

$$k_{NaCl} = k_{Ar} \left(\frac{\sigma_{Ar}}{\sigma_{NaCl}} \right) \left(\frac{S_{Ar}}{S_{NaCl}} \right) \left(\bar{S} \right)^{-1} . \qquad (4.4)$$

The term $\bar{S}$ (≤ 1) is an empirical correction factor discussed in Section 4.2.3.

For the case of $NaCl^{+}$ as a measure of NaCl, an average R value, denoted as $\bar{R}$, was used as a scaling factor (necessary for the total ionization cross section argument to be valid) to avoid overwhelming the $NaCl^{+}$ variations by the large Na^{+} contribution. The $P_{NaCl}(NaCl^{+})$ data were obtained from the expression

$$P_{NaCl}(NaCl^{+}) = [(1 + \bar{R}) \cdot \dot{I}_{NaCl}{}^{+}] k_{NaCl} \cdot T . \qquad (4.5)$$

Figure 8 shows the pressures derived from this expression to be equivalent to those using the Na^{+} ion intensity data [and eq. (4.1)].

4.2.2 Ionization cross sections

Values of σ for the reference gases N_2 and Ar are known from the literature [39]. However, no such data exist for the high temperature species NaCl and $(NaCl)_2$. Expressions of the type 4.4 can be used to obtain ratios of ionization cross sections. Values of σ, relative to Ar, were measured for N_2, O_2, SO_2 and NaCl using the TMS technique and the results are summarized in table 4. The data for N_2 and O_2 agree with the literature results within the combined experimental errors. Also the measured σ's for SO_2 and NaCl seem reasonable in comparison with data for electronically similar species. To derive σ_{NaCl}, k_{NaCl} was obtained using expression 4.1 and the value of P_{NaCl} obtained by transpiration [method (a)].

Table 4. Ionization Cross Sections (πa_0^2 units [39])[a]

	30 eV		70 eV	
Ar	--	(2.6)[b]	--	(4.0)
N_2	1.48	(1.2)	3.0	(2.8)
O_2	1.26	(1.0)	2.8	(2.8)
SO_2	1.3		--	
Na	--	(4.6 ± 0.3)	--	(4.0 ± 0.2)
NaCl	1.00	(± 0.3)[c]	--	
$(NaCl)_2$	1.5[d]		--	

[a]Experimental values determined from expressions of the type 4.4 using Ar as reference σ_j.
[b]Literature values of Kieffer and Dunn [39] given in parentheses. Typical uncertainty ± 0.2.
[c]Based on $\bar{S}$ = 0.6, as determined in Section 5.2.
[d]Determined from literature empiricism for dimer to monomer cross section ratio of ~1.5
(Meyer and Lynch [40]); probable uncertainty ± 0.2.

4.2.3 Pressure correction due to gas scattering

The empirical factor $\bar{S}$ contained in expression 4.4 corrects for a differential gas scattering effect. This effect, which is characteristic of our TMS system, arises as follows.

In the working pressure range of our system, the beam number density at the skimmer is only four times higher than for the background. Since the differential pump aperture does not completely limit the solid angle viewed by the ion source to beam species, some of the carrier gas (N_2 or Ar) admitted arises from the scattered background (in region I) and not the beam itself. This would not be the case for the condensible salt species. Hence, since the ion intensities of salt species are normalized against the carrier gas signal [by expressions (4.3) and (4.4)], as part of the pressure calibration procedure, they would be underestimated by the degree that scattered carrier gas competes with beam gas. Thus, in treating ion signals of condensible species relative to the carrier gas signal, we need to include an empirically determined multiplying factor of about 1.67 ($\bar{S} = 0.6$) as a calibration constant, e.g., in expression 4.4. This factor is essentially invariant with total pressure since the ratio of background to beam pressure remains constant for our unthrottled pumping system (see Section 3.2). We have applied this correction factor to all <u>condensible</u> species partial pressures included in this study.

An independent test and verification of this correction procedure will be demonstrated for the Na_2SO_4 system in Section 5. We should emphasize, however, that even without this correction the agreement between our data and the JANAF [26] values is well within that usually expected for vapor pressures of complex high temperature systems.

4.2.4 Data comparison with JANAF [26]

Below the melting point, the sublimation data (fig. 8) fit the least squares expression:

$$\log P_{NaCl}(atm) = 7.8(\pm 1.6) - 11970(\pm 1500)/T.$$

It follows that the enthalpy and entropy of sublimation (reaction R1) are, respectively,

$$\Delta H_s = 54.8 \pm 7 \text{ kcal/mol and } \Delta S_s = 35.6 \pm 8 \text{ cal/deg mol at 1000 K.}$$

For the liquid region, the corresponding data-fit is given by:

$$\log P_{NaCl}(atm) = 4.85(\pm 0.3) - 8820(\pm 200)/T,$$

and for reaction R2,

$$\Delta H_v = 40.4 \pm 0.9 \text{ kcal/mol and } \Delta S_v = 22.2 \pm 1.4 \text{ cal/deg mol at 1290 K.}$$

The enthalpy of sublimation compares favorably with the JANAF [26] selection of 51.6 ± 2.4 kcal/mol where the uncertainty represents the standard deviation in the second law data analyzed by JANAF [26]. For the liquid region, the literature data are based on total

387

pressure measurements (i.e., not molecular specific) which have been corrected for dimer contribution by extrapolating mass spectrometric data obtained over solid NaCl. JANAF [26] selects ΔH_v = 42.7 ± 3.5 kcal/mol and ΔS_v = 24.2 ± 0.5 cal/deg mol at 1290 K for reaction R2. Both sets of data are in very good agreement.

The key uncertainty in the present data arises from the cross section and $\bar{S}$ terms in expression 4.4. However, the agreement between NaCl pressures obtained by the methods (a) - (c) at 1360 K and a subsequent check on $\bar{S}$ using $Na_2SO_4^{-}$ strongly support the pressure calibration procedure and hence the entropy data.

In view of the sparsity of molecular specific measurements in the liquid range by other investigators, the general agreement between JANAF [26] and our data is excellent. Further, this appears to be the first report of measurements in the temperature range from the melting point to 1250 K. This result demonstrates an additional advantage of TMS over the classical effusion (e.g., Knudsen effusion mass spectrometry) and total pressure (e.g., conventional transpiration) methods in its ability to bridge the 10^{-4} - 10^{-3} atm gap in existing partial pressure measurement capability at high temperature. The temperature range of >450 K covered by our measurements is exceptionally large, and measurements over an even wider range are feasible with this technique.

4.3 NaCl dimerization and test for homogeneous equilibrium

The NaCl sublimation and vaporization reactions represented by the data in figure 8 provide a convincing test of the attainment of heterogeneous equilibrium, for condensible vapor species, in the transpiration reactor and their faithful sampling into the mass spectrometer. However, in the absence of additional experimental insight, it is conceivable that the sampling process could perturb homogeneous vapor phase chemical equilibria. A sensitive test of the system fidelity in this regard can be made using the known equilibrium represented by reaction R7.

It is well established from the literature, and our results support this, that the Na_2Cl^+ ion may be used as a measure of the dimer species $(NaCl)_2$. Our appearance potential and temperature dependence data indicate that Na_2Cl^+ is a fragment ion of $(NaCl)_2$ and that any Na^+ or $NaCl^+$ arising from dimer electron impact fragmentation is negligible (for present purposes). The equilibrium constant for the dimerization process (R7) is then given by:

$$K_d = \frac{I_{Na_2Cl^+}}{(I_{Na^+} \text{ or } I_{NaCl^+}^*)^2 k_{Na_2Cl_2} \cdot T} \qquad (4.6)$$

where $k_{Na_2Cl_2}$ includes the relative ionization cross section, mass spectrometer sensitivity, differential gas scattering and beam segregation factors for the monomer and dimer species, as discussed previously. The term $I_{NaCl^+}^*$ refers to the scaled $NaCl^+$ ion intensity, i.e., as in expression 4.5. In practice, where I_{Na^+} and $I_{Na_2Cl^+}$ are used as measures of monomer and dimer, respectively, $k_{Na_2Cl_2}$ = 4.0 k_{N_2}.

388
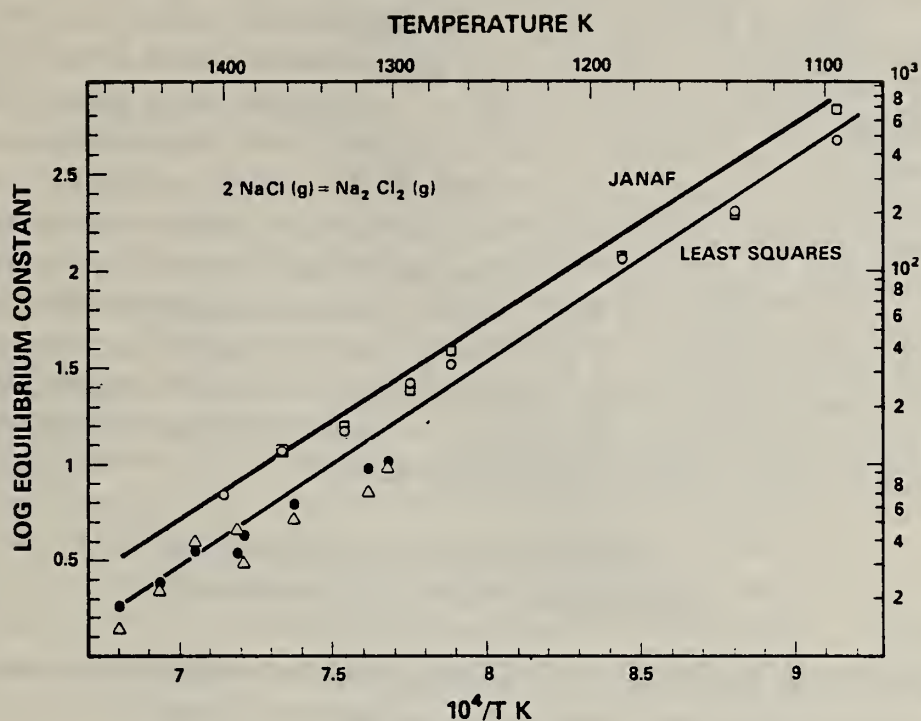
Figure 9. TMS data, at 30 eV with N_2 carrier gas for NaCl monomer – dimer equilibrium. Open circles and squares using capillary sampler at 0.3-0.5 atm with Na^+ and $NaCl^+$ (scaled--see text) as measures of P_{NaCl}, respectively. Closed circle and open triangle obtained with conical sampler, 0.4-0.6 atm, using Na^+ and $NaCl^+$ (scaled-- see text), respectively [see eq. (4.6) in main text].

Typical data sets for K_d as a function of temperature are given in figure 9. These data were obtained using both the conical and the capillary-type samplers. Note the satisfactory agreement between the various K_d data sets and the JANAF [26] literature curve, indicating good control over the various effects discussed earlier as contributing errors in converting ion intensity to partial pressure, or equivalent equilibrium constant, data. Both the I_{Na^+} [as per eq. (4.1)] and the scaled $I_{NaCl^+}^*$ [as per eq. (4.5)] signals were used as measures of P_{NaCl}. The least squares line shown in figure 9 is an average of individual least squares fits to each data set, giving

$$\log K_d = 10640 \ (\pm \ 400)/T - 6.97 \ (\pm \ 0.4).$$

The calculated enthalpy of dimerization (reaction R7) at 1265 K is then $\Delta H_d = -48.7 \ (\pm \ 1.8)$ kcal/mol, which is in good agreement with the selected JANAF [26] value of -47.1 kcal/mol, particularly since the corresponding literature data span a difference of more than 7 kcal/mol (see JANAF [26]). Our data for the conical probe were obtained at carrier gas

pressures varying over the range 0.4-0.6 atm and gas flow rates in the range 3-10 sccm. The capillary probe data, were obtained at pressures of 0.3-0.5 atm and gas flow rates in the range 15-40 sccm. That there is agreement between these data sets over a range of flow rates suggests saturated flow conditions in the transpiration reactor.

The isentropic expansion model discussed earlier (see Section 3.3) for the capillary sampler suggested that a temperature decrease of a few percent might occur in the early gas expansion phase along the capillary, while the velocity in the channel was still low enough that a re-adjustment of simple gas equilibria might be kinetically feasible. However, the generally good agreement between the capillary and conical samplers, and between the JANAF [26] literature data, suggests that during the early expansion period the isothermal model is a better description of capillary flow. That is, isentropic expansion dominates only when the remaining residence time in the capillary is a few microseconds and the flow velocity approaches unit Mach number. Direct computer modeling is required to predict more definitively the early flow conditions for this type of sampling orifice. However, the empirical approach adopted seems to satisfy present requirements.

4.4 NaCl vaporization at low pressures
using Knudsen effusion mass spectrometry

At the outset of the transpiration mass spectrometric studies we considered the accuracy of the literature data for NaCl vaporization, as compiled by JANAF [26], to be more than adequate for demonstrating and calibrating the TMS technique. However, small, but systematic, differences persisted between our measured dimerization reaction enthalpies and entropies and those recommended by JANAF [26]. That this difference occurred for different reactor and furnace geometries, different probe types, carrier gas flow rates and pressures, temperatures, thermocouples, mass spectrometers, ion sources, and sample loadings, seemed to rule out systematic error as an explanation. Closer inspection of the original literature data concerning the NaCl dimerization process revealed the thermodynamic data to be less definitive than suggested by the JANAF [26] compilation. The data for the liquidus NaCl region relied heavily on an extrapolation of solid NaCl data through the melting phase transition. We therefore considered it desirable to check the original dimerization data, as obtained over solid NaCl by Knudsen effusion mass spectrometry, using a similar technique ourselves. Such an experiment also served the useful purpose of providing an independent check on the $Na^+/NaCl^+$ (=R) characteristics for a thermal effusion beam of NaCl, as distinct from the non-thermal cool supersonic beams generated by the TMS method.

For these Knudsen effusion studies a lightweight platinum Knudsen cell with a leak free welded lid-seal was used in a vertical orientation. A Pt-Pt +10 %Rh thermocouple was used to measure the cell temperature at the base and an optical pyrometer (calibration traced to NBS standards) used to measure the effusion orifice temperature. These two independent temperature measurements agreed to within the pyrometer reading uncertainty of 5 K. As the thermocouple readings were of higher precision they were used as the primary source of

temperature data. A 33 mg sample was completely vaporized from a cell volume of 0.7 cm^3 through an orifice 0.051 cm diameter drilled in a lid of 0.01 cm thickness.

Figure 10 shows the ion intensity-temperature dependence plots for the major ion species--Na^+, $NaCl^+$, Na_2Cl^+ and $Na_3Cl_2^+$ [10]. Near the end of the experiment unsaturation effects were noted; see the high temperature region in figure 10. The sequence of loss-of-saturation followed the expected order of species loss, i.e., trimer > dimer > monomer. Note also in figure 10 that during the unsaturation period, both Na^+ and $NaCl^+$ continue to increase with temperature even though the dimer Na_2Cl^+ and trimer $Na_3Cl_2^+$ ion intensities fall off dramatically. This observation further supports the earlier assignments of ions to their neutral precursors. These data also show an essentially constant R ratio, even during unsaturation. As was mentioned earlier (Section 4.1) the magnitude of this ratio is con- siderably less than that obtained by TMS. · If the higher ratio found by TMS was related solely to <u>sample</u> temperature we should have expected the Knudsen effusion data to show a trend towards larger R values with increasing temperature. Thus our earlier interpretation of the corresponding TMS ratios seems consistent with these Knudsen data.

Conversion of the ion intensities to partial pressures was made using relationships of the same form as (4.1). The proportionality constant k_i, for species i, was determined using the established integrated signal-weight loss method [33] which can be expressed in the form:

$$k_i = \frac{G_i A_i (2\pi R)^{1/2} W}{aC(M_i)^{1/2} \Sigma [I_i(T)^{1/2} \Delta t]} \qquad (4.7)$$

where

    G is a gravimetric factor,

    A an isotopic abundance factor,

    R the universal gas constant,

    W the weight loss,

    a the orifice area,

    C the orifice Clausing factor,

    M the molecular weight,

    I the ion intensity,

    T the temperature, and

    Δt the elapsed time.

The contribution of the trimer to observed weight loss was neglected (<1 percent error). To calculate the individual k_i's for NaCl(g) and $(NaCl)_2$(g) it was necessary to estimate the relative concentrations for each species. Based on relative cross section estimates and the quadrupole mass discrimination for monomer and dimer species and their ion intensities (given in fig. 10), we partitioned the weight loss as ∿20(± 5) percent dimer and ∿80 percent monomer.

---

[10]Note that the $Na_3Cl_2^+$ ion was not routinely monitored during TMS experiments owing to its relatively low intensity and the preferential instrument tuning for low amu species.

This partitioning was considered acceptable as it produced NaCl monomer partial pressures in good agreement with JANAF [26]. From this partitioning estimate the above k_i expression (4.7) leads to

$$k_{(Na^+ + NaCl^+)} = 1.00 \times 10^{-11} \ (\pm \ 30 \ \%)\mu V/atm \ K, \ and$$

$$k_{(Na_2Cl^+)} = 4.15 \times 10^{-12} \ (\pm \ 30 \ \%)\mu V/atm \ K.$$
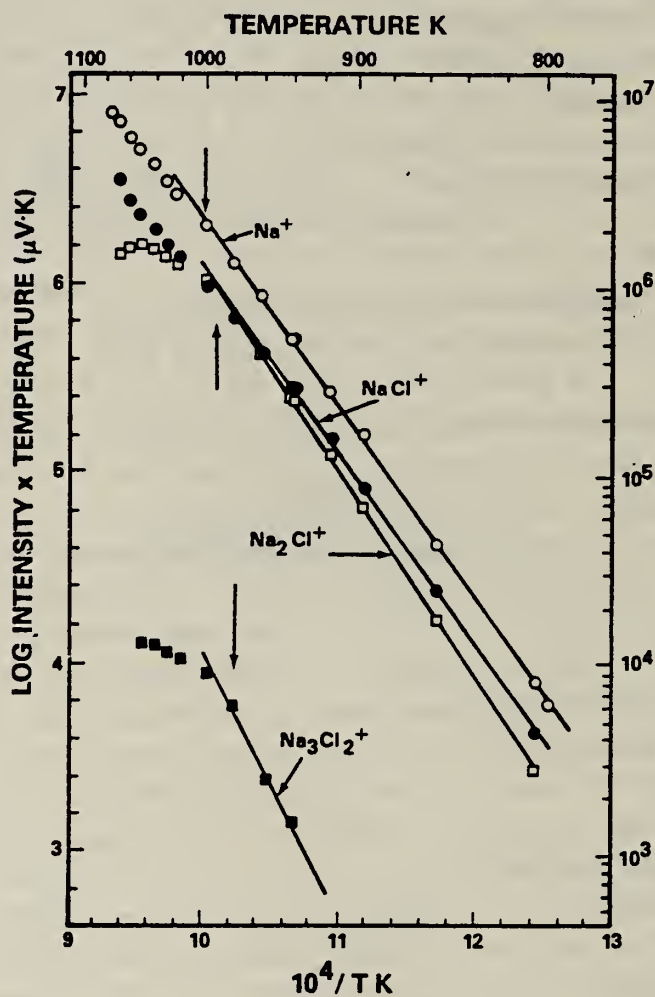
Figure 10. Kundsen effusion mass spectrometric data, expressed in the form of Clausius-Clapeyron plots, for vaporization of NaCl(s). Open circles - $Na^+(NaCl)$, closed circles - $NaCl^+(NaCl)$, open squares - $Na_2Cl^+(Na_2Cl_2)$, closed squares - $Na_3Cl_2^+(Na_3Cl_3)$. The Cl-containing species refer only to the ^{35}Cl isotopic species. Vertical arrows denote the end of saturated vaporization and the highest temperature included in the least squares fit. Experimental chronology was in the direction of increasing temperature.

392

These constants were used to convert the ion intensity data (fig. 10) to partial pressures, as shown in figure 11. The least squares lines have the algebraic form,

$$\log P_{NaCl} \text{ (atm)} = 5.75 \ (\pm 0.14) - 10170 \ (\pm 120)/T$$

$$\log P_{(NaCl)_2} \text{ (atm)} = 5.81 \ (\pm 0.11) - 11050 \ (\pm 100)/T$$

and yield, at ~900 K, in comparison with corresponding literature data (in parentheses)

ΔH_s (R1) = 46.5 ± 0.6 (52.3 [26]) kcal/mol

ΔS_s (R1) = 26.3 ± 0.6 cal/deg mol

ΔH_s (R3) = 50.6 ± 0.5 (57.0 [26]) kcal/mol, and

ΔS_s (R3) = 26.6 ± 0.5 cal/deg mol.

For the trimer (fig. 10 data),

ΔH_s (R5) = 62 ± 5 (62.2 ± 2.3 [31]) kcal/mol.

The monomer data are in good agreement with the JANAF [26] results (see fig. 11) but the corresponding dimer data show a significant, though not excessive, difference.
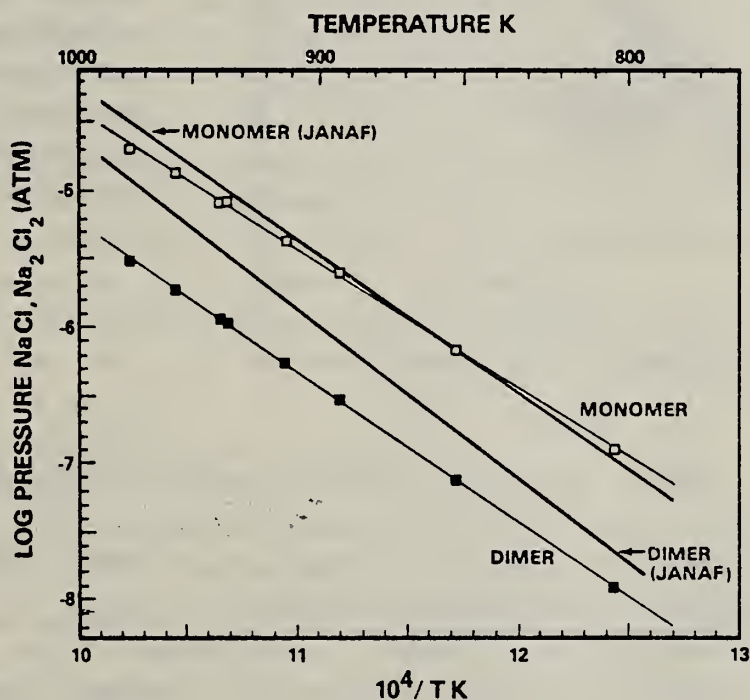
Figure 11. Vapor pressure of NaCl monomer and dimer obtained via Knudsen effusion mass spectrometry. Heavy curves represent the JANAF [26] data. Open squares – $P_{NaCl}(NaCl^+ + Na^+)$, closed squares – $P_{Na_2Cl_2}(Na_2Cl^+)$.

4.5 Comparison of Knudsen effusion and TMS-NaCl dimerization data

The various Knudsen effusion and TMS data sets have been replotted in the form of K_d (R7), as shown in figure 12. Table 4 summarizes the essential thermodynamic parameters represented by the various individual and combined data sets given in figure 12.
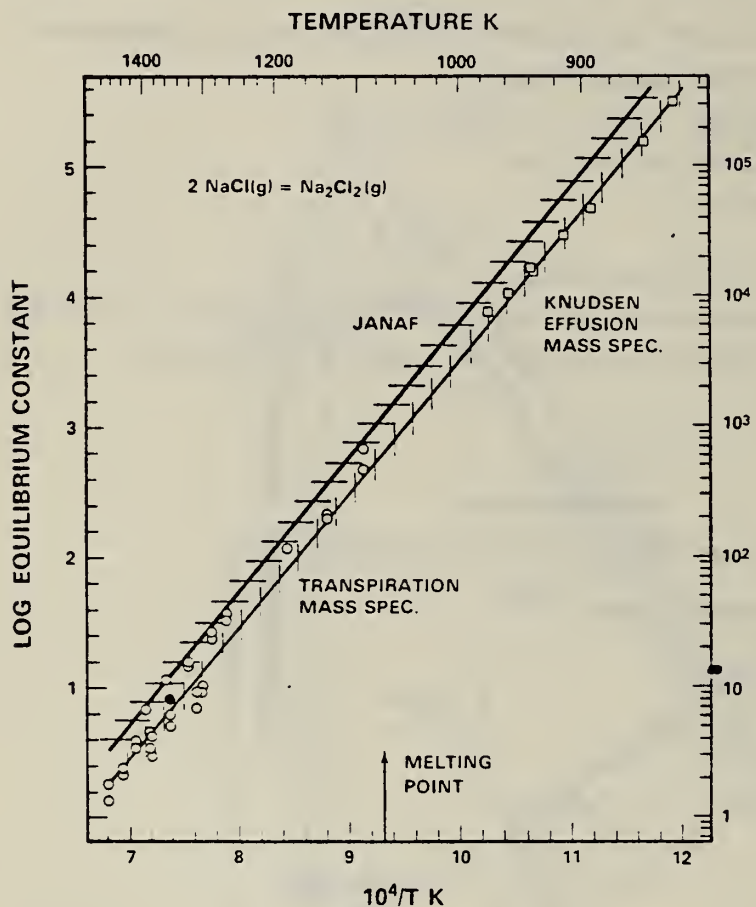
Figure 12. Comparison of various data sets for NaCl dimerization (reaction R7) (see also table 4). Horizontal and vertical bars indicate (to a good approximation) the slope uncertainties for the JANAF [26] and experimental curves, respectively (see text). The closed circle data point was obtained using calibration method (a) (see Section 4.2.1).

Table 4. Comparison of dimerization data (reaction R7).

$\log K_d$ atm^{-1}	$-\Delta H_d$ kcal/mol	$-\Delta S_d$ cal/deg mol	T Range K	Data source
$\dfrac{9300\ (\pm\ 200)}{T}$ $-5.70\ (\pm\ 0.2)$	42.5 ± 0.8	26.1 ± 0.9	820-980	Knudsen MS (fig. 11)
$\dfrac{10640\ (\pm\ 400)}{T}$ $-6.97\ (\pm\ 0.4)$	48.7 ± 1.8	31.9 ± 1.8	1100-1480	TMS (fig. 9)
$\dfrac{10312\ (\pm\ 150)}{T}$ $-6.49\ (\pm\ 0.1)$	47.1 ± 3.5	29.7 ± 1.0	800-1600	JANAF [26]
$\dfrac{10140\ (\pm\ 150)}{T}$ $-6.60\ (\pm\ 0.13)$	46.4 ± 0.7	30.2 ± 0.6	820-1480	Knudsen + TMS (fig. 12)

Note (in fig. 12) that our Knudsen effusion data extrapolate almost perfectly to the liquidus data curve obtained by TMS. Thus both the Knudsen effusion and TMS data sets appear to be more consistent with each other than with the JANAF [26] data, though the difference is not disturbingly great and is almost within the combined data uncertainties (see fig. 12). Such agreement between widely differing measurement techniques clearly establishes the TMS method as reliable and accurate, and capable of extending the pressure range of conventional effusion methods by four orders of magnitude or greater. The temperature range is also naturally extended by such a high pressure sampling capability.

5. The Na_2SO_4 System: Results and Discussion

Most practical systems adaptable to characterization by the TMS technique are heterogeneous, involving equilibria between reactive gases and volatile substrates. Experience with Knudsen effusion mass spectrometric studies of gas-solid (or liquid) systems has indicated a need to exercise great care in achieving, and then demonstrating, thermodynamic equilibrium[11]. On the other hand, considerable experience has shown that equilibria involving only condensible vapor species and their substrates are generally attainable in Knudsen cells.

With the TMS technique, the results for the NaCl system clearly demonstrated the presence of a thermodynamic equilibrium between condensible vapor species and the corresponding substrate. However, these data showed the need for a small, but noticeable, correction factor in relating partial pressures of condensible NaCl species to the carrier gas pressure (see fig. 8). This effect was attributed to mass spectral contributions of non-beam scattered carrier gas. Such an effect should also be present in heterogeneous systems where the scatterable gas is one of the reaction components. To further test our interpretation and data correction procedure for this effect, and to validate the TMS technique for the more general, but more difficult, case of heterogeneous gas-solid (or liquid) equilibria, we selected the Na_2SO_4 system as a test case.

This system is known [34-38] to vaporize according to one or more reactions:

$$Na_2SO_4(s,l) = 2Na + SO_2 + O_2 \qquad\qquad R9$$
$$Na_2SO_4(s,l) = Na_2SO_4 \text{ (g)} \qquad\qquad R10$$
$$Na_2SO_4(s,l) = Na_2O \text{ (soln or gas)} + SO_2 + 1/2 \ O_2 \qquad\qquad R11$$
$$SO_3 = SO_2 + 1/2 \ O_2 \qquad\qquad R12$$
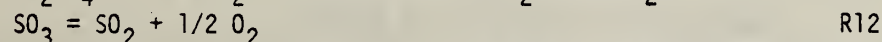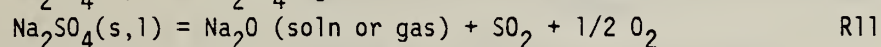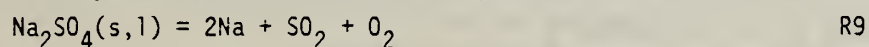
Historically, there has been considerable disagreement among researchers concerning the relative contribution of each reaction to the overall vaporization process (see table 5 in Section 5.5). It now appears that container reactions (catalytic or otherwise), temperature, sample treatment, and gas composition (e.g., external O_2 or SO_2 present), all contribute to the overall process defined by reactions R9-R12. For the high temperature (>1360 K) conditions of interest to the present study, we can readily eliminate reaction R12 as a contributing process. Previous mass spectrometric observations of Kohl, et al. [37] indicate that above 1300 K, SO_3 dissociation is favored and this species forms less than 10 percent of the

---

[11]For example, see the chapter by Hildenbrand elsewhere in this volume - "Attainment of Chemical Equilibrium in Effusive Beam Sources of the Heterogeneous Reaction Type."

vapor. Our own observations indicate SO_3 to be barely detectable at ~1100 K and virtually absent at higher temperatures.

As will be shown later (Sections 5.4 and 5.5), for most conditions reaction R9 is usually predominant. This is a very convenient reaction for a critical test of TMS sampling of gas-condensed phase equilibria. In addition to carrying out temperature dependence studies for the isolated system, it is possible to externally control the concentration of product species SO_2 and O_2 and provide an isothermal mass action (or Le Chatelier effect) test for equilibrium. With our particular design of external gas supply multiple mass flow meter/ controller system we were able to introduce either SO_2, O_2 or their mixtures at concentrations, with respect to the N_2 or Ar carrier gas, in the range of ~0.02-4 percent. Usually we maintained a constant O_2 pressure and varied the SO_2 concentration. The capability for varying the SO_2 partial pressure over a range of two orders of magnitude was more than adequate for a mass action test of equilibrium sampling.

5.1 Sample preparation and side reactions

Certified ACS grade anhydrous Na_2SO_4, supplied by Fisher Scientific Company (lot number 770832), was used as a starting material. Initial preparation techniques for our transpiration runs involved melting Na_2SO_4 into the transpiration boat at 1200 K using a muffle furnace under ambient conditions. Observations of Na^+ and CO_2^+ in the initial mass spectra at relatively low temperatures of 900-1100 K lead us to the conclusion that a small quantity of the salt reacted with atmospheric CO_2 to form Na_2CO_3. Under vacuum vaporization conditions, Na_2CO_3 decomposes according to the reaction:

$$Na_2CO_3(s,l) = 2Na + CO_2 + 1/2\ O_2 \quad ,$$
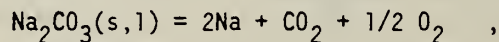
leading to much higher Na pressures at low temperatures than for reaction R9. These impurity signals disappeared during the pre-run bake out period.

Another impurity reaction noted by Fryxell, et al. [34] is

$$2NaHSO_4(s,l) = Na_2SO_4(s,l) + H_2SO_4 \quad ,$$
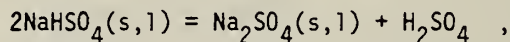
followed at elevated temperatures by

$$H_2SO_4 = H_2O + SO_2 + 1/2\ O_2 \quad .$$
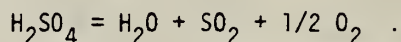
Consistent with this process we observed, during the initial measurement phase with fresh samples, impurity signals of SO_2 and H_2O at temperatures of about 1300 K. However, these impurities could be readily removed by a period of outgassing prior to commencement of a measurement run.

The presence of trace amounts of water in the system, either in the sample itself or as an impurity in the carrier gas, could alter the Na_2SO_4 vaporization process according to

396

the reaction

$$Na_2SO_4(s,l) + H_2O = 2NaOH \text{ (soln or gas)} + SO_2 + 1/2 \text{ } O_2 \text{ . } \quad R13$$

To remove water from the sample, the salt was heated for a 6-12 hour period at 400 °C in the assembled transpiration system prior to beginning an experimental run. This in situ drying process was monitored mass spectrometrically by following the decay of the H_2O^+ ion signal. Background H_2O from the aluminum walls of the stage I vacuum region limited ultimate H_2O detection sensitivity to ~25 ppm. The zero grade nitrogen and pre-purified argon contained <3 ppm H_2O (Matheson supplied specification). This specification was verified by us where a dew point of less than -80 °C was found. Even using our limited detection sensitivity as an upper limit for P_{H_2O}, and allowing reaction R13 to set the values for P_{SO_2} and P_{O_2}, we can show from the JANAF [26] values of $K_p(R13)$ that P_{NaOH} is negligible. During experimental runs with nitrogen as a carrier gas we periodically monitored the ions 40 $(NaOH^+)$, 39 (NaO^+), 80$[(NaOH)_2^+]$ and 79 $(Na_2O_2H^+)$ amu but no evidence for these species was found, in agreement with the thermodynamic prediction.

The following arguments can be made concerning the possible competition of reactions R10 and R11 with reaction R9. Cubicciotti and Keneshea [35] have calculated reaction R11, with $Na_2O(g)$ as a product, to be ~10 orders of magnitude less significant than reaction R9. We can also show the corresponding reaction leading to Na_2O (soln) to be insignificant in this system. From JANAF [26], the equilibrium constant for the reaction

$$Na_2O \text{ (soln)} = 2Na + 1/2 \text{ } O_2 \text{ .} \quad R14$$
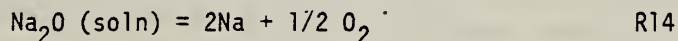
at 1500 K has a calculated value of

$$\log K_p(R14) = \log \left[\frac{P_{Na}^2 \text{ } P_{O_2}^{1/2}}{a_{Na_2O}} \right] = -5.9;$$

similarly for reaction R9 at 1500 K,

$$\log K_p(R9) = \log \left[\frac{P_{Na}^2 \cdot P_{SO_2} \cdot P_{O_2}}{a_{Na_2SO_4}} \right] = -16.4.$$

With the reasonable assumption that the activity $a_{Na_2SO_2}$ ~1, and congruent vaporization, reaction R9 requires a materials balance

$$1/2 \text{ } P_{Na} = P_{SO_2} = P_{O_2} \text{ .}$$

Hence, the sodium pressure can be given as

$$P_{Na} = [4 \ K_p(R9)]^{1/4} \sim 1 \times 10^{-4} \text{ atm (at 1500 K).}$$

Substitution of this value into the equilibrium constant expression for reaction R14 with the approximation that $1/2 \ P_{Na} = P_{O_2}$ (valid if reaction R9 is dominant) predicts

$$a_{Na_2O} < 4 \times 10^{-5}.$$

This predicted low activity of the basic oxide is supported by the observations of Fryxell, et al. [34] that their post-run salt exhibited a neutral pH. Likewise, our post-run samples, even for experiments as short as 2-3 hr, did not exhibit any basic pH character.

From these considerations we can eliminate reactions R11-R14 as possible contributing factors to Na_2SO_4 vaporization.

5.2 Closed system temperature dependence

Under closed system conditions, i.e., no external reactive gas load applied, we observed reaction R9 as the predominant process in the temperature range ca 1400-1700 K. The measured temperature dependence of the equilibrium constant,

$$K_p(R9) = P_{Na}^2 \cdot P_{O_2} \cdot P_{SO_2} \qquad (5.1)$$

is shown in figure 13, where an excellent agreement with the JANAF [26] curve is indicated. The right-hand side axis represents an equivalent partial pressure of sodium calculated from the observed $K_p(R9)$ using $P_{Na} = [4K_p(R9)]^{1/4}$. This is a useful representation of $K_p(R9)$ for making comparisons with the literature data, as will be shown in Section 5.5.

The partial pressures were obtained using the established relation,

$$P_i = k_i I_i^+ T$$

for conversion of the ion intensities for Na^+ (23 amu), SO_2^+ (64 amu), and O_2^+ (32 amu). k_i was derived from k_{Ar} or k_{N_2} at each temperature T where

$$k_{Ar} = \frac{P_o \cdot f_i}{I_{36_{Ar}} \cdot T} \text{ and } k_{N_2} = \frac{P_o \cdot f_i}{I_{29_{N_2}} \cdot T} \quad ,$$

P_o is the source pressure of carrier gas (Ar; N_2),

$I_{36_{Ar}}$ the ion intensity of the argon isotope at 36 amu,

$I_{29_{N_2}}$ the ion intensity of the nitrogen isotope at 29 amu,

$f_i = 0.0034$ is the ^{36}Ar isotope fraction of argon gas, and

$f_i = 0.0072$ is the $^{29}N_2$ isotope fraction of N_2 gas.
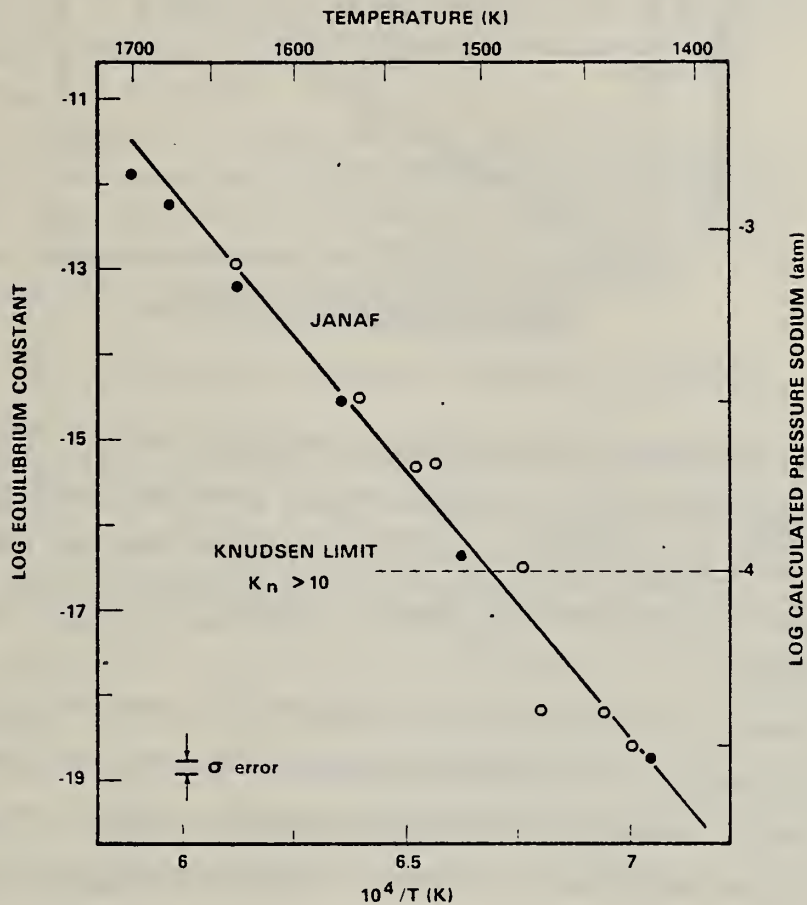
Figure 13. Temperature dependence of the equilibrium constant for reaction $Na_2SO_4(1) = 2Na + SO_2 + O_2$ from TMS observations of Na^+, SO_2^+ and O_2^+. Data taken at 30 eV ionizing electron energy using Ar carrier gas at pressures of 0.4 atm (closed circles) and 0.5 - 0.8 atm (open circles). The solid line is taken from JANAF [26]. The Knudsen limit was estimated for a cell with ~0.1 mm orifice diameter. The right-hand side axis has been calculated, assuming congruent vaporization, as $P_{Na} = [4K_p(R9)]^{1/4}$.

A typical data point for figure 13 is given by the experimental parameters:

T = 1563 K, $P_{Ar} = 0.81$ atm, $I_{36_{Ar}} = 26 \times 10^3$, $I_{Na} = 2100$, $I_{SO_2} = 500$ and $I_{O_2} = 2300$ μV. These data agree within experimental error with the JANAF $K_{Na_2SO_4}$ data if a scattering

399

factor of $\bar{S} = 0.6$ (± 0.06) is assumed. That this factor has the same magnitude as for the NaCl study tends to establish its use as a universal correction factor for our particular TMS system.
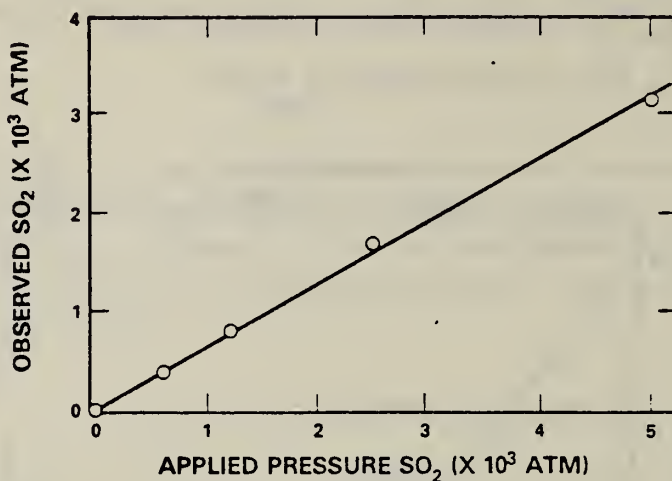
Figure 14. Dependence of "observed" SO_2 on externally applied partial pressure; where $P_{SO_2}(obs) = k_{N_2} \cdot I_{SO_2}^{+} \cdot T$. Data taken at 30 eV ionizing electron energy and 1485 K using N_2 carrier at ~0.6 atm in the presence of Na_2SO_4. The least squares fit yields the relationship $P_{SO_2}(appl) = 1.55$ (± 0.5) $k_{N_2} I_{SO_2}^{+} \cdot T + 2.5$ (± 0.2) x 10^{-5} atm.

The constants k_i are then derived as follows. For the case of k_{SO_2}, use can be made of the system response to a known external pressure of SO_2. Figure 14 indicates the relationship between calculated and "observed" pressures for SO_2, where the observed data refer to k_{N_2} as the proportionality constant. The figure shows the excellent linear response of the mass spectrometer system to known concentrations of reactive gas species and gives a direct relation between observed intensity and true pressure. These data may be used to derive cross sections, such as those given in table 4. From the slope of the line in figure 14 we obtain,

$$\frac{P_{SO_2}(obs)}{P_{SO_2}(appl)} = \frac{k_{N_2} \cdot I_{SO_2}^{+} \cdot T}{k_{SO_2} \cdot I_{SO_2}^{+} \cdot T} = \frac{1}{1.55} \; ;$$

hence, $k_{SO_2} = 1.55 \, k_{N_2}$ (at 30 eV). With the mass discrimination function of figure 6, the

cross section data of table 4, and the scattering correction (multiplication factor of 1.67) obtained from the NaCl TMS data, the equilibrium constant is then

$$K_P(R9) = 4.8(k_{Ar}T)^4 (I_{Na}^+)^2 \cdot I_{SO_2}^+ \cdot I_{O_2}^+ \quad . \qquad (5.2)$$

The data represented in figure 13 were obtained at various argon carrier gas pressures P_0, in the range of 0.4 - 0.8 atm. Separate least squares fits to the low (0.4 atm) and high (0.5 - 0.8 atm) P_0 data points yield, respectively (in terms of Na):

ΔH_v = 69 ± 1 and 71 ± 4 kcal/mol

ΔS_v = 27.5 ± 1.5 and 28.1 ± 4 cal/deg mol (for reaction R9).

The good fits within and between various total pressure-ranges is indicative of saturated sampling conditions since the carrier gas flow rate is proportional to P_0 at constant T. Also, the excellent agreement with the JANAF [26] data for both ΔH_v and ΔS_v (evident in fig. 13) is consistent with a non-perturbing sampling process.

5.3 Open system, isothermal, variable SO_2 conditions

The effect of variable SO_2 pressure on the equilibrium constant for reaction R9 at near isothermal conditions (1475 ± 7 K) is shown in figure 15. Note that the least squares curve has zero slope [required by definition of $K_p(R9)$] and is located very close to the JANAF [26] curve. There are two contributing factors to the data scatter observed in figure 15. First, during the runs, the VARIAC driven furnace system allowed a temperature variation of ±7 K, due partly to fluctuations in line power and to interaction of variable background SO_2 with the thin-foil tantalum furnace. The second factor resulted from a slow response of $I_{SO_2}^+$ to changes in applied P_{SO_2} from high to low SO_2 concentrations. This slow response is believed to result from SO_2 dissolving, and being retained, in the liquid Na_2SO_4.

5.4 Closed-system Knudsen effusion mass spectrometric results

There appears to be considerable discrepancy in the data obtained by various methods, and in different laboratories, concerning the relative contribution of reactions R9 and R10 to the overall Na_2SO_4 vaporization process (e.g., see later in table 5). For the TMS studies considered so far, emphasis has been on reaction R9. No attempt was made to study reaction R10 in this work; in fact the mass spectrometer tuning was optimized for the low mass range needed for Na, O_2 and SO_2 rather than for the species Na_2SO_4. In order to be sure that reaction R10 does not compete appreciably with reaction R9 for our TMS conditions, we undertook a Knudsen effusion mass spectrometric study of Na_2SO_4. The apparatus and experimental procedures used were very similar to those indicated for the NaCl study (Section 4.4). An all-platinum Knudsen cell was used to avoid the sample-cell interaction problems reported by others (e.g., see table 5).
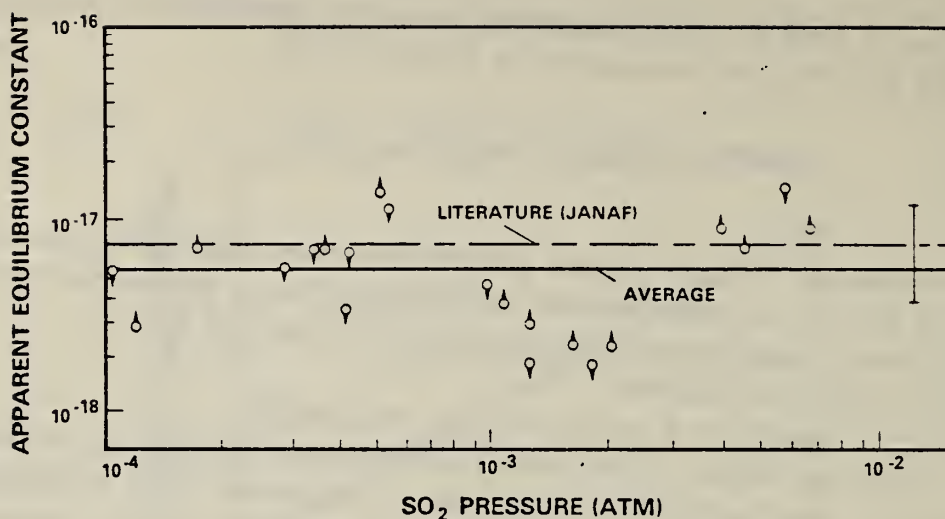
Figure 15. Isothermal equilibrium behavior of $K_p(R9)$ with variable SO_2 partial
pressure at 1475 (±7) K, using N_2 carrier gas at 0.5 atm and 30 eV ionizing
electron energy. Error bar on JANAF [26] value (broken line) represents the
change in $K_p(R9)$ for the experimental temperature variation of ±7 K. The solid
line is the average of all measurements; a two parameter fit yields a similar
result with a statistically insignificant pressure dependent term. Arrows on
data symbols indicate the direction of change of applied SO_2 pressure. Three
symbols with double arrows denote the turning points of the two cycles of
variation in SO_2.

Our mass spectrometric results, plotted as log (I·T) vs 1/T for the principal ions Na^+
and $Na_2SO_4^+$ are given in figure 16. The Na^+ curve gives an enthalpy of vaporization (R9)
as sodium of 72.3 ± 4 kcal/mol at 1165 K, in excellent agreement with the JANAF [26] data.
From the $Na_2SO_4^+$ curve we obtain a second law enthalpy for reaction R10 of

$$\Delta H_{Na_2SO_4} = 65.1 \pm 3.5 \text{ kcal/mol},$$

which is in very good agreement with the result of Kohl, et al. [37] (shown in table 5).
The location of their least squares curves for $Na_2SO_4^+$ (relative to Na^+) are indicated for
comparison in figure 16, using the same relationship between $Na_2SO_4^+$ and Na^+ as given in
their reported mass spectrum. The agreement for the relative importance of Na_2SO_4 and Na
between the laboratories of Kohl, et al. [37] and ours is quite satisfactory. Also within
the errors quoted, and considering the differences in mean temperature, both mass spectro-
metric studies are in good agreement with the transpiration measurements of Cubicciotti
and Keneshea [35].

402
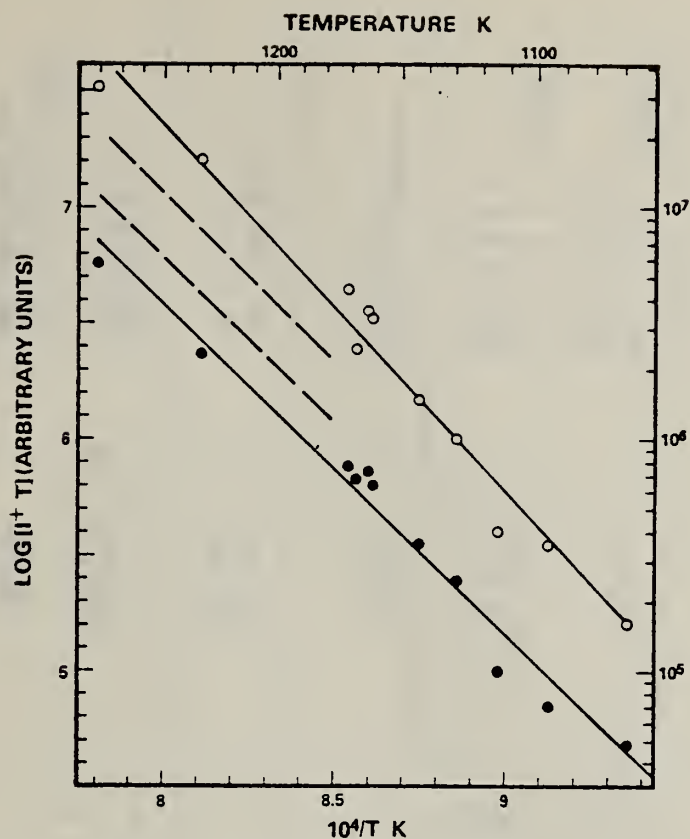
Figure 16.   Knudsen effusion mass spectrometric data for $I_{Na}{}^{+}\cdot T$ and $I_{Na_2SO_4}{}^{+}\cdot T$

from $Na_2SO_4(1)$.   Open circles are $I_{Na}{}^{+}T$ and closed circles are $I_{Na_2SO_4}{}^{+}T$ data,

corrected by effusive mass discrimination plot of figure 6.   Due to a substantial

time difference, and instrumental changes between obtaining the figure 6 data and

these results, the relative locations of the two lines could be uncertain by a

factor of 2.   Broken lines represent two sets of $I_{Na_2SO_4}{}^{+}\cdot T$ data from Kohl, et al.

[37] located relative to our fitted $I_{Na}{}^{+}\cdot T$ line using their reported mass spectral

relative intensities [their fig. 2(b)].

5.5   Data summary and literature comparison

Table 5 summarizes the most recent literature for the Na_2SO_4 vaporization process(es).
As total vaporization techniques do not monitor individual species, they usually do not
identify the separate contributions from reactions R9 and R10.   The data reviewed, including
molecular specific results, are therefore expressed in terms of P_{Na} for comparison with
the literature total vaporization data.   The decomposition data (reaction R9) have been
converted using the assumption of congruent vaporization, i.e., $P_{Na} = 2P_{SO_2} = 2P_{O_2}$ as dis-
cussed above.   In the case of the data reported by Ficalora, et al. [36], their cited result

Table 5. Comparison of data among various investigators[a]

Authors	Range K	Method	System materials	Carrier gas	Vapor species	Results[b]
Fryxell Trythall Perkins [34]	1227 - 1477 $\bar{T}$ = 1340	transpiration (wt loss)	platinum, mullite	air	Na_2SO_4	Log P = 6.04 - 15870/T ΔH = 72.6 ± 3.5 ΔS = 27.6 ± 2.5
Cubicciotti Keneshea [35]	1400 - 1625 $\bar{T}$ = 1504	transpiration (collection)	platinum	$O_2 + SO_2$	Na_2SO_4	LOG P = 5.86 - 15540/T ΔH = 71.1 ± 1.7 ΔS = 26.8 ± 0.7
	$\bar{T}$ = 1518			N_2	$2Na + SO_2 + O_2$ as Na	LOG P = 7.11 - 16480/T ΔH = 75.4 ± 1.7 ΔS = 32.4 ± 1.0
Uhlig Davis Graham [38]	1175 - 1375 $\bar{T}$ = 1267	transpiration free evaporation	platinum		Na_2SO_4	LOG P not obtained ΔH = 71
Ficalora, uy Muenow Margrave [36]	1020 - 1150 $\bar{T}$ = 1081	Knudsen ms w/shutter	tantalum, alumina		$\underline{2Na + SO_2 + O_2}$ as Na	LOG P not given ΔH = 74.8 ± 1.3
Kohl Stearns Fryburg [37]	1196 - 1400 $\bar{T}$ = 1290	Knudsen ms w/shutter	platinum, alumina		$\underline{2Na + SO_2 + O_2}$ as Na	LOG P not given ΔH = 73.5 ± 2.5
	1175 - 1375 $\bar{T}$ = 1267				$\underline{Na_2SO_4}$	LOG P = 4.87 - 14440/T ΔH = 65.9 ± 3 ΔS = 22.3 ± 2.8
JANAF [26]	1400 - 1700 $\bar{T}$ = 1536	selected	--		$Na_2SO_4(l)$ = as Na	LOG P = 6.49 - 15670/T ΔH = 71.7 ± 0.6 ΔS = 29.7

404

Table 5 (continued)

this work	1069 - 1281 $\bar{T} = 1165$	Knudsen modulated beam ms	platinum	$\underline{2Na} + SO_2 + O_2$ as Na $_2$ $\underline{Na_2SO_4}$	LOG P not obtained $\Delta H = 72.3 \pm 4$ LOG P not obtained $\Delta H = 65.1 \pm 3.5$
	1400 - 1701 $\bar{T} = 1550$	transpiration modulated beam	platinum, trace alumina	N_2 or Ar	$\underline{2Na} + SO_2 + \underline{O_2}$ as Na	LOG P = 6.16 - 15300/T $\Delta H = 69.8 \pm 3$ $\Delta S = 27.8 \pm 3$

[a] Underlined species observed directly.

[b] P in atm; ΔH in kcal/mol; ΔS in cal/deg mol, at $\bar{T}$.

(1 atm = 1.01325 x 10^2 kpascal; 1 cal = 4.184 J).

for ΔH_{Na} (= 78.8 ± 3.3 kcal/mol) was not in agreement with the result calculable from their raw data (their fig. 3), and we have listed the latter in table 5.

In the study of Ficalora, et al. [36] no ion attributable to $Na_2SO_4(g)$ was observed and they concluded that reaction R9 together with the gas phase equilibrium R12 best described the vaporization of $Na_2SO_4(s)$. The work of Kohl, et al. [37] included tests for sample interaction with tantalum and tungsten cells using ZrO_2 liners, and with platinum cells with or without Al_2O_3 liners. Their results indicated a significant enhancement of Na^+ and SO_2^+ signals relative to $Na_2SO_4^+$ from the ZrO_2 lined tantalum and tungsten cells, and formation of additional species due to sample reduction by the tungsten cell. They concluded that Ficalora, et al. [36] failed to identify $Na_2SO_4^+$ because of a cell-interaction enhancement of reaction R9.

Transpiration data, in an all-platinum apparatus., were obtained by Cubicciotti and Keneshea [35]. They distinguished between reactions R9 and R10 by using, separately, an atmosphere of pure N_2 and of 1/2 SO_2 + 1/2 O_2. Uhlig, et al. [38] assert that the only vapor species present in their studies is Na_2SO_4, as no dependence of vaporization rate on an applied O_2 partial pressure was observed. This result is inconsistent with our data and indeed the bulk of the literature. Their static technique is highly surface layer diffusion controlled, as evidenced by the fact that the actual weight-loss rate is much lower than expected from a saturated flow or vacuum evaporation system.

In conclusion, the summary of table 5 clearly indicates the inherent and historical problems associated with the Na_2SO_4 vaporization system and, in comparison, the quality of the TMS data must be considered very good. The reliability of the TMS technique for heterogeneous gas-liquid (or solid) systems, as demonstrated for the very demanding Na_2SO_4 system, appears to outweigh that of alternative approaches.

References

[1] Hastie, J. W., High Temperature Vapors: Science and Technology (Academic Press, New York, 1975).

[2] Hastie, J. W., Intl. J. Mass Spectrom. Ion Phys. 16, 89 (1975); Combust. Flame, 21, 49 (1973).

[3] Stearns, C. A., Kohl, F. J., and Fryburg, G. C., this volume (1979).

[4] Merten, U. and Bell, W. E., in The Characterization of High Temperature Vapors, J. L. Margrave, ed., p. 91 (Wiley, 1967).

[5] Gordon, R. J., Lee, Y. T., and Herschbach, D. R., J. Chem. Phys. 54, 2393 (1971).

[6] Kantrowitz, A. and Grey, J., Rev. Sci. Instr. 22, 328 (1951).

[7] Parker, H. M., Kuhlthau, A. R., Zapata, R., and Scott, J. E., Jr., Rarefied Gas Dynamics, Proc. First Int. Symp., F. M. Devienne, ed., 1, 69 (1960).

[8] Anderson, J. B. and Fenn, J. B., Phys. Fluids, 8, 780 (1965).

[9] Ashkenas, H. and Sherman, F. S., Rarefied Gas Dynamics, Proc. Fourth Int. Symp., J. H. deLeeuw, ed., 2, 84 (1966).

[10] Bier, K. and Hagena, O., ibid, 200 (1966).

[11] Knuth, E. L., Appl. Mech. Rev. 17, 751 (1964).

[12] Morris, J. F., The Chemistry of Propellants, AGARD Symposium, S. S. Penner and J. Ducarme, eds., 410 (Pergamon Press, N. Y., 1960).

[13] Sherman, F. S., Second Biennial Gas Dynamics Symposium, Am. Rocket Soc. (Northwestern University, 1957).

[14] Bray, K. C. N., Ninth Symposium (International) on Combustion, 770 (Academic Press, N. Y., 1963); and J. Fluid Mech. 6, 1 (1959).

[15] Wegener, P. P., Combustion and Propulsion, Fourth AGARD Symposium, A.C. Jourmatte, A. H. Lefebvre and A. M. Rothrock, eds., 261 (Pergamon Press, N. Y., 1961).

[16] Hayhurst, A. N. and Telford, N. R., Proc. Roy. Soc. London, A322, 483 (1971).

[17] Greene, F. T., Brewer, J., and Milne, T. A., J. Chem. Phys. 40, 1488 (1964).

[18] Abuaf, N., Anderson, J. B., Andres, R. P., Fenn, J. B., and Marsden, D. G. H., Science, 156, 997 (1967).

[19] This collision diameter is from Anderson and Fenn (ref [8]) for monatomic gases $\delta = 5/3 = C_p/C_v$. A larger collision diameter for diatomic N_2 makes Kn_0 smaller. The choice of 3.7×10^{-8} cm for this calculation shows $Kn_0 < 0.01$ for argon which was used for some studies.

[20] Stearns, C. A., Kohl, F. J., Fryburg, G. C., and Miller, R. A.; NASA Technical Memorandum 73720 (1977) and references cited therein.

[21] Brown, R. F. and Heald, J. H., Jr., Rarefied Gas Dynamics, Proc. Fifth Int. Symp., 1407 (1966).

[22] Stern, S. A., Waterman, P. C., and Sinclair, T. F., J. Chem. Phys. 33, 805 (1960).

[23] Reis, V. H. and Fenn, J. B., J. Chem. Phys. 39, 3240 (1963).

[24] Sherman, F. S., Phys. Fluids, 8, 773 (1965).

[25] Milne, T. A. and Greene, F. T., J. Chem. Phys. 47, 4095 (1967).

[26] JANAF Thermochemical Tables, 2nd ed., NSRDS-NBS 37 (1971), U. S. Govt. Printing Office, Washington, D.C.

[27] Barton, J. L. and Bloom, H., J. Phys. Chem. 60, 1413 (1956); ibid. 63, 1785 (1959).

[28] Miller, R. C. and Kusch, P., J. Chem. Phys. 25, 860 (1956); ibid. 27, 981 (1957).

[29] Milne, T. A. and Klein, H. M., J. Chem. Phys. 33, 1628 (1960).

[30] Akishin, P. A., Gorokhov, L. N., and Sidorov, L. N., Russian J. Phys. Chem. 33, 2822 (1959).

[31] Feather, D. H. and Searcy, A. W., High Temp. Sci. 3, 155 (1971).

[32] Berkowitz, J., Tasman, A. A., and Chupka, W. A., J. Chem. Phys. 36, 2170 (1962).

[33] Margrave, J. L., ed., The Characterization of High Temperature Vapors, p. 38 (Wiley, New York, 1967).

[34] Fryxell, R. E., Trythall, C. A., and Perkins, R. J., Corrosion-NACE, <u>29</u>, 423 (1973).

[35] Cubicciotti, D. and Keneshea, F. J., High Temp. Sci. <u>4</u>, 32 (1972).

[36] Ficalora, P. J., Uy, O. M., Muenow, D. W., and Margrave, J. L., J. Amer. Ceram. Soc. <u>51</u>, 574 (1968).

[37] Kohl, F. J., Stearns, C. A., and Fryburg, G. C., <u>Metal-Slag-Gas</u> <u>Reactions</u> <u>and</u> <u>Processes</u>, Z. A. Foroulis and W. W. Smeltzer, eds., p. 649 (The Electrochemical Society, 1975); also NASA TMS 71641.

[38] Uhlig, G. F., Davis, H. H., and Graham, H. C., J. Amer. Ceram. Soc. <u>58</u>, 201 (1975).

[39] Kieffer, L. J. and Dunn, G. H., Rev. Mod. Phys. <u>38</u>, 1 (1966).

[40] Meyer, R. T. and Lynch, A. W., High Temp. Science, <u>5</u>, 192 (1973).

Discussion

<u>Moderator</u> (Green): You showed that the partial pressure in the high pressure molecular beam sampling system was proportional to the intensity times the temperature, which is a little bit surprising, though I expect it is right. But you actually used this relationship?

<u>Response</u> (Bonnell): Yes, we do. What we actually do is monitor the carrier gas along with everything that moves with it, i.e., the transported vapor. We use the carrier gas (known pressure) through $P=kIT$ to back-calculate an effective instrument constant, k, for every data point taken. (Actually when we do this at every temperature we simply use ion intensity ratios.) The real point is that the beam characteristics outside of the effusive nature of that function are carrier gas dependent. And one really does need to take a measurement on the carrier gas each time.

We find that the function (i.e., k) varies slowly with T and P. We could, in fact, process our data with the average of all the instrument constants (k) we calculate. But, it is rougher. There is actually a dependence on the expansion process that is observable as a change in instrument constant, particularly as a function of temperature in the transpiration cell.

<u>Question</u> (Hildenbrand): I didn't understand the explanation for your sodium chloride total pressures. You said they were low by about 50 percent relative to the JANAF data.

<u>Response</u> (Bonnell): The current interpretation is that molecular beam collimating system is not particularly a restriction in the beam only. The beam that actually enters the mass spectrometer ion source is of the order of the size of the entrance of the mass spectrometer itself. This arrangement allows scattered carrier gas, in addition to beam carrier gas, to enter the ion source and give too high a reference gas signal. I would like to make the argument that 50 percent agreement is pretty good. I mean, that is quite typical of ordinary Knudsen cell work. This question is discussed more fully in the main text.

<u>Question</u> (Hildenbrand): Do you expect the same kind of disparity over other condensible species?

Response (Bonnell): Yes, as a matter of fact, in the sodium sulphate case, we apply that correction to the sodium partial pressure. We do not need to apply it to the sulphur dioxide or the oxygen.

Moderator (Greene): Did you do any diagnostics such as varying the orifice size in your study of sodium chloride monomer-dimer equilibrium?

Response (Bonnell): All right, varying orifice size is a little tricky. These are platinum cones and we take what we can get when we drill holes. We did use two totally different samplers with approximately 30 percent difference in orifice size and there seems to be no difference in the data.

We have changed the skimmer to orifice distance slightly. This is not something that is easily done. We are, in fact, depending upon measurements by a number of other people as to where the maximum expansion ratio occurs, which is typically like 120 nozzle diameters. So we haven't made a systematic change in orifice size. We are really not equipped with the pumping to do it yet. That is coming. (It should be noted that the nozzle-skimmer geometry is very similar to that used earlier for flame sampling and other 1 atm pressure studies as reported on by Hastie).

Comment (Hastie): I think the interesting thing about this work is represented by the figure where we show data over about an 800 degree temperature range for sodium chloride and about six orders of magnitude in pressure--that is, the data from the conical and the capillary sampler both fall on the same line (Clausius-Clapeyron relationship). The really striking thing was that we were able to get this kind of data with a capillary. We thought the capillary would be much cruder and we were originally interested in the capillary just because it would be a more robust type of sampling probe for very extreme environments. But it does seem to give pretty good thermodynamic data.
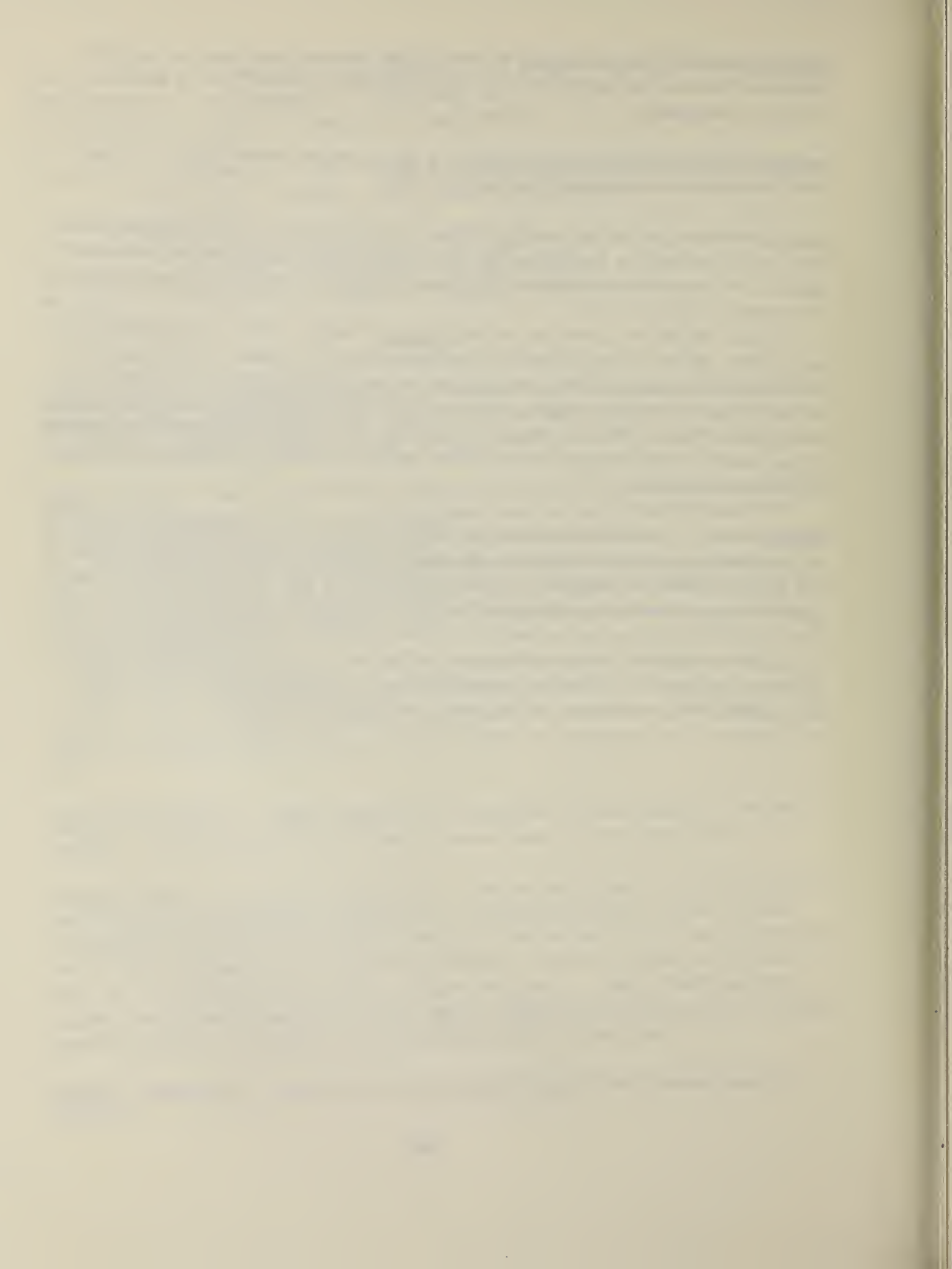
SLAG AND METAL OXIDE VAPORIZATION IN REACTIVE ATMOSPHERES

J. W. Hastie, D. W. Bonnell and E. R. Plante
Chemical Stability and Corrosion Division
Center for Materials Research
National Bureau of Standards
Washington, D. C.   20234

Abstract

Metal oxides, whether they are present in the form of refractory ceramics or slags, are key components of high temperature energy systems. Planned magnetohydrodynamic (MHD) and coal gasifier systems are particularly dependent on the thermochemical properties of ceramic and slag materials. However, almost no basic thermochemical data exist for oxides in the presence of high temperature-high pressure reactive gases such as H_2O. The present study utilizes a modification of the now classical Knudsen effusion mass spectrometric technique and a new technique, transpiration mass spectrometry, for molecular-level thermochemical analysis of MgO and a potassium enriched MHD coal slag in the presence of H_2O vapor and related gases. New data are presented for the enthalpy of formation of MgOH ($\Delta H_{f\ 298}$ = -35.8 ± 3.0 kcal/mol). Species partial pressures and derived activity coefficients are given for a potassium enriched Illinois number 6 coal slag over a range of K_2O content (15.4-8.0 mole%) and temperature (1100-1820 K). Data on the effect of H_2O vapor on alkali vapor transport are also given.

1.   Introduction

One of the key limitations to further technological improvement, or the new development, of fossil energy systems is the ability of ceramic components to withstand chemically corrosive environments at high temperature and pressure [1,2]. Alkali metal impurities in coal and some oil fired combustors are known to be particularly important in the degradation of alumino-silicate refractories, e.g., see Rigby and

Hutton [3], and Clews, et al. [4]. The thermodynamic activity of alkali metal species in coal minerals, slags and ceramics is therefore an important, but usually unknown, parameter in the design or performance evaluation of coal fired combustors or gasifiers.

Related to this problem is the interaction of gaseous species, particularly H_2O and H_2, with the alkali-containing systems and also with the ceramic components. These gases can greatly modify the vapor transport properties of alkali and other metal containing components by virtue of the formation of volatile oxide, hydroxide and posssibly hydrated vapor species. Numerous examples of such species have been cited elsewhere [5]. Recent citations pertinent to the present discussion include:

 • vapor transport of silica, possibly in the form of $Si(OH)_4$ species, under coal combustion conditions [6];

 • water enhanced vapor transport of Cr_2O_3 from chromite-based ceramics, possibly in the form of $CrO_2(OH)$ species [7,8];

 • water enhanced vapor transport of Na_2O from soda-lime-silica melts [9]; and

 • water enhanced vapor transport of MgO ceramics, possibly in the form of $Mg(OH)_2$ species [10].

These studies are based either on the classical transpiration (at $\sim$ one atm) or, in a relatively few instances, the Knudsen effusion mass spectrometric method (at $\sim 10^{-4}$ atm). Only in a very few cases is there any assurance of species identity and in each instance the conditions of pressure, temperature, and reactive gas composition differ greatly from those present in practical energy systems. These two basic experimental

limitations make it difficult, if not impossible, for one to accurately

interpret or predict, through the use of thermodynamic models, the

nature of ceramic-slag-gas interaction in fossil fueled energy systems.

A further complication in modeling such complex systems is the

possible presence of non-equilibrium or rate limiting processes.

Diffusion effects, for instance, can significantly reduce vaporization

rates from oxide solids [11] and melts [12].

The present study addresses these interrelated problems of species

identity, relation of experimental conditions to practice, and appli-

cability of thermodynamic equilibrium, through the use of a modified gas

inlet Knudsen effusion mass spectrometric method (KMS) and a novel

transpiration mass spectrometric technique (TMS). The systems of interest

include:

(a) $MgO(s) + H_2O$, H_2, O_2, and

(b) A K-seeded Illinois Number 6 coal slag derived from an

MHD test channel [13].

The first system has practical significance in open cycle coal fired MHD

systems, where the durability (i.e., enhanced volatility) of MgO com-

ponents in the presence of reactive gases at temperatures in excess of

2000 C is of concern. The importance of the second system relates to

the retention of potassium seed by slag. This seed loss may reduce

plasma conductivity and will also limit the recovery of seed which, for

economic feasibility, must exceed about 98 percent.

Previous transpiration vaporization studies, e.g., see Maeda et

al. [10], have indicated the probable formation of $Mg(OH)_2$ and $MgOH$ from

a reaction of $MgO(s)$ with H_2O or H_2. The JANAF thermochemical tables [14]

have estimated a value for the heat of formation of MgOH as no reliable experimental data are available for this species. No basic thermo-chemical data are available for potassium species vapor pressures and activities in MHD slag compositions.

2. Experimental

2.1 Apparatus and Procedure

2.1.1 Gas-Inlet Knudsen Effusion Mass Spectrometer System

The Knudsen effusion cell, furnace, and vacuum assembly used for the present study are similar to those described elsewhere [15] with the following exceptions. A Bendix[a] time of flight (TOF) mass spectrometer was used as the beam analyzer and the vacuum system consisted of a differentially pumped configuration using mercury diffusion pumps. The Knudsen cell was modified by insertion of a gas inlet tube through the cell base. A mechanical chopper was used for beam modulation to distinguish between beam and scattered gaseous species in the ion source of the mass spectrometer. The TOF instrument was modified to operate in a continuous mode giving significantly increased sensitivity.

Knudsen Cells

An iridium Knudsen cell, with dimensions 1.6 cm length, 0.95 cm O.D., 0.076 cm lid thickness, and 0.1 cm orifice diameter, was used for the MgO experiments. Gas injection was carried out through an iridium reentrant tube 15 cm long, 0.43 cm O.D., which was welded into the Knudsen cell bottom such that the internal portion extended 0.64 cm into the cell cavity. Gas injection to the Knudsen cell occurred through two holes, 0.025 cm diameter, located in the side of the reentrant tube and

---

[a] Certain commercial items are identified only for completeness and this does not imply that they are the most suitable available instrumentation.

at right angles to the cell orifice. The entire cell was weld-sealed to prevent leakage. Samples were loaded through the effusion orifice. Cell heating was achieved by radiation from a tungsten resistance heater 5 cm long and 1.6 cm diameter.

For the slag vaporization studies weld-sealed platinum Knudsen cells, having orifice diameters of about 0.025 cm, were used.

Temperatures were obtained from optical pyrometer sightings of the cell orifice made through a prism, vacuum chamber window, the ion source, the chopping wheel and an adjustable aperture separating the mass spectrometer and Knudsen cell chambers. A correction of 4.38 x 10^{-5} deg^{-1} was used with the apparent absolute temperature, to correct to the IPTS-68 temperature scale.

Partial Pressure Determination

Conversion of mass spectral ion intensities to species partial pressures was made through the basic relations

$$P_i = k_i I_i^+ T \tag{1}$$

$$k_i = \frac{GA_i (2\pi R)^{1/2} \Sigma m_i}{ac\sqrt{M_i} \Sigma I_i^+ t\sqrt{T}} , \tag{2}$$

where

P_i is the species partial pressure

I_i^+ the corresponding ion intensity

T temperature

k_i instrument and system sensitivity

G gravimetric factor

Σm_i weight loss

t time

c   clausing factor

a   orifice area and

M_i the molecular weight of species i (or an average value

        for Knudsen effusion),

as described elsewhere [15]. In some cases, k_i for different species,
but arising from the same experimental configuration, can be inter-
related through known ionization cross sections, σ_i, and transmission/
detector efficiencies, S_i i.e.,

$$k_i \propto (\sigma_i \cdot S_i \cdot A_i)^{-1} \qquad (3)$$

where A_i is an isotope abundance factor (see Bonnell and Hastie [16]).
These basic parameters are summarized in table 1. The degree of agree-
ment for the k_i's obtained from weight loss [expression (2)] or cross
section data [expression (3)] provides a useful check on the internal
consistency of the partial pressure data.

2.1.2 Transpiration Mass Spectrometric System

The transpiration mass spectrometric system (TMS) has been described
in detail elsewhere [16], and the basic apparatus is shown schematically
in figure 1. Sample transpiration and molecular beam production are
carried out in chamber I, while beam modulation and mass spectral
analysis are achieved in chamber II. In the present study a capillary-
type sampler of proven sampling fidelity [16] was used.

Relation (1) can also be applied to TMS data. The sensitivity
factors k_i are obtained by several independent methods, thereby providing
a good test of internal consistency in the data. The basic relationships
are:

$$k_i = R \frac{n}{V} \Delta t / \Sigma I \Delta t \tag{4}$$

and

$$k_i = k_j \left(\frac{\sigma_j}{\sigma_i}\right) \left(\frac{S_j}{S_i}\right) \left(\frac{1}{\bar{S}}\right) \tag{5}$$

where

R   is the gas constant

n   number of moles transported

V   volume of gas transported

Δt transport time

I   species ion intensity (corrected for isotope abundances)

σ species ionization cross section

S   beam expansion and quadrupole mass discrimination factor, and

$\bar{S}$ an instrument gas scattering correction ($\sim$ 0.6, [16]).

The reference or transport gas sensitivity factor k_j is obtained from
·equation (1) since the pressure of transport gas is known from an
external manometric determination. Table 1 summarizes the ionization
cross sections and sensitivity factors used to obtain partial pressures
from ion intensity data.

2.2 Results

2.2.1 KMS Data for MgO + H_2 System

MgO vaporizes primarily as Mg and O_2 species under free vapori-
zation conditions. From the JANAF thermochemical data [14], we can
expect H_2 or H_2O to enhance the vaporization of MgO by the formation of
volatile hydroxides such as MgOH and $Mg(OH)_2$. However, the extent of
this interaction is uncertain by at least an order of magnitude owing to
the estimated nature of the thermochemical data for MgOH [14]. In the
present study, the reactions:

$$MgO(s) = Mg + 1/2 \ O_2 \tag{1}$$

$$H_2O = H_2 + 1/2 \ O_2 \tag{2}$$

$$Mg + 1/2 \ H_2O + 1/4 \ O_2 = MgOH \tag{3}$$

were monitored, virtually simultaneously, by the KMS technique as a function of temperature and pressure using the ion intensities of Mg^+, $MgOH^+$, H_2O^+, O_2^+ and H_2^+.

Species Production and Identification

In order to enhance the production of MgOH, molecular H_2 was used as the reagent gas rather than H_2O which would favor $Mg(OH)_2$ formation. This served as a convenient source of H_2O while keeping O_2 at a reduced level [via reaction (2)] and maintaining a high level of Mg [through reaction (1)]. A simultaneous formation of $Mg(OH)_2$ and MgOH was considered undesirable as the $(MgOH)^+$ ion could not be assigned unambiguously to a single molecular precursor. In the present experiments, with excess H_2 present, $Mg(OH)_2^+$ was below the mass spectral detection limit of $\sim 10^{-10}$ atm. The MgO species was also undetectable. An observed 40 amu ion was attributable, from isotope arguments, to a Ca impurity. In the absence of added H_2 no modulated ion signals were detected at 41 amu.

Identification of the 41 amu ion, in the presence of H_2, as $MgOH^+$ (with precursor MgOH) was verified by its intensity dependence on the square root of the H_2^+ intensity for isothermal conditions. This is consistent with the reaction:

$$MgO(s) + 1/2\ H_2 = MgOH \qquad . \qquad\qquad (4)$$
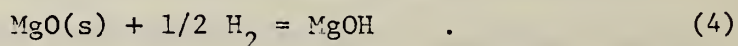
Calibration and Pressure Determination

Conversion of ion intensitites to partial pressures for each species was made as follows. In the absence of H_2, the Mg^+ ion intensity can be related to the known partial pressure of Mg over MgO(s) [14] by relationship (1), yielding a value of the sensitivity factor k_{Mg} for each data point. Then, from relation (3),

$$k_{Mg} = k_g / \sigma_{Mg} \cdot S_{Mg} \cdot A_{Mg}$$

and the geometrical calibration factor k_g can be used to obtain k_i for the other species present, also from a relation of the type (3).

An independent test of the calibration procedure was provided by conversion of observed O_2^+ and O^+ (at low eV) ion intensities to partial pressures and equilibrium constants for the reaction:

$$O_2 = 2 \, O \qquad . \qquad (5)$$

The equilibrium constants, obtained under neutral and reducing conditions (H_2 present), and at various temperatures, agreed with JANAF [14] to within a factor of two.

Mass Action Test for Equilibrium

As a further test of data consistency and, more particularly, the establishment of thermodynamic equilibrium, an attempt was made to measure the equilibrium constant, K_p, for reaction (2). At constant temperature, $K_p(2)$ should be invariant with H_2^+ ion intensity (i.e., partial pressure) for an equilibrium process. Typical data are given in figure 2. Note that the K_p's are essentially invariant with H_2^+ ion intensity but that the absolute magnitude is about a factor of 30 less than the literature value [14]. This low $K_p(2)$ value suggests P_{H_2} is too low as P_{O_2} was verified through reaction (5) and it is unlikely that H_2O, as a reaction product, could be produced in excess of the equilibrium amount. We believe that the low intensity H_2^+ signals resulted from a known discrimination effect of the TOF ion source magnet on light masses such as H_2^+. Hence the JANAF values of $K_p(2)$ were used to calibrate for this discrimination effect in the derivation of k_{H_2}. This correction was not necessary, however, to the measurement of MgOH equilibria as use of reaction (3) eliminates explicit consideration of H_2 partial pressures.

Thermodynamic Data for MgOH Production

The temperature dependence of $K_p(3)$ is shown in figure 3. A representative example of data used for the calculation of $K_p(3)$ is given in table 2. Table 3 summarizes the partial pressure, equilibrium constant and third law enthalpy data for reaction (3). The Gibbs (free energy) function data used for the enthalpy calculations were obtained from JANAF [14] and should be reliable in view of the simple electronic and geometric structure for MgOH.

Evidence in support of reaction (3) being at equilibrium is provided by the invariance, within experimental uncertainty, of $K_p(3)$ with P_{H_2O}, e.g., see the 2054 K data points in table 3.

JANAF's most recent estimate of the standard heat of formation of MgOH, based on bond energy considerations, is -39.38 ± 9 kcal/mol. The average heat of reaction (3) of -42.2 kcal at 298 K can be combined with the heat of sublimation of Mg(s) ($+35.3$ kcal/mol) and one half the heat of formation of H_2O (-28.9 kcal/mol) to yield a standard enthalpy of formation for MgOH of $\Delta H_{f\ 298}$ MgOH = -35.8 ± 3 kcal/mol. The error limit arises from an estimated factor of two uncertainty in the cross sections used to convert ion intensities to partial pressures. From the data listed in table 3 and figure 3, a second law evaluation gives

$$\Delta H_{298}(3) = -52.4 \pm 10 \text{ kcal/mol,}$$

which is equivalent to

$$\Delta H_{f\ 298} \text{ MgOH} = -46.0 \pm 10 \text{ kcal/mol.}$$

The uncertainty is based on two standard errors in the second law enthalpy. Agreement between the second and third law values of $\Delta H_{298}(3)$ is satisfactory considering the limited experimental temperature range (e.g., see figure 3).

2.2.2 TMS and KMS Data for MHD slag K_1

A detailed study was made of vapor transport over a high melting

temperature (~ 1700 K) potassium-enriched coal slag (Illinois No. 6).

The initial slag composition, in wt%, ·was: Al_2O_3 (12.06), CaO (3.8),

Cr_2O_3 (1.3), Fe_2O_3 (14.25), K_2O (19.54), MgO (1.03), Na_2O (0.47), SO_3

(0.21), SiO_2 (46.82), TiO_2 (0.52). This slag sample was obtained from

combustion of Illinois No. 6 coal with additional potassium added to the

combustor [13]. For identification purposes we shall denote this high

potassium-content slag as K_1. X-ray diffraction data indicated that the

bulk of the potassium in the slag is present as the compound $KAlSiO_4$.

TMS analysis indicated that about two percent of the potassium was

present in relatively volatile form, mainly K_2SO_4 and K_2CO_3.

We present here data on vapor species identity and vapor transport

dependence on temperature, N_2 carrier gas pressure, H_2O pressure, and

slag K_2O content. The results are interpreted to indicate that the bulk

of the potassium is highly bound in the slag and that its release to the

vapor phase may, in some instances (particularly at reduced temperature),

be controlled by the rate of alkali diffusion to the surface.

Identity of Volatile Species

The as-received potassium-enriched coal slag was subjected to a

series of heating cycles (runs) in nitrogen carrier gas. During the

initial heating cycle mass spectral scans, obtained using the TMS

technique, revealed many volatile species, in addition to the expected K

and Na species. A typical mass spectrum is given in figure 4 where the

following species can be positively assigned: H_2O, CO_2, SO_2, O_2, K,

and Na. Some of the other ion signals can be tentatively assigned to

the species (some hypothetical): KO or KOH, KS or KSH, SiS, SiSH, H_2S,

H_2SO_2, and KSiO. From JANAF [14], we can expect to see KOH under these conditions but not H_2S. Some of these more minor species may result from slag occlusions and would not represent an equilibrium release from the slag. Following this initial heating cycle, the only significant slag vapor species were K and O_2.

Initial Species Partial Pressure--Temperature Dependence

The initial volatiles showed a non-monotonic variation of partial pressure with temperature, as shown in figure 5. These volatiles constitute only a few percent of the total slag components and are not representative of the bulk slag composition. However, they do provide a sufficiently high flux of alkali (Na, K) and SO_2 to be a potential source of corrosion. The high initial partial pressures of SO_2, CO_2, K, and Na are indicative of the presence of alkali sulfate and carbonate in the slag. An additional contribution to low temperature alkali release could result from the high H_2O content leading to the formation of volatile hydroxide species (KOH) at T < 1250 K. Note that the T > 1400 K the K pressures fall below those expected from $KAlO_2$, but that the SO_2, CO_2, and H_2O pressures are still relatively high. Apparently, at this stage, the K produced by sulfate and carbonate decomposition is retained in the bulk slag. After further heating at 1620 K for about 30 min., the sample was virtually depleted of Na, SO_2, and CO_2; H_2O also continued to fall off in pressure to a negligible level.

Potassium Partial Pressure--Temperature Dependence

The variation of K-partial pressure was followed over a wide temperature range ($\sim$ 1150-1820 K) using both the TMS and KMS techniques. Usually, the O_2 partial pressure tracked with the K data (but not always in stoichiometric proportion) indicating the main vaporization process

to be:

$$K_2O(\text{slag}) = 2K + 1/2 \ O_2 \quad , \tag{6}$$
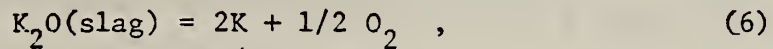
with possible secondary contributions, as discussed later. At temper-
atures corresponding to K partial pressures of 10^{-5} atm, or less, the
rate of loss of K_2O from the bulk was sufficiently low that the data
represent constant composition conditions. At higher temperatures, and
vaporization rates, the data are greatly modified by the effects of
changing slag composition.

Representative vaporization data are given in figure 6. For a
typical TMS data point, at 1466 K, P_{N_2} = 0.64 atm, $I_{N_2}^{29}$ = 3.2 x 10^4 μV,
I_K^{39} = 200 μV, yielding P_K = 7.0 x 10^{-6} atm. In order to obtain accurate
data at K-partial pressures below 10^{-5} atm, use was made of Knudsen
effusion mass spectrometry (KMS). The KMS system used for these slag
measurements differed from that used for the MgO studies in that no gas
inlet was used and a quadrupole mass filter was substituted for the TOF
analyzer. A relatively high background signal at 39 amu (K^+ position)
limited the sensitivity of the TMS measurements. By combining data from
both the TMS and KMS methods we were able to cover a wide range of
temperature and K_2O mole fraction. The rate of vapor transport differs
appreciably for the two methods, with KMS losing about three times as
much material as for TMS at equal K pressure. Thus the bulk slag com-
position changes more rapidly during a KMS experiment.

The N_2 carrier gas used for the TMS experiments also contained a
small, but significant, amount of O_2 (typically $\sim$ 5 x 10^{-5} atm). This
caused a suppression of the K-vapor pressure by a reversal of reaction
(6). When this effect is taken into account, using the observed thermo-
chemical data for reaction (6), good agreement is found between the TMS

and KMS data, e.g., see the comparison temperature (1561 K) and com-
position point in figure 6. That such an agreement is possible is a
strong indication of thermodynamic equilibrium, at least with respect to
K transport, as species residence times in Knudsen cells and trans-
piration tubes differ appreciably.

Several processes appear to be contributing to the relatively
shallow slopes of the curves presented in figure 6, which under equilib-
rium conditions represent enthalpies of vaporization. During run 1
(KMS) the ratio of O_2 to K varied from being much lower than allowed by
reaction (6) at low temperatures to somewhat larger at higher temper-
atures. Also, during the low temperature phase of this run, release of
K_2SO_4 and K_2CO_3 was still occurring. Each of these factors can lead to
higher than expected K-pressures at low temperatures and hence a low
apparent vaporization enthalpy.

K_2O Activity Coefficients

As most of the bulk-slag composition changes result from reaction
(1), a continuous monitoring of the K-partial pressure (and O_2) allows
one to calculate the slag composition at any stage of an experiment.
For instance, with the TMS method, the number of moles (n) of K_2O lost
by vapor transport (as $K + O_2$) is related to the known mole number and
pressure of N_2 by the transpiration relationship:

$$n(K_2O) = \frac{[n(N_2) + n(K_2O)] \, P_{K_2O}}{P_{N_2}} \quad .$$

Hence the change in composition with time can be determined, provided the initial sample weight and composition are known. Likewise, with the KMS method, the Knudsen effusion equation [see relations (1) and (2)] may be used to follow the bulk-slag composition. For both the TMS and KMS methods, the basic experimental requirement for monitoring the bulk composition is the measurement of significant species partial pressures as a function of time during an experimental run. An independent check on this approach can be provided by chemical analysis of the sample remaining at the end of a run. Such an analysis has not yet been performed on the post run slag samples. However, when all the significant species are measured, and the ionization cross sections are known, the in situ approach to monitoring composition changes provides a good mass balance at any stage of the experiment, as was shown for the NaCl and Na_2SO_4 test systems reported elsewhere [16].

Since the mole fraction of K_2O can be defined at any stage of an experiment, it is possible to convert K-partial pressures to K_2O activity coefficients. By varying the amount of K_2O present in the slag during a vaporization run we were able to follow the dependence of the K_2O "apparent" thermodynamic activity on temperature and composition. The term "apparent" is used to emphasize that the slag system may not always be in a state of complete thermodynamic equilibrium.

Typical data, expressed in activity coefficient form, are given in figure 7. Activity coefficients ("apparent") were calculated from the experimental K-partial pressures using the expression:

$$\gamma(K_2O) = \frac{P_K^2 \left(\frac{P_K}{4}\right)^{1/2} [slag]}{P_K^2 \left(\frac{P_K}{4}\right)^{1/2} [pure\ K_2O\ reference]\ X(K_2O)}$$

where $X(K_2O)$ is the slag K_2O mole fraction, determined from the calcu-
lated mass loss using the integrated ion intensity-time method. The K_2O
reference state data were obtained from the literature. This expression
assumes congruent vaporization according to reaction (6). That this is
the appropriate reaction was confirmed by KMS observations of O_2 in the
appropriate ratio to K, to a reasonable approximation. As was indicated
in figure 6, the corresponding TMS data for $\gamma(K_2O)$ need to explicitly
include the O_2 partial pressure as it was considerably higher than the
dissociation pressure of K_2O. When this is done the TMS $\gamma(K_2O)$ data
agree satisfactorily with the KMS $\gamma(K_2O)$ values, where comparison
temperatures and compositions are available. The largest experimental
uncertainty in comparing activity coefficient data sets from the two
different techniques (KMS and TMS) is the accuracy of $X(K_2O)$ which is
probably uncertain by ten percent in each case.

Note in figure 7, the non-monotonic nature of the log $\gamma(K_2O)$ vs T^{-1}
curves. For normal non-ideal solution behavior, we would expect a
linear monotonic relationship with a negative slope representing a
negative partial molar enthalpy of solution for K_2O in the slag. This
type of behavior occurs for segments of each run (see figure 7), e.g.,
for run 1, up to about 1430 K, and for run 2 between 1430 and 1630 K.
The run 1 data were obtained during the initial heating period when
K_2SO_4 and K_2CO_3 decomposition was a significant source of K. The rapid
reduction in $\gamma(K_2O)$ as the temperature is increased beyond 1430 K results
from the almost complete depletion of these relatively volatile forms of
potassium. For runs 2 and 3, the initial reduction of $\gamma(K_2O)$ with
increasing temperature is believed to be due either to diffusion limited
(in solid slag) K-transport to the slag surface or to changes in the

mode of O_2 release from the slag, for instance through Fe_3O_4 disso-
ciation. The onset of increasing $\gamma(K_2O)$ with temperature is believed to
arise from an as yet unspecified physiochemical change in the slag
leading to a less viscous form, thereby reducing the diffusion limita-
tion, or, again, to secondary sources of O_2. At higher temperatures the
bulk composition changes rapidly (see mole fractions in figure 7) and
leads to a peaking in $\gamma(K_2O)$. We believe that the data for runs 2 and
3, at temperatures in excess of 1450 K, represent an equilibrium vapor-
ization condition, particularly as the KMS and TMS data are in agreement
for these conditions. Clearly, these unusual trends in the $\gamma(K_2O)$ data
indicate the difficulty involved in making a priori predictions of slag
vaporization behavior.

K_1 slag + H_2O System

The effect of added H_2O on the release of alkali from the K_1 slag
to the gas phase was monitored with the transpiration mass spectrometer
from 1553-1692 K and 10^{-3}-10^{-1} atm H_2O vapor in ~ 0.5 atm N_2. Typical
data are given in figures 8 and 9. Note in figure 8 the relatively
small dependence of K-pressure on temperature at a constant H_2O pres-
sure. However, as is shown in figure 9, at constant temperature, the K-
pressure is strongly dependent on the H_2O-pressure. The following
reactions are possible:

$$K_2O \; (\ell) \; (\text{in slag}) + H_2O = 2KOH \tag{7}$$

$$K_2O \; (\ell) \; (\text{in slag}) + H_2 = 2K + H_2O \tag{8}$$

$$H_2O = H_2 + 1/2 \; O_2. \tag{9}$$
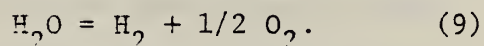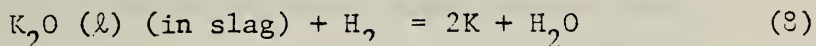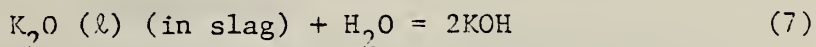
As no KOH was observed for these particular conditions, reaction (7)
does not appear to be significant. From the instrumental detection
limit for KOH^+, the species KOH is estimated to be at least an order of

magnitude less abundant than K. We believe, therefore, that reaction (8) is the predominant mechanism for H_2O-induced alkali release under the conditions pertaining to figure 9 and that the thermal dissociation of water [reaction (7)] provides the necessary H_2. However, as is shown in figure 9, the reactions do not appear to have attained equilibrium.

Future experiments with added H_2 gas are planned to test this interpretation.

3. Summary

In the presence of H_2, MgO vaporizes primarily as MgOH, Mg and O_2. From the measured equilibrium between these species (and H_2O) a value of $\Delta H_{f\ 298}$ MgOH = -35.8±3 kcal/mol was determined.

A detailed study has been made of vapor transport over a high melting temperature ($\sim$ 1700 K) potassium-enriched slag derived from Illinois Number 6 coal. The rate of release of K, and secondary species such as H_2O, O_2, SO_2, CO_2, and Na, has been measured over the temperature range 1100-1820 K, a N_2-pressure range of 0.2-0.63 atm, and for K_2O slag contents over the range 15.4-8.0 mole%. Apparent activity coefficients for K_2O in the range of 10^{-9}-10^{-7} were determined for this regime of temperature and composition. In the presence of H_2O the rate of K-release increased but apparently not to the equilibrium level.

Acknowledgment

Table 1

Ionization Cross Sections (σ) and Sensitivity (S) Factors

	KMS		TMS[c]	
	σ_i [a]	S_i [b]	σ_i	S_i
N_2	--	--	1.48	1.0
O_2	2.62	0.177	1.26	1.3
H_2O	1.78	0.236	1.5	0.8
Mg	3.44	0.204	--	--
MgOH	4.98	0.156	--	--
K	--[e]	--	7.8[d]	1.3
Na	--	--	4.5[d]	1.0

[a] Cross section for Mg given by J. B. Mann, J. Chem. Phys. 46, 1646 (1967). Values for H_2O, O_2 and MgOH estimated with 30 percent uncertainty.

[b] Based on the empirical dependence of multiplier efficiency on particle mass; relative data only.

[c] σ_i and S_i values measured directly as described elsewhere [16].

[d] Experimental data cited by L. J. Kieffer and G. H. Dunn [Rev. Mod. Phys. 38, 1 (1966)].

[e] KMS partial pressure data for K and O_2 obtained via relationships (1) and (2), i.e., no σ, S data were necessary.

Table 2

Typical Reaction (3) Data at 2029 K

Ion	A_i	k_i[a]	$I^+ \cdot T (\mu V \cdot K)$	P_i (atm)
Mg^+	0.78	3.16 – 12[b]	2.19 + 6	6.92 – 6
O_2^+	1.0	3.73 – 12	2.86 + 5	1.07 – 6
H_2O^+	1.0	4.05 – 12	4.02 + 5	1.63 – 6
$MgOH^+$	0.78	2.85 – 12	1.58 + 3	4.50 – 9

[a]Values of σ_i and S_i used to derive k_i are given in table 1.

[b]Denotes e.g., 3.16×10^{-12} atm/μV K (10^7 Ω).

Table 3

Thermodynamic Data for Reaction (3)

Temp.	P_{Mg}	P_{H_2O}	P_{O_2}	P_{MgOH}	K_P	ΔH°_{298} [a]
K	atm	atm	atm	atm		cal
2077	1.48-5	7.56-6	7.42-7	1.35-8	11.3	-42306
2077	1.66-5	1.01-5	4.84-7	1.53-8	11.0	-42195
2022	6.10-6	1.47-6	9.73-7	3.34± [	14.4	-42194
2022	5.14-6	2.64-7	1.19-6	1.09- [	12.5	-41625
2029	6.92-6	1.63-6	1.07-6	4.50-9	15.8	-42710
2054	9.73-6	1.47-6	1.75-6	6.16- [	14.4	-42841
2054	1.32-5	6.16-6	1.10-6	1.44-8	13.6	-42608
2054	1.81-5	1.10-5	7.12-7	2.40-8	13.8	-42668
2054	2.99-5	2.00-5	3.84-7	4.10-8	12.3	-42198
2054	2.79-5	2.17-5	2.60-7	3.62-8	12.3	-42198
2107	2.26-5	3.72-6	4.18-6	1.72-8	8.73	-41817
2107	2.95-5	1.34-5	2.77-6	4.75-8	10.8	-42708
2098	3.07-5	1.76-5	1.78-6	4.08-8	8.67	-41615
2167	5.33-5	1.77-5	7.74-6	7.43-8	6.28	-41550
2167	5.98-5	3.39-5	5.96-6	1.09-7	6.34	-41591
				AVERAGE		-42188

[a] Obtained from the expression:

$$\Delta H^{\circ}_{298} = T \left\{ \sum_{p-r} [- (G^{\circ}_T - H^{\circ}_{298})/T - R\ln K_P] \right\} \, ,$$

where the summation refers to the difference between product (p) and reactant (r) thermodynamic functions.

References

1. Raymon, N. S. and Sadler, III, L. Y., "Refractory Lining Materials for Coal Gasifiers", Information Circular 8721 pp. 1-22 (1976).

2. Crowley, M. S., "Refractory Problems in Coal Gasification Reactors", Amer. Ceram. Soc. Bull., 54, 1072 (1975).

3. Rigby, G. R. and Hutton, R., "Action of Alkali and Alkali-Vanadium Oxide Slags on Alumina-Silica Refractories", J. Amer. Ceram. Soc. 45, 68 (1962).

4. Clews, F. R., Richardson, H. M., and Green, A. T., "The Action of Alkalies on Refractory Materials: Part V. Further Observations on the Action of Potassium Chloride Vapor on Refractory Materials at 1,000 °C", Trans. British Ceramic Society 39, 139 (1940).

5. Hastie, J. W., "High Temperature Vapors: Science and Technology", Academic Press, New York (1975).

6. Taylor, R. W., "Silica Vaporization and Condensation: A Potential Source of Fouling in Coal Combustion", ANL-77-21, pp. 260-264 (1977).

7. Kessler, W., Jantsch, W., Gebhardt, F., and Majdic, A., "Investigations of Volatilization in the System Cr_2O_3 and $SiO_2-Al_2O_3-ZrO_2$", Glastechn. Ber. 51, 289 (1978).

8. Kim, Y. W. and Belton, G. R., "Thermodynamics of Volatilization of Chromic Oxide. I. Species Chromium Trioxide and Chromium Dioxy Hydroxide", Met. Trans. 5, 1811 (1974).

9. Sanders, D. M. and Schaefer, H. A., "Reactive Vaporization of Soda-Lime Silica Glass Melts", J. Amer. Ceram. Soc. 59, 96 (1976).

10. Maeda, E., "Vaporization from Magnesia in O_2-H_2O Atmosphere", Yogyo Kyokai-Shi 86, 491 (1978).

11. Popkov, O. S. and Semenov, G. A., "Mass-Spectrometric Study of the Vaporization of Lithium and Sodium Aluminates", Russian J. Phys. Chem. 45, 266 (1971).

12. Cable, M. and Chaudhry, M. A., "Volatilization from Soda-Lime-Silica Melts at One Atmosphere and Reduced Pressures", Glass Technol. 16, 125 (1975).

13. Coal slag obtained from diffuser section of an MHD test channel at University of Tennessee Space Institute, Tullahoma, Tenn.

14. JANAF Thermochemical Tables, 2nd ed., NSRDS-NBS-37, U. S. Govt. Printing Office, Washington, D. C. (1971) and continuing supplements.

15. Plante, E. R., "Vapor Pressure Measurements of Potassium over K_2O-SiO_2 Solutions by a Knudsen Effusion Mass Spectrometric Method", p. 265 in Characterization of High Temperature Vapors and Gases, J. W. Hastie, Ed., NBS SP-561, U. S. Govt Printing Office (1979).

16. Bonnell, D. and Hastie, J. W., "Transpiration Mass Spectrometry", p. 357 in Characterization of High Temperature Vapors and Gases, J. W. Hastie, Ed., NBS SP-561, U. S. Govt. Printing Office (1979).

1. Schematic of transpiration mass spectrometer system.

2. Mass action test for equilibrium in the system $H_2O = H_2 + 1/2\ O_2$ present over MgO(s) at 2050 K. Data obtained at 20 eV ionizing electron energy. Dashed line obtained from JANAF [14].

3. Variation of equilibrium constant K_p with temperature for the reaction $Mg + 1/2\ H_2O + 1/4\ O_2 = MgOH$. Data obtained at 20 eV ionizing electron energy. Solid curve through the data points was obtained from the <u>third law</u> method of analysis. Dashed curves obtained from JANAF [14] estimates of $\Delta H_f MgOH$. The ΔH values are enthalpies, in kcal/mol, for the above reaction.

4. Typical mass spectrum (30 eV electron energy) of species evolved from a K-enriched Illinois Number 6 coal slag, K_1, (see text for composition) during an initial heating phase at 1428 K (run 1). Data were obtained using the TMS method with a capillary sampling probe. About one gm of sample was used with a N_2 transport gas pressure of 0.5 atm and a flow rate of $\sim$ 25 SCCM. The ordinate (right hand side) indicates approximate partial pressures, P_i, obtained from $P_i = k_{N_2} I_i T$, where I_i is species i signal intensity and k_{N_2} is the instrument sensitivity constant for N_2; $I_{N_2}^{29} = $ 170 mV.

5. Ion intensity and partial pressure variation of initial volatiles (K_2O wt% 19.5-19.1) as a function of temperature for the K_1 slag (m.pt. $\sim$ 1700 $\pm$ 30K) using the TMS approach (run 1). Conditions 0.5 atm N_2, capillary probe. Pressures, P_i, were obtained from the ion intensities I_i using the relation $P_i = k_i I_i T$, where k_i is obtained from k_{N_2} and the appropriate cross section and sensitivity factors.

The multiplying factors for K and Na refer only to the pressure

scale, i.e., K x 2.6 = pressure K. Literature Clausius Clapeyron

curves for K-pressures from $K_2CO_3(l)$ [14] and $KAlO_2(s)$ are also

shown for comparison. No literature data are available for $KAlSiO_4$,

the main K-containing constituent in this slag, and the $KAlO_2$ data

are considered as an upper limit to the vaporization rate for the

silicate: E. R. Plante, C. D. Olson and T. Negas, Sixth Intl.

Conf. on Magnetohydrodynamic Electrical Power Generation, Washington,

D. C., June, 1975, II, 211.

6.   Variation of K-partial pressure with temperature for K_2O contents

of 19.1-17.8 wt% (run 1--open circles, KMS), 18.17-18.07 wt% (run

2--open squares, TMS) and 18.07-18.0 (run 3, open squares, TMS).

Corresponding pressure curves (literature data) for the phases

$K_2CO_3(l)$, $K_2SO_4(l)$, $KAlO_2(s)$, and $K_2O \cdot 9Al_2O_3$--$Al_2O_3(s)$ are given

for comparison (see Plante et al., Fig. 5 caption). The triangular

point at 1561 K is a TMS data point corrected for the presence of

O_2 (see main text). Each curve represents a separate experimental

run. Usually, data were obtained for successive increases in

temperature, except for run 3--TMS where the arrows indicate the

run chronology, i.e, T increasing or decreasing. TMS conditions,

0.5 atm N_2, capillary probe.

7.   KMS data for variation of K_2O activity coefficient, $\gamma(K_2O)$, with

temperature and composition for the K_1 slag. The numbers, ranging

from 0.154 to 0.08, refer to the mole fraction of K_2O remaining in

the sample at each measurement point. For comparison with compositions

listed in Fig. 6, $X_{K_2O} = -0.0041 + 0.827 w + 0.0136 w^2$ where X is

mole fraction and w is weight fraction. Runs 1-3 were carried out

consecutively on the same sample. K_2O reference state data obtained from [14] and F. Natola and Ph. Touzain, Can. J. Chem., 48, 1955 (1970); to a good approximation the standard state data are given by the expression:

$$\log\left(P_K^{\ 2} \cdot P_{O_2}^{\ 1/2}\right) = -\frac{23751}{T} + 11.7723.$$

8. Dependence of K-pressure (log-scale) on temperature in the presence of H_2O ($\sim 3 \times 10^{-2}$ atm) and N_2 (0.5 atm) for the K_1 slag. Conditions, TMS method, capillary probe.

9. Dependence of K-pressure (log-scale) on H_2O content in N_2 (0.35 atm) at 1673K for the K_1 slag. Conditions, TMS method, capillary probe. The dashed curve of slope 0.5 represents the theoretical thermodynamic equilibrium dependence for reaction (8) (see text).
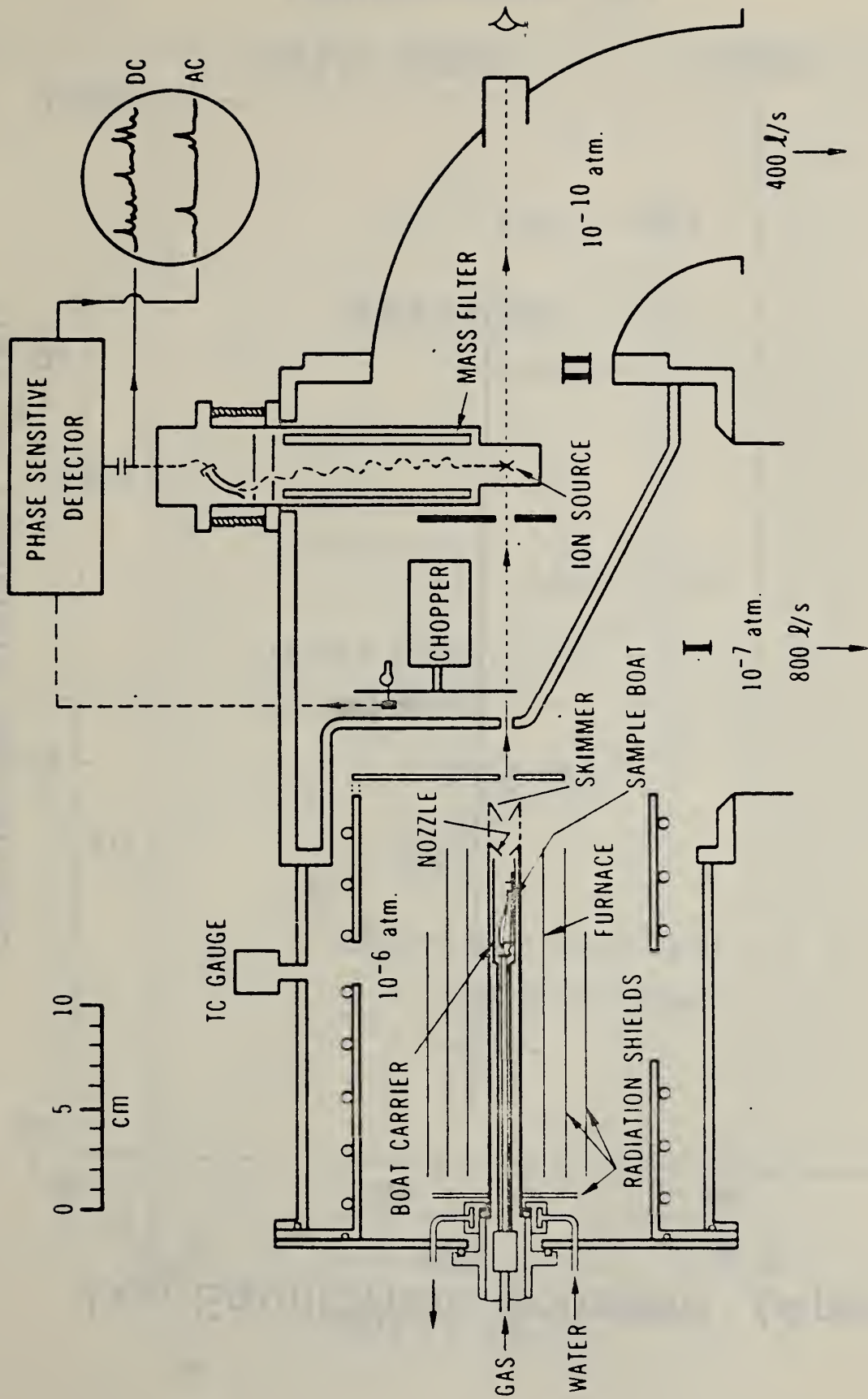
Figure 1
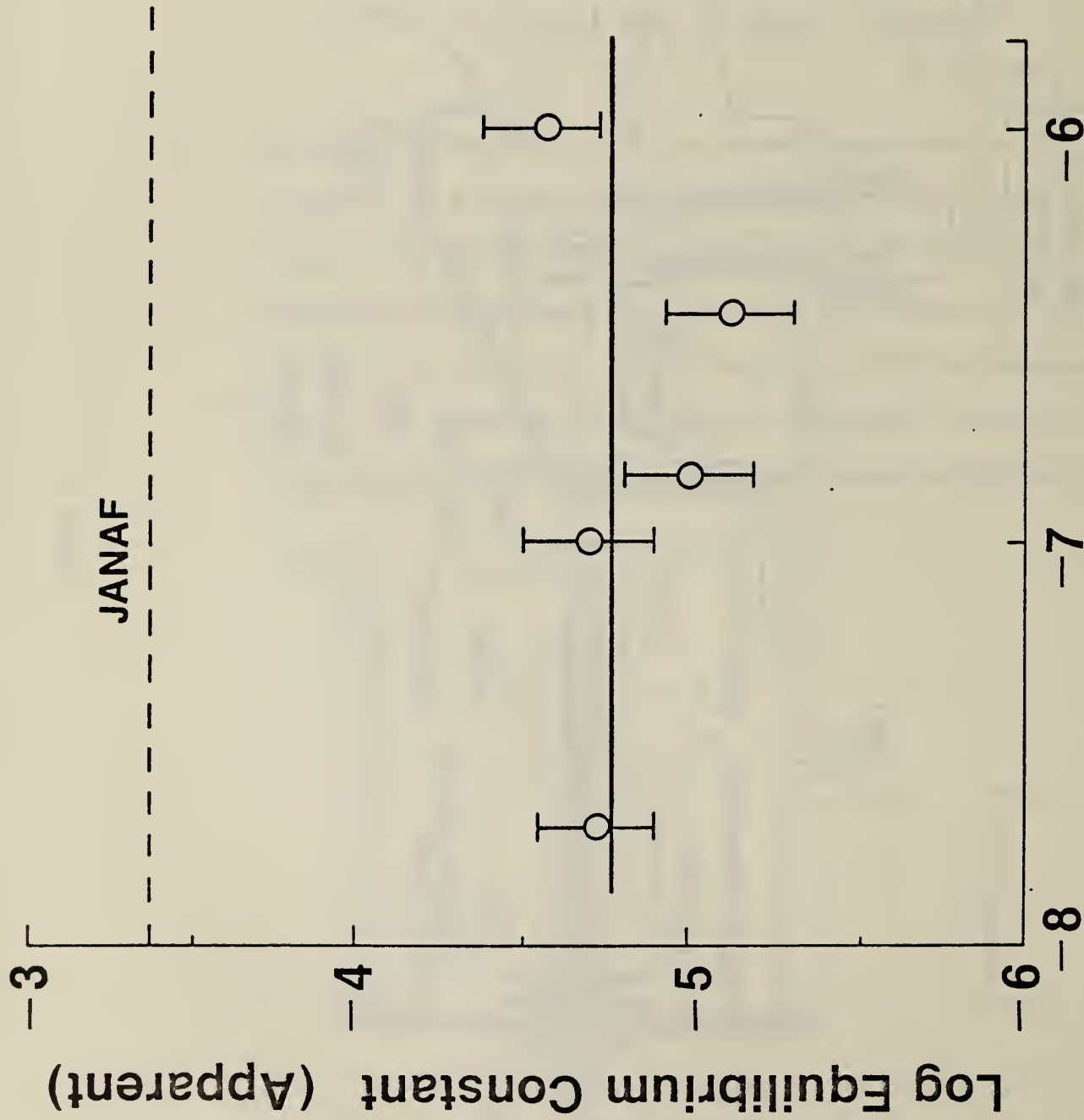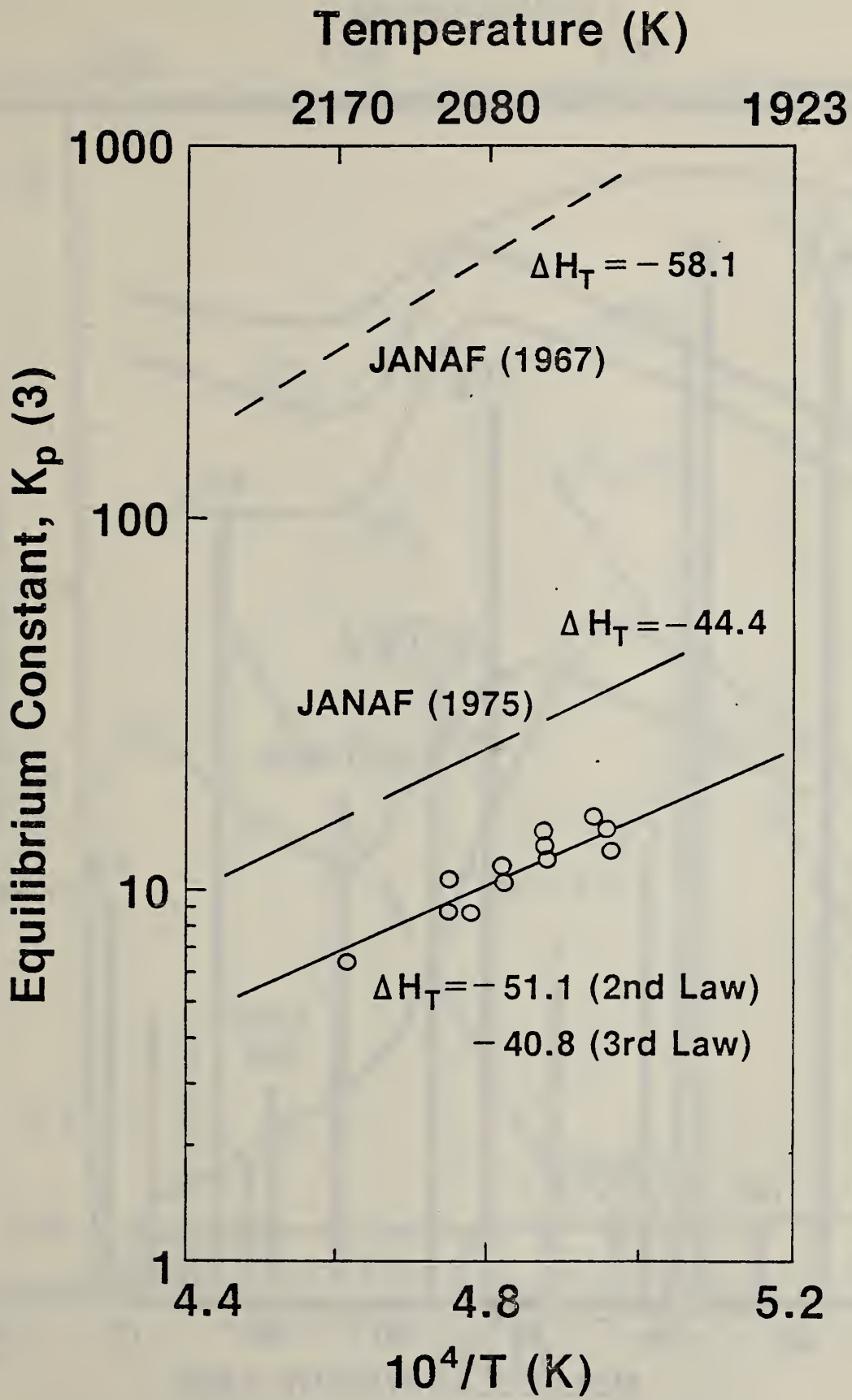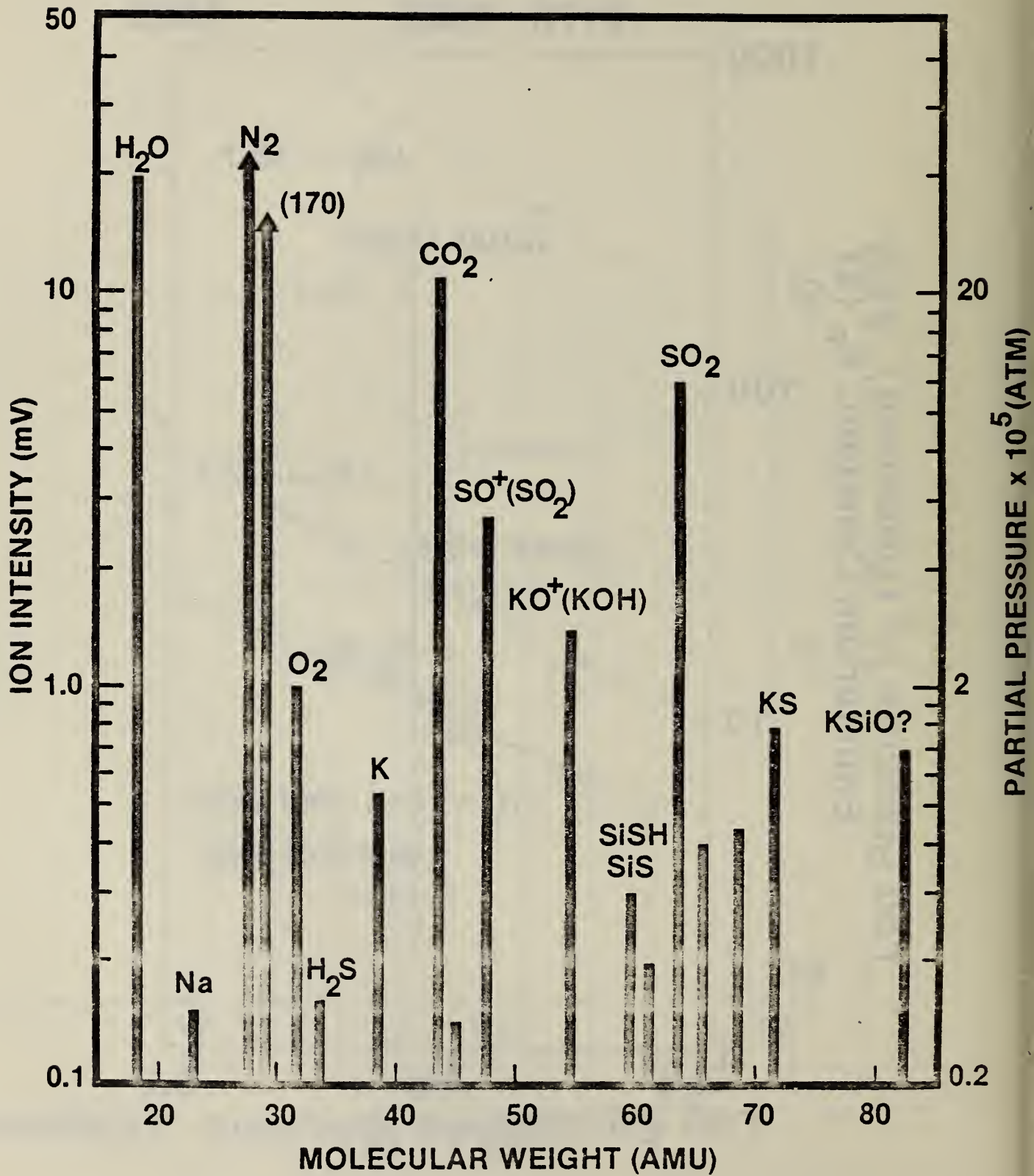
Figure 2
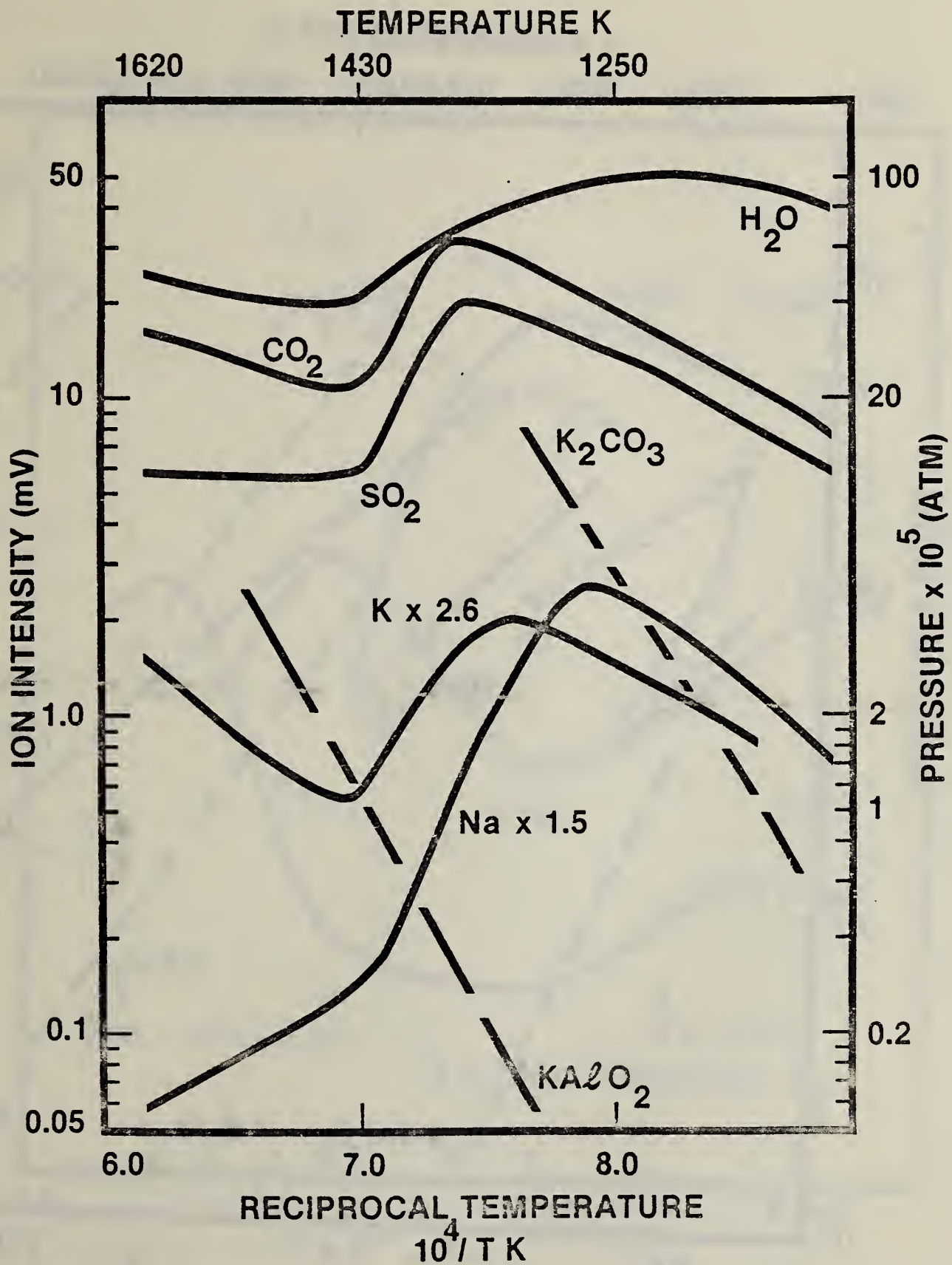
Figure 3

Figure 4

Figure 5
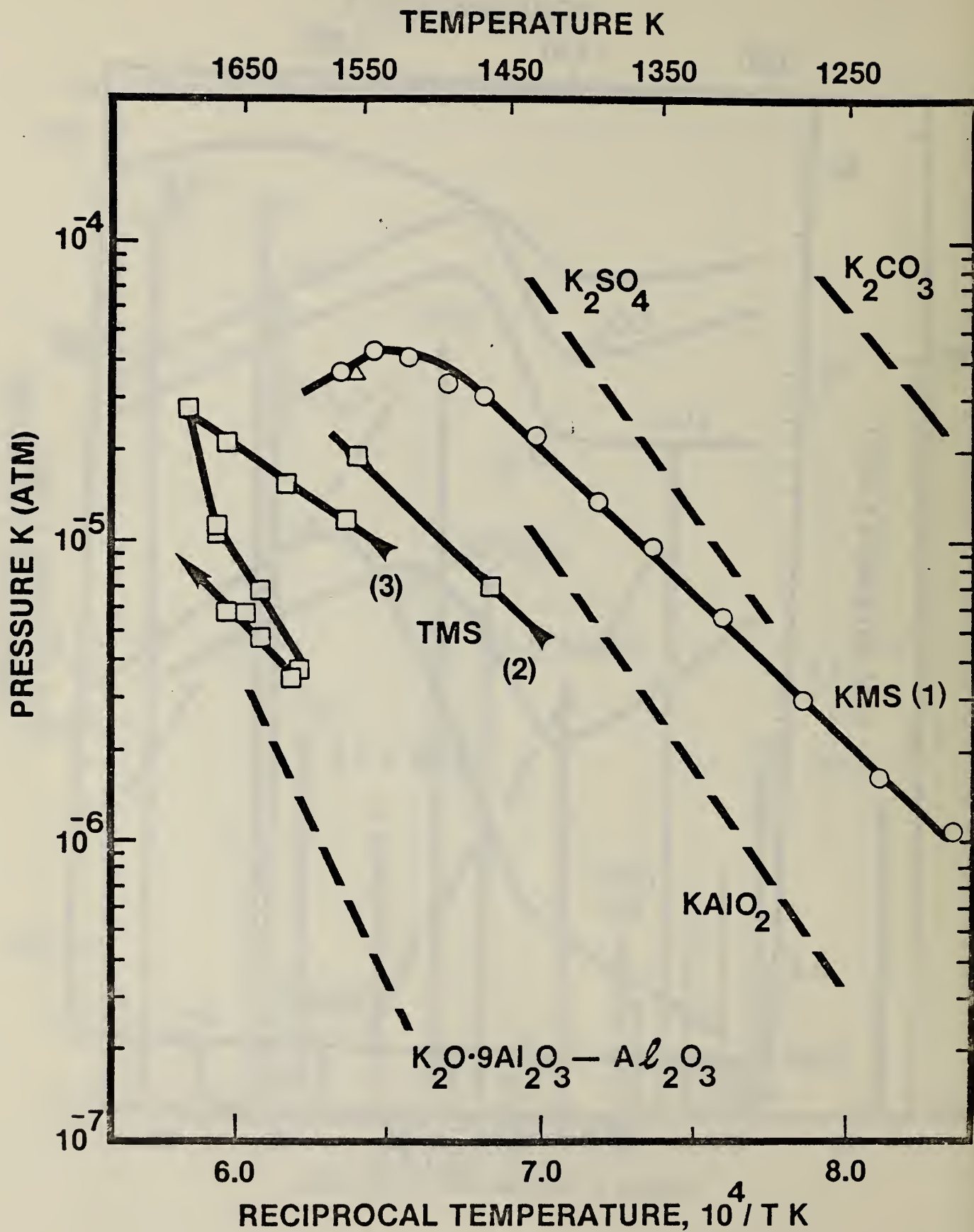
Figure 6
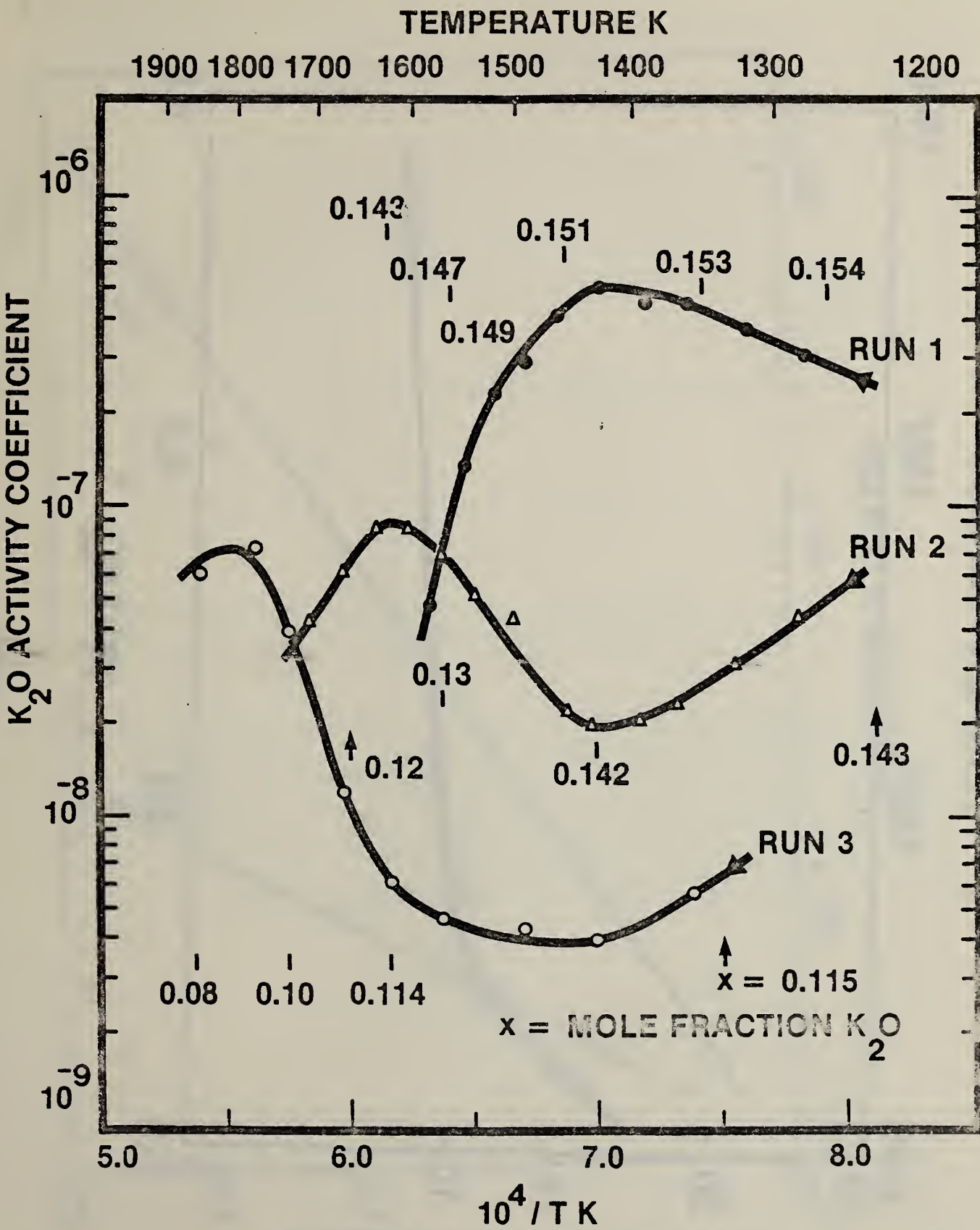
Figure 7

Figure 8

Figure 9

The figure shows a plot with axes labeled:
- Vertical axis (left): PRESSURE $K \times 10^5$ ATM, ranging from 2×10^{-4} at bottom to 3.0 at top, with marks at 1.0, 1.5, 2.0, 2.5, 3.0
- Horizontal axis (bottom): PRESSURE H_2O (ATM), with marks at 10^{-4}, 10^{-3}, 10^{-2}, 10^{-1}

A dashed line is labeled 0.5.

4. TITLE AND SUBTITLE

VAPORIZATION AND CHEMICAL TRANSPORT UNDER COAL GASIFICATION CONDITIONS

5. AUTHOR(S)

J. W. Hastie, D. W. Bonnell, E. R. Plante, W. S. Horton

11. ABSTRACT *(A 200-word or less factual summary of most significant information. If document includes a significant bibliography or literature survey, mention it here)*

The present studies have resulted in the development of a new experimental technique, transpiration mass spectrometry, for the quantitative analysis of high vapor temperature gases and vapors. This technique has been applied to vapor transport and thermodynamic activity determinations for real and synthetic coal slag samples in reactive coal gas components at atmospheric pressure. The results indicate a highly non-ideal and non-monotonic (with temperature and composition variables) behavior for alkali metal vapor transport. Thus a priori predictions of alkali metal transport in coal gasifiers without actual activity data are virtually impossible at the present time. Surface segregation and diffusion limitations of alkali species in slags are also possible complicating effects.

12. KEY WORDS *(Six to twelve entries; alphabetical order; capitalize only proper names; and separate key words by semicolons)*

Coal gasification; high temperature; mass spectrometry; slag; transpiration; vapor transport